Synthesis and Characterization of Metal-Chalcogenide MQ_2-Nanoparticles

(M = Mo, W, Zr; Q = S, O)

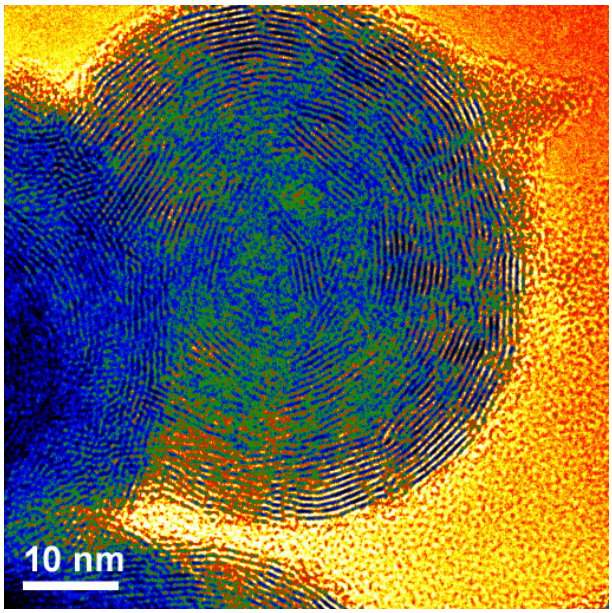

Dissertation

zur Erlangung des Grades

"Doktor der Naturwissenschaften"

am Fachbereich Chemie, Pharmazie und Geowissenschaften

der Johannes Gutenberg-Universität Mainz

Nicole Christin Zink

geb. in Frankfurt a. M.

Mainz, 2006

Alles Wissen

und alle Vermehrung

unseres Wissens

endet nicht mit einem Schlusspunkt,

sondern mit einem Fragezeichen.

Hermann Hesse

Wem, wenn nicht Dir, sei sie gewidmet (SDG).

TABLE OF CONTENT

1 INTRODUCTION 1

1.1 MOTIVATION 1
1.2 STATE OF THE ART 1
1.2.1 Fullerenes and Carbon Nanotubes 1
1.2.2 Structure of LTMCs[16-20] 2
1.2.3 Properties of LTMCs 4
1.2.4 Synthesis methods for LTMCs 8
1.3 SCOPE AND AIM 17
1.4 REFERENCES 24

2 A SOLVOTHERMAL ROUTE TO HIGH SURFACE AREA NANOSTRUCTURED MOS_2 31

2.1 INTRODUCTION 31
2.2 EXPERIMENTAL DETAILS 32
2.2.1 Synthesis 32
2.2.2 Characterization 33
2.3 RESULTS AND DISCUSSION 34
2.4 CONCLUSION 39
2.5 REFERENCES 39

3 SELECTIVE SYNTHESIS OF HOLLOW AND FILLED FULLERENE-LIKE (IF) WS_2 NANOPARTICLES VIA METAL-ORGANIC CHEMICAL VAPOR DEPOSITION (MOCVD) 41

3.1 INTRODUCTION 41
3.2 EXPERIMENTAL 43
3.2.1 Synthesis 44
3.3 CHARACTERIZATION 45
3.3.1 Electron microscopy 45
3.3.2 X-ray powder diffraction 45
3.4 RESULTS AND DISCUSSION 46
3.4.1 Hollow IF-WS_2 particles by a two-step synthesis 46
3.4.2 Single-step process – influence of the reaction temperature in the induction-heated zone 50
3.4.3 Growth mechanism 59
3.5 SUMMARY AND CONCLUSION 62
3.6 REFERENCES 63

4 *IN SITU* HEATING TEM STUDY OF ONION-LIKE WS_2 AND MOS_2 NANOSTRUCTURES OBTAINED VIA MOCVD 67

4.1 INTRODUCTION 67

4.2 EXPERIMENTAL ... 68
4.2.1 MOCVD synthesis ... 68
4.2.2 *In situ* heating TEM study ... 69
4.2.3 Instrumental details ... 69
4.3 RESULTS AND DISCUSSION ... 70
4.3.1 Pristine sample at the example of WS_2 ... 70
4.3.2 *In situ* heating TEM study ... 71
4.4 CONCLUSION ... 80
4.5 REFERENCES ... 80

5 LOW TEMPERATURE SYNTHESIS OF MONODISPERSE ZRO_2 NANOPARTICLES WITH HIGH SPECIFIC SURFACE AREA ... 82

5.1 INTRODUCTION ... 82
5.2 EXPERIMENTAL DETAILS ... 83
5.2.1 Synthesis ... 83
5.2.2 Characterization ... 84
5.3 RESULTS AND DISCUSSION ... 85
5.3.1 Differential thermal analysis and thermogravimetry ... 85
5.3.2 X-ray diffraction ... 86
5.3.3 Scanning electron microscopy ... 87
5.3.4 Transmission electron microscopy ... 88
5.3.5 Small angle X-ray scattering ... 93
5.3.6 Brunauer-Emmett-Teller nitrogen sorption ... 94
5.3.7 Raman spectroscopy ... 94
5.3.8 Photoluminescence spectroscopy ... 95
5.4 CONCLUSION ... 96
5.5 REFERENCES ... 96

6 CONCLUSION ... 100

7 LIST OF FIGURES ... 103

8 LIST OF TABLES ... 105

9 ABBREVIATIONS (ABBR.) ... 107

10 APPENDIX ... I

10.1 LAYERED TRANSITION METAL CHALCOGENIDES (LTMC) OF THE FORM MQ_2 ... I
10.2 CHARACTERIZATION METHODS ... II
10.3 SUPPLEMENTARY MATERIAL ... III
10.3.1 Ad Chapter 3: Selective Synthesis of Hollow and Filled Fullerene-Like (IF) WS_2 Nanoparticles via Metal-Organic Chemical Vapor Deposition (MOCVD) ... III

10.3.2 Ad Chapter 4: *In situ* Heating TEM Study of Onion-Like WS_2 and MoS_2 Nanostructures Obtained via MOCVD IV

10.3.3 Ad Chapter 5: Low temperature synthesis of monodisperse ZrO_2 nanoparticles with high specific surface area V

10.4 LIST OF PUBLICATIONS VI

10.4.1 Articles VI

10.4.2 Conferences VI

10.4.3 Patent VII

10.4.4 References VII

11 ZUSAMMENFASSUNG IX

12 ABSTRACT XI

1 Introduction

1.1 Motivation

Nanotechnology is regarded as one of the most important resorts of future technologies. A significant increase in investments in this field has been made in the last decade, *e.g.* the budget of the U. S. National Nanotechnology Institute has nearly tripled since its foundation in 2001[1] and the volume of the market on nanotechnology-based products is expected to reach the 1 Trillion US $ benchmark by 2015, taking into account the United States alone.[2]

The synthesis of nano-sized materials is essentially based upon two complementary principles: the top-down and the bottom-up approach. The top-down approach on the one hand – trying to achieve further miniaturization based on established methods – is a very old idea, not even the oldest example being *e.g.* the miniature bibles Gutenberg provided. This approach is still widely used to date. As a result *e.g.* integration density in microelectronics, *i.e.* the number of transistors per unit area on integrated circuits, is nearly doubled every 18 month (known as Moore's law).[3]

On the other hand, the bottom-up approach, building up nanostructures from the scratch, that is from the atoms and molecules, became possible only in the last century with the development of characterization methods suitable to this scale. This approach is promising in particular in research areas in which the top-down approach has reached the physical limit.

The present work is dedicated towards the synthesis and characterization of nano-materials of layered transition metal dichalcogenide (LTMCs) in a bottom-up approach.

In the sequel, the discovery of MQ_2 (M=transition metal, Q=chalcogenide) nano-materials, their morphology and their intriguing properties will be highlighted, followed by the presentation of the established synthetic approaches to such materials.

1.2 State of the Art

1.2.1 Fullerenes and Carbon Nanotubes

In „10 days of September 1985", Kroto *et al.*[4] discovered the existence of small hollow-sphere carbon structures later named „fullerenes"[i] in the soot produced by laser ablation of graphite, an experiment that was originally dealing with the study of unusual

[i] In reminiscence to the architect Buckminster Fuller whose famous geodesic domes have a large resemblance with the structures of these nanoparticles.

modifications of carbon namely in short chains with odd numbers of carbon atoms. Six years later another allotrope of carbon in form of nanotubes was realized by Iijima.[5]

Calculations suggested that those kinds of nanostructures could - in principle - be obtained from any layered material. The small interaction between the layers leads to a significant decrease of the elastic modulus C of the corresponding parent compound single sheet thereby reducing its bending energy per atom E_{bend}/N as compared to 3D-structures:

$$E_{bend} / N = \frac{Ca^3}{24\rho} \frac{1}{R^2}, \qquad (1\text{-}1)$$

where ρ is the number of atoms per unit area, and a is the thickness of the sheet bent into a cylinder of radius R.[6]

Up to now, a variety of layered materials were investigated and the synthesis of non-carbon (so-called inorganic) fullerene-like (IF) and nanotube (NT) modifications were reported.

BN. Chopra *et al.*[7] managed the synthesis of nanotubes of BN, which is isoelectronic to graphite, by arc discharge. An extensive list of synthesis methods and properties of BN and BN-related nanotubes and fullerene-like materials is summarized in Pokropivny.[8-10]

Oxides/Hydroxides. Only few exemplary references shall be given for the synthesis of oxide and hydroxide nanotubes. Nesper and co-workers used the intercalation of amines followed by a hydrothermal treatment to obtain V_2O_5 nanoscrolls.[11, 12] A similar approach by Shukoor *et al.*[13] yielded MoO_x nanoscrolls among other morphologies. Kasuga *et al.*[14] employed a sol-gel route for the synthesis of TiO_2 nanotubes of about 8 nm and ~100 nm in length. Rare earth hydroxide nanotubes, *e.g.* $Y(OH)_3$, were synthesized via a hydrothermal route by Wang and co-workers.[15]

1.2.2 Structure of LTMCs[16-20]

In the following section another class of layered compounds that are prone to form fullerene-like and nanotube morphologies, *i.e.* the layered transition metal chalcogenides (LTMC), will be discussed in more detail, as the present work is focused on these compounds.

The structure of many of the early transition metal dichalcogenides resembles that of graphite in the sense that those are layered structures (see the appendix for an overview). The two most frequent structure types observed for these compounds are the CdI_2- (*e.g.* TiS_2) and

the MoS_2-structure (Figure 1-1). Both exhibit a six-fold coordination of the metal by the chalcogenide, octahedral in case of CdI_2 and trigonal-prismatic in the MoS_2-structure.

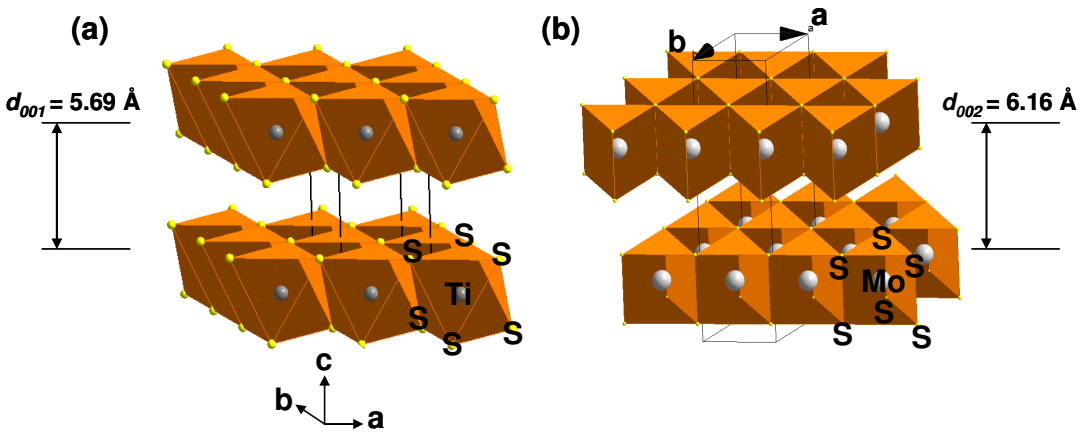

Figure 1-1. Crystal structures of TiS_2 (CdI_2) (a) and MoS_2 (b).

By joining the polyhedrons at their edges, X-M-X sandwich layers are formed (M = Cd, Mo; X = I, S). Note, for MoS_2 the X-layers are in registry (aBa), for CdI_2 they are not (aBc). The layers can be stacked perpendicular to the layer plane in different sequences leading to several polytypes.

For MoS_2, the most common and thermodynamically stable modification is the 2H-type in which an ABA stacking is realized (see Figure 1-1(b)). ABCA stacking leads to the 3R-modification with the same interlayer distance of $d_{002/003}$ = 0.616 nm. Less frequent is the 1T-polymorph.

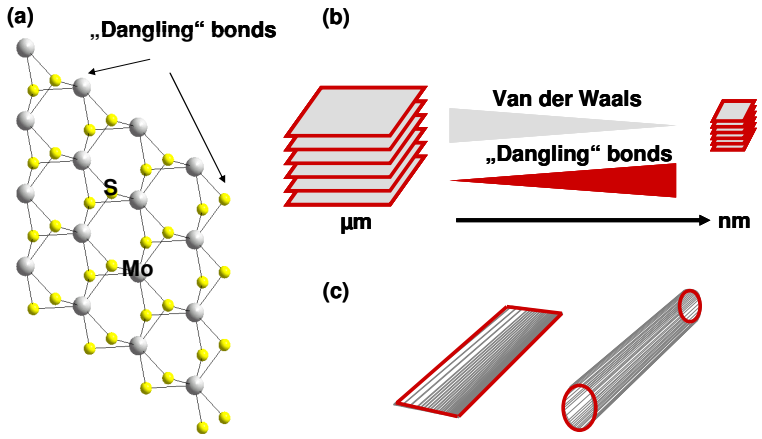

Figure 1-2. Schematic illustration of „dangling“ bonds in a MoS_2 sheet (a), the size effect of volume to surface ratio (b), and the minimization of dangling bonds and surface by tube-formation (c).

A single MoS_2 sheet exhibits unsaturated Mo and S atoms at the border-lines. These atoms have so-called "dangling" bonds which are energetically unfavorable (Figure 1-2(a)). In bulk material, the energy gain by interlayer interactions compensates the energy loss by dangling bonds. Upon size reduction to the nanometer range, the ratio of surface to volume increases (Figure 1-2(b)). Subsequently, the effect of dangling bonds exceeds that of interlayer interactions. Thereby, folding of the layers to minimize the number of dangling bonds (Figure 1-2(c)) gets more favorable even though it requires the bending energy E_{bend} (see Equation 1-1).

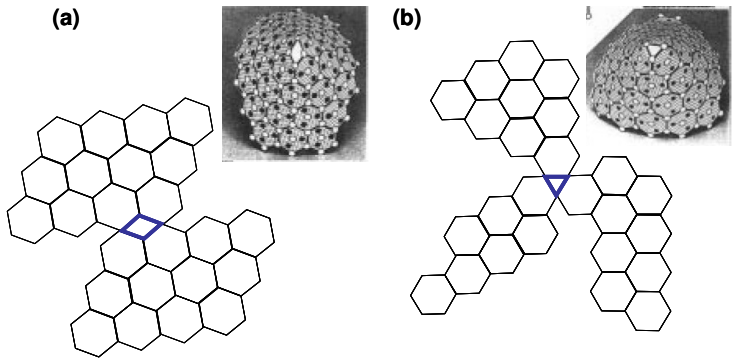

Figure 1-3. Rhombohedral (a) and trigonal (b) point defect inducing curvature in MoS_2 layers.[21]

In order to form fullerene-like nanoparticles or nanotubes, curvature has to be generated. In the case of carbon, hexagonal rings in the graphene sheet are replaced by pentagonal or heptagonal rings, which induce curvature (Euler Theorem). As the formation of pentagons and heptagons is unfavorable for heteroatomic compounds, spherical structures are realized by formation of defects. For MQ_2 layers, those defects are rhombohedral and trigonal point defects (Figure 1-3), leading to topological defects. Combining topological defects generates positive (square-like topological defect) or negative (octagonal-like defect) curvatures.

1.2.3 Properties of LTMCs

Inorganic nanotubes, fullerene-like particles and nanostructures exhibit a variety of interesting properties that will be briefly discussed in the subsequent paragraphs. A recent review is given by Tenne and Rao.[22]

1.2.3.1 Physical properties

1.2.3.1.1 Band structure calculations, electrical and magnetic properties

Soon after the discovery of synthesis methods for inorganic nanotubes and fullerene-like structures, theoretical studies were conducted in order to determine the stability as well as the electronic and magnetic properties of such structures. To date, a high number of compounds has been investigated mainly by Seifert, Enyashin and co-workers. Some of the results are summarized in Table 1-1.

Table 1-1. Theoretical studies on MS_2 (M=transition metal) nanotubes and fullerene-like particles.

Compound	Morphology	Method	Properties	Reference
WS_2	NT[a]	TB-DFT[b]	Semiconducting	23
MoS_2	NT	TB-DFT	Semiconducting	24
	IF[c]	MM[d]+SC[e]-DVM[f]/LSDFT[g]	Metallic, μ[h]=0.9-1.6 μ_B	25, 26
NbS_2	NT	TB-DFT	Metallic, superconducting	27
	IF	MM[d]+SC[e]-DVM[f]/LSDFT[g]	Metallic, μ=0.3-0.5 μ_B	25, 26
$NbSe_2$	NT	TB-DFT[b]	Metallic, superconducting	28, 29
	IF	FPLMTO[i] (LDA)[j]	Metallic	
TaS_2	NT	FPLMTO[i] (LDA)[j]	Metallic, superconducting	30
TiS_2	IF	MM[d]+SC[e]-DVM[f]/LSDFT[g]	Metallic, μ=0 μ_B	25
ZrS_2	NT	TB-DFT[b]	Semiconducting	31
	IF	SC[d] *ab initio*, MM[d]+SC[e]-DVM[f]/LSDFT[g]	Metallic, μ=0 μ_B	25, 26, 32, 33

[a]Nanotube, [b]tight-binding density functional theory, [c]fullerene-like nanoparticles, [d]molecular mechanics, [e]self-consistent, [f]discrete variation method, [g]local spin density functional theory, [h]magnetic momentum, [i]full potential linearized *muffin-tin* orbital method, [j]local density approximation.

For MoS_2 and WS_2, armchair and zig-zag nanotubes are stable for diameters above 20 Å. Squarelike and octagonal defects were used to introduce curvature.[24] Both modifications are semiconducting in contrast to NbS_2 and $NbSe_2$ metallic nanotubes. Scanning tunneling microscopy (STM) studies report the band gap of WS_2-NT to decrease upon decreasing diameter.[34] Due to the small direct bandgap found in zig-zag MoS_2-NTs, those are discussed to be suitable for application in optoelectronics. $MoS_{2-x}I_z$ nanotubes synthesized via an iodine mediated chemical vapor transport method exhibit reproducible stable field emitting properties with currents higher than 10 µA.[35] $NbSe_2$ nanotubes and -wires obtained from thermal decomposition of $NbSe_3$ are metallic and show superconductivity below T_C = 8.3 K.[36]

According to *ab initio* calculations by Enyashin *et al.*,[25] fullerene-like MoS_2 particles exhibit three stable structures: octahedral, cuboctahedral and dodecahedral. Formation of

octahedral particles was experimentally confirmed by Parilla *et al.*[37] MoS_2 and WS_2 fullerene-like structures are semiconductors as shown by optical absorption spectroscopy measurements.[38] The band gap is smaller than in the bulk material. IFs consisting of only few layers exhibit an increased band gap which was attributed to quantum confinement in *z*-direction. Pellets of IF-WS_2 exhibit comparable transporting properties as the bulk compound with a slightly higher absolute electrical resistance value due to interparticle boundaries.[39]

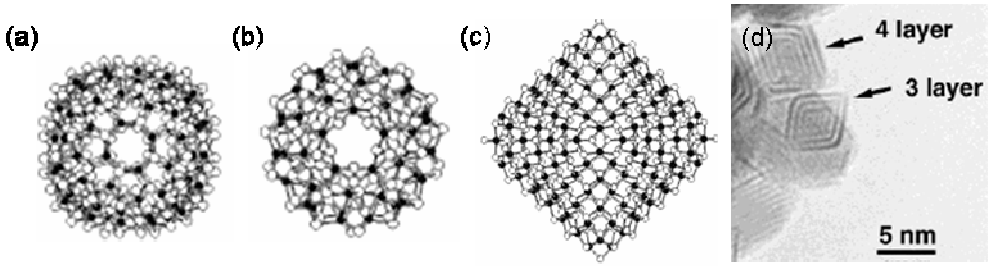

Figure 1-4. Atomic structure of fullerene-like MoS_2 with (a) cuboctahedral and (b) dodecahedral, and (c) octahedral morphology.[40] Transmission electron microscopy image of a nano-octahedron obtained by Parilla is given in (d).[37]

1.2.3.1.2 Tribological performance

Bulk MoS_2 is long known as a solid lubricant. Weak van der Waals interactions between the layers allow an easy shearing. Being a solid lubricant, MoS_2 is even applicable in vacuum (aerospace) or at high temperatures, *i.e.* upon conditions, when oils and greases come to their limits. A variety of investigations have shown that inorganic fullerene-like particles of MoS_2 and WS_2 outperform the bulk material in wear, lubricating power and lubricating lifetime on various conditions (*e.g.* as additives in oil,[41-43] as thin films,[44] or in a self-lubricating porous matrix[45]). A number of products are already commercialized, the most recent being IF-WS_2 in lubricating orthodontic wires.[46]

The lubricating mechanism is still under discussion. Early studies attributed the improved behavior to a rolling mechanism.[47, 48] More recent analyses demonstrate that the rolling mechanism is only taking place in low load situations.[49] On higher load, delamination of the IFs and subsequent material transfer lead to an ultrathin and very smooth tribofilm exclusively in the friction zone.[50-54]

The lack of dangling bonds in closed-shell structures is assumed to improve the stability towards oxidation and to lower the adhesion to the surface, improving the lubricating behavior of these structures. On the other hand, recent thermal stability studies[55] demonstrated that bulk MoS_2, WS_2 and NbS_2 exhibit a slightly higher oxidation onset temperature in O_2 atmosphere than the corresponding IF-materials, which is in contradiction to the assumed inertness of closed-shell structures. Nevertheless, oxidation temperatures of ~350°C in O_2

atmosphere and decomposition temperatures around 1200°C in N_2 atmosphere are still highly sufficient for their application as commercial lubricants.

Furthermore, the hollow cages of IF-MoS_2 nanoparticles can be elastically deformed, which makes them stable even on high loads.[48] A comparison of the performance of MoS_2 and WS_2 nanoparticles as lubricants is difficult as the morphologies tend to be quite different mostly due to different synthesis approaches.

1.2.3.1.3 Mechanical behavior

The closed-shell structure of inorganic fullerene-like particles of MoS_2 and WS_2 and the nearly defect-free structure of WS_2 nanotubes (NT) make them very good shock absorbers up to pressures of 25 GPa and 21 GPa, respectively.[56-58] Oxide cores (coming from incomplete sulfurization), faceting or mixtures of tubes and nanoparticles reduce the performance significantly. The Young modulus of WS_2-NT was determined to be 171 GPa and is comparable to the bulk material (150 GPa). The tensile strength is ~13 GPa with a critical strain of 12-19%.[59] Their excellent mechanical behavior and their high aspect ratio makes WS_2-NT an ideal material for atomic force microscopy tips especially when deep and narrow pits have to be studied.[60]

1.2.3.2 Chemical properties

1.2.3.2.1 Intercalation and H_2 storage

Inorganic nanotubes and fullerene-like structures are discussed as battery material in nanocircuits. Therefore, their intercalation behavior is of great interest. Zak *et al.*[61] studied the intercalation of alkali metals into MoS_2 and WS_2-IFs and found a reversible intercalation behavior. Intercalated material exhibited a significantly higher electrical conductivity and was paramagnetic opposed to the diamagnetism of the pristine sample. Thin films of intercalated IFs are reported to exhibit a photoeffect.[62]

For intercalation purposes, defect-rich structures should be preferred as the access of metal ions into the interlayer space would be made easier. This has been shown for chemically etched single-walled carbon nanotubes[63, 64] and ball-milled MoS_2-NT.[65] On the other hand, closed shells prevent highly reactive materials such as Li from a violent reaction with surrounding moisture.

Therese *et al.*[66] reversibly intercalated 0.77 equivalents of copper-ions in VS_2-NTs. This corresponds to a specific capacity of 314 mA h/g and is only slightly lower than the theoretical capacity of graphite (372 mA h/g).[67]

Bundles of sub-nanometer $MoS_{2-x}I_z$ tubes obtained from C_{60} catalyzed chemical vapor transport reactions are reported to reversibly intercalate Li, the total number of Li atoms per formula unit being 2.3 times higher than for bulk MoS_2. Electron spin resonance measurements proved the contribution of electrons from Li to the host material.[68-70]

TiS_2 nanotubes could be reversibly Li-intercalated by Chen and co-workers.[71] Furthermore, they are now established as cathode materials for Mg ion rechargeable batteries with high capacities.[72] Additionally, the TiS_2-NTs were found to load up to 2.5 wt.% hydrogen under 4 MPa. MoS_2-NTs were also tested for their H_2 storage ability. Reversible electrochemical intercalation was possible with a charge-discharge capacity of 260 mA h/g. The capacity remained nearly unchanged (2% loss) even after 30 charge/discharge cycles.[73]

1.2.3.2.2 Catalytic activity

Besides employment as solid lubricant, MoS_2 is of great importance as catalyst in the hydrodesulfurization (HDS) process for the desulfurization/hydrogenation of fuels. Theoretical[74] and experimental[75-77] studies have shown that the catalytic site for the C-S bond cleavage are the unsaturated Mo atoms situated at the edges of the MoS_2 slabs. More demanding limiting values for environment protection, increase in fuel consumption combined with the need to exploit oil sources of lesser quality, *e.g.* higher sulfur contents, makes the development of high activity catalysts an urgent task. Nanomaterials, with their high surface to volume ratio, seem to be suitable candidates for further improvement of catalytic activity. Nanostructured MoS_2 showed indeed a higher HDS performance than conventional catalysts.[78-80] Recent research focuses on tuning of the M-S strength by synthesis of mixed compounds to a further enhancement of the activity of such catalysts.[81]

Additionally, MoS_2-NTs synthesized from $(NH_4)_2MoS_4$ in H_2 atmosphere exhibit catalytic activity for the methanation of CO and hydrogen at temperatures of 100 K lower than in the conventional process.[82]

1.2.4 Synthesis methods for LTMCs[ii]

In the sequel different synthesis approaches for nanostructures of layered early transition metal chalcogenides of the formula MQ_2, where M is a group (IV, V, VI) transition metal and Q can be S, Se or Te will be presented. Note, that the classification to a specific approach is ambiguous in some cases but the reference will be cited only once.

[ii] Synthesis methods of MoS_2, WS_2 and other layered transition metal chalcogenides (LTMC) are summarized in Table 1-4 at the end of this chapter.

1.2.4.1 Far from equilibrium and high energy methods

Nanotubes and inorganic fullerene-like nanoparticles are metastable phases. Therefore, far from equilibrium methods are necessary to prevent the formation of the thermodynamically stable bulk phase. On the other hand, high energies are needed to "knit" together the folded layers.

1.2.4.1.1 Laser ablation

One of the methods already known from the synthesis of C_{60} is laser ablation of a suitable target material. Soon after the synthesis of $NiCl_2$ nanotubes and fullerene-like particles by laser ablation,[83-85] Parilla *et al.* yielded nano-octahedra of MoS_2 with the same method, which was later extended to $MoSe_2$.[37, 86] Metal-filled and hollow inorganic fullerene-like particles of MoS_2 and WS_2 were obtained some years later by Sen *et al.*[87] Recently, Schuffenhauer *et al.* managed the synthesis of filled TaS_2 fullerene-like particles by laser ablation of TaS_2 under Ar and CS_2, respectively.[88] Hf_2S-IFs could be synthesized via laser ablation in a liquid medium.[89] Laser ablation in water resulted in hexagonal WS_2 nanoparticles.[90] Facetted IFs consisting of SnS_2 and SnS were synthesized by Hong *et al.*[91]

1.2.4.1.2 Arc discharge

Another method that has already been employed for the (carbon) fullerene synthesis is the arc discharge method. Chhowalla *et al.* were the first to successfully adopt this method for the synthesis of MoS_2-IFs in form of a thin film that exhibited an excellent lubricating behavior.[44]

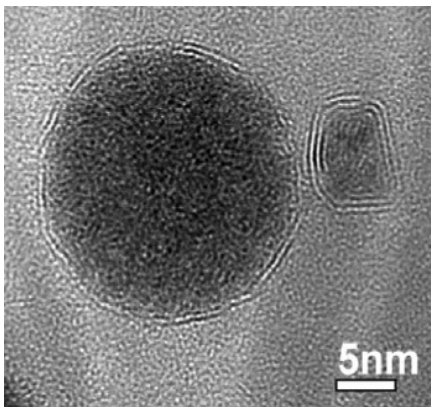

Figure 1-5. TEM of multi-walled IFs with a solid core.[92]

Other fullerene-like particles, sometimes filled with different materials, *e.g.* CoS inside WS_2-IFs, were synthesized soon after.[49, 92-96] Filled IFs are especially interesting because they

might be advantageous compared to hollow particles as far as stability upon pressure load is concerned.

1.2.4.1.3 Microwave-induced plasma

The microwave-induced plasma method gives access to a large variety of compounds. By reacting $M(CO)_6$ with H_2S or $SeCl_4$, Vollath and Szabo obtained MQ_2 (M=Mo, W; Q= S, Se) nanoclusters, partly also in form of fullerene-like particles.[97, 98] Furthermore, nanoclusters of SnS_2 and ZrS_2 were prepared with the same setup. Starting from WO_3 nanoparticles, ZrS_3 or HfS_3, Brooks *et al.* obtained WS_2 and HfS_2-IFs, and ZrS_2 nanotubes and –rods, respectively, in microwave-induced plasmas of H_2S and N_2/H_2.[99]

1.2.4.1.4 Electron beam irradiation

Electron beam irradiation of samples can cause defects and subsequent folding of layered materials. IFs of MoS_2 were synthesized accordingly.[100] Jose-Yacaman found that in the inner part of these onion-like structures (small radii) faceting occurs whereas the outer layers (larger radii) are bent. $NbSe_2$, $MoSe_2$ and silver containing NbS_2 nanotubes could be obtained by electron beam irradiation of adequate precursor materials.[101-103] In the case of $NbSe_2$ the nanotubes were mixed with IFs and nanorods.

1.2.4.1.5 Spray pyrolysis

A different approach to reduce the size of the product is to limit the reaction volume within small droplets as it is done in the spray pyrolysis. IFs and nanoboxes of MoS_2 and WS_2 were obtained when finely dispersed ethanolic solutions of $(NH_4)_2MS_4$ (M = Mo, W) were pyrolyzed at 900°C.[104]

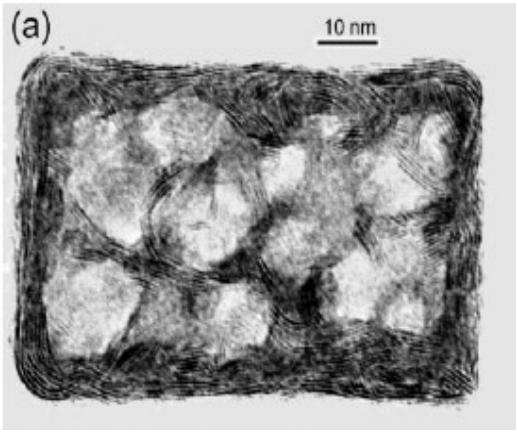

Figure 1-6. WS_2 nanobox obtained in a spray pyrolysis process.[104]

He and co-workers prepared MoS_3 nanoparticles with diameters from several Ångstrøm to 5 nm via spray pyrolysis at 220°C.[105] A subsequent annealing in an H_2/Ar atmosphere at 850°C yielded MoS_2 nanoparticles of about the same size.

1.2.4.1.6 Other high energy methods

High-intensity ultrasonic irradiation of $M(CO)_6$ (M=Mo, W) and S was used to prepare nanostructured MoS_2 and WS_2 nanorods, respectively.[78, 106] Heating bulk MoS_2 under a Mo foil in an H_2S atmosphere at temperatures of 1200-1300°C resulted in MoS_2-NTs.[107] The very first proof that layered transition metal chalcogenides can form nanotubes was given, when Tenne *et al.* synthesized WS_2 nanotubes by heating a WS_2 film on a glass substrate at 1000°C in an H_2S atmosphere.[108]

1.2.4.2 Facilitated diffusion

Conventional solid state syntheses of transition metal chalcogenides yield highly crystalline bulk-material due to the high temperature and long duration of the experiments. High temperatures and long times are obligatory to obtain a homogeneous mixture of the reactants. One approach to avoid these conditions for the synthesis of nanomaterials is the decrease of diffusion ways as has been realized in the following synthesis methods.

1.2.4.2.1 Ball milling

Ball milling decreases the size of the precursor material crystallites. When milling of two or more components is concerned, this process leads to an intimate mixture through a fracture-welding-rewelding mechanism.[109] Thus, it decreases the diffusion pathways and thereby allows the synthesis of far from equilibrium materials. Chen *et al.* used this approach for the formation of MS_2 (M=Mo, W) nanotubes from ball milled $(NH_4)_2MS_4$ and the synthesis of $TiSe_2$ nanowires and -nanotubes by annealing a ball milled stoichiometric mixture of Ti and Se at 650°C/8h under Ar.[110-113]

1.2.4.2.2 Chemical vapor deposition (CVD)

Chemical vapor deposition is a classical method for the synthesis of thin films and has only recently been discovered for the synthesis of IFs and NTs. Ge *et al.* obtained WS_2 nanotubes with diameters of 10-30 nm by CVD from WCl_6 and S on a Si substrate.[114] Starting from S and $MoCl_5$ or WCl_6, Li *et al.* obtained MoS_2 and WS_2 inorganic fullerene-like structures, respectively.[115]

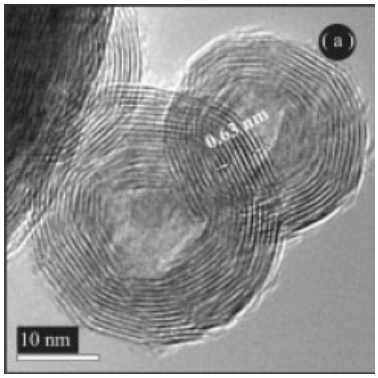

Figure 1-7. Hollow onion-like particle of MoS_2 synthesized in a two-step CVD-based process.[116]

MoS_2 and $MoSe_2$ hollow inorganic fullerene-like structures were synthesized in a two-step CVD-based process, starting from $Mo(CO)_6$ and S or Se.[116] Gao *et al.* produced MoS_2 nanotubes by chemical vapor deposition of MoO_3 and S in a conventional tube furnace.[117] A recent review on atmospheric pressure CVD of IFs and NTs is given by Zhang.[118]

1.2.4.2.3 Vapor transport reactions

A classical method for the synthesis of bulk transition metal chalcogenides is chemical vapor transport. A stoichiometric mixture of the elements and a small amount of a transport agent are sealed in an evacuated silica quartz tube and heated in a temperature gradient for usually several days or even weeks. Remskar *et al.* adopted this synthesis for the formation of MoS_2 and WS_2 micro- and nanotubes using I_2 as transport agent.[119-122] Interestingly, the microtubes consist of the 3R- instead of the 2H-polytype. The addition of C_{60} led to bundles of subnanometer $MoS_{2-x}I_y$ tubes that exhibit interesting properties such as reversible Li intercalation and the use as field emitter.[123] Doping of the WS_2 and MoS_2 nanotubes with Ag and Au was also achieved via the chemical vapor transport technique.[124]

1.2.4.2.4 Decomposition of a suitable precursor

Another method to ensure short distances between the reactants and therefore short diffusion pathways is to use a precursor molecule containing both, M and Q. Ideally, the molecule solely consists of M and Q, or of entities that will evaporate upon synthesis conditions. As early as 1996, Homyonfer *et al.* obtained inorganic fullerene-like particles of MoS_2 induced by electrical pulses from a scanning tunneling microscope (STM) to amorphous MoS_3 on a Au substrate. Leist *et al.* synthesized high surface area, nanostructured MoS_2 from $(NH_4)_2MoS_4$, $(NH_4)_2Mo_2S_{12}$ and $(NH_4)_2Mo_3S_{13}$.[125] A solution based reaction of $(NH_4)_2MoS_2$ with hydrazine was employed by Afanasiev *et al.* for the synthesis of nanostructured MoS_2.[126] Ammonium thiometallates $(NH_4)_2MS_4$ (M=Mo, W) and MQ_3 (M= Zr, Hf, Ti, Mo, Nb, W; Q=S, Se) have been successfully employed as precursor materials for the synthesis of MQ_2

nanotubes and -particles, respectively, by Nath, Rao and co-workers[17, 36, 89, 127-131] and Chen *et al.*[65, 110, 111] Co-precipitation of $(NH_4)_2MoS_4$ and $(NH_4)_2WS_4$ yielded $Mo_xW_{1-x}S_2$ nanotubes upon decomposition by thermal treatment in H_2/Ar atmosphere.[132]

1.2.4.3 Templated structures

The synthesis of anisotropic metastable materials such as nanotubes is particularly challenging. One approach is the use of templates that force the product into anisotropic morphology. Additionally, templates are favorable in applications and investigations that request a homogeneous and monodisperse product in order to avoid tedious and expensive post-reaction separation procedures. In the sequel, methods, that use supplementary materials in order to obtain the desired morphology, will be presented.

1.2.4.3.1 Template inside – CNTs and SiO_2 nanospheres

As synthetic approaches to carbon nanotubes (CNT) are well-developed, these were used as templates for the synthesis of MQ_2-NTs.

Walton and co-workers were the first to coat carbon nanotubes and bundles of them with transition metal chalcogenide layer(s), namely NbS_2[133, 134] and WS_2 (Figure 1-8).[135-140] Brorson *et al.* soon followed with the synthesis of ReS_2 coated CNTs.[141] The basic principle of this template synthesis is to suspend the CNTs in a suitable precursor solution. Drying leads to a uniform coating with the precursor material that is subsequently sulfurized with H_2S at elevated temperatures. Variation of the reaction parameters allows single or multi-layer coating. Ma *et al.* combined the template method with hydrothermal synthesis and obtained MoS_2 coated CNTs.[142]

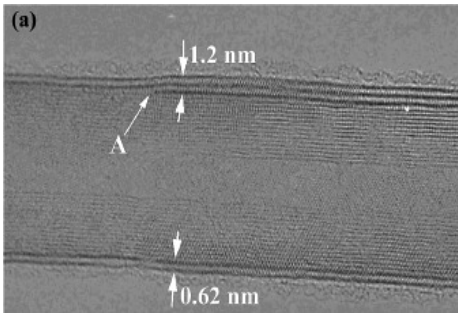

Figure 1-8. WS_2 coated multiwall CNT.[140]

Recently, Dhas and Suslick[143] used SiO_2 spherical nanoparticles as template for the synthesis of IF-MoS_2. Here, the sulfide was synthesized from $Mo(CO)_6$ and S by a sonochemical route. Additionally, the template was removed with HF resulting in hollow nanospheres of MoS_2.

1.2.4.3.2 Template outside – membranes and inverse micelle technique

One main disadvantage of an inner template is the lack of controllability of the diameter of the resulting spheres or tubes. Therefore, outer templates were used to achieve (nearly)-monodisperse sizes of the nano-materials.

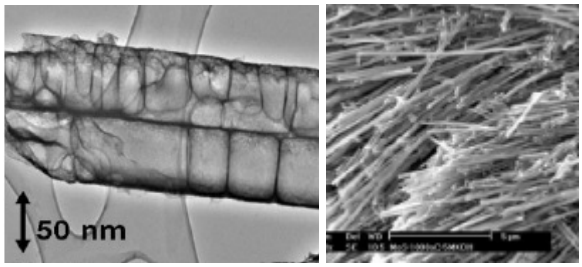

Figure 1-9. MoS_2 nanotubes synthesized using an alumina membrane as template.[144]

An Al_2O_3 membrane with uniform holes prepared by an anodization process was used to synthesize MoS_2-NTs. Zelenski and Dorhout[145] used the decomposition of $(NH_4)_2MoS_4$ and $(NH_4)_2Mo_3S_{13}$, Loh *et al.*[146] started from tetrakis(diethylaminodithiocarbomato)molybdate(IV) and Che *et al.*[144] applied an oxide to sulfide conversion with H_2S. Only in the first two methods the product is forming indeed within the pores of the Al_2O_3 membrane leading to nanotubes with a nearly monodisperse diameter-distribution. On the one hand, this method allows a high yield production of nanotubes. On the other hand, the resulting nanotubes are far from perfect as they are divided in nanoboxes of about 10-100 nm in length by MoS_2 layers perpendicular to the tube axis. Recently, Reza-San Germán *et al.* pyrolyzed propylene in such MoS_2 nanotubes and ended up with coaxial MoS_2-C nanotubes.[147]

In the case of the oxide to sulfide conversion by Che, the porous alumina serves as a support of the oxidic precursor that is actually growing to needles outside the pores. The pores ensure a narrow size distribution of the diameters of these needles.

A second method of outside templating is the inverse micelle technique. Micelles are formed *e.g.* when a surfactant, that is a molecule with a hydrophilic “head” and a hydrophobic “tail” (or vice versa), is added to a mixture of a hydrophilic and a hydrophobic solvent. The ratio of surfactant, lipophilic and hydrophilic solvent determines the morphology (*e.g.* lamellar, spherical, cylindrical shape) of the micelles and can therefore be tuned by choosing the appropriate area in the 3-component phase diagram.

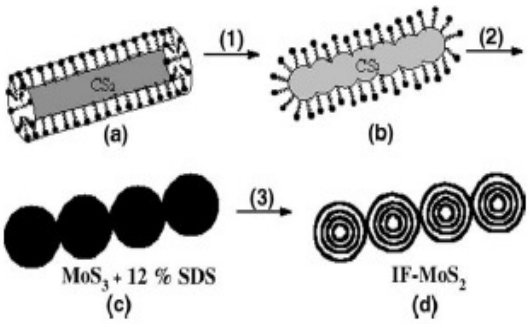

Figure 1-10. Scheme for the inverse micelle technique synthesis of IF-MoS_2.[148]

Very small and monodisperse nanoclusters of MoS_2 in form of discs could be obtained by Wilcoxon and Samara[149] from the mixture of inverse micelle solutions of $MoCl_4$ and H_2S. These cluster exhibit a blueshift in the optical absorption due to quantum size confinement. Choosing either H_2S or $(NH_4)_2S$ as sulfidizing agent, Chikan and Kelley[150] selectively synthesized nanoclusters of 3.5 or 8 nm in diameter, respectively.

Xiong *et al.*[148] obtained necklace-shaped fullerene-like MoS_2 particles starting from an inverse micelle solution of CS_2/sodium-laurylsulfonate (SDS)/1-octanol. Nested onion-like MoS_2 nanoparticles were synthesized via a hydrothermal reaction of this inverse micelle solution with an aqueous solution of Na_2MoO_4 with $N_2H_4 \cdot H_2O$ at low temperature (140°C) and subsequent annealing at 850°C in vacuum (schematic illustration of the growth mechanism see Figure 1-10).

CdS and CdSe nanotubes were obtained from a reaction of CdO and NaHQ (Q=S, Se) in aqueous solution upon addition of surfactant.[151]

High surface area highly dispersed layers of MoS_2 were produced by Afanasiev *et al.* when heating an ammonium thiomolybdate solution with cetyltrimethylammonium chloride (CTACl) upon reducing conditions.[126] The structure directing property of CTA^+ ions was also used by the approach of Li *et al.* to synthesize WS_2-NTs from co-condensation of CTA^+ anions and WS_4^{2-} cations into lamellar structures und subsequent reducing at 850°C. Amine intercalation und subsequent hydrothermal reaction yielded MoS_2 nanotubes.[152]

1.2.4.3.3 Precursor morphology dictates final morphology

In order to avoid contamination of the product and laborious cleaning of the product from the template, respectively, a different approach was chosen. In this method, a precursor material, that already exhibits the desired morphology, *e.g.* anisotropy and size, is chemically converted to the corresponding MQ_2 chalcogenide. As shown for the sulfurization of oxides, an outward-in growing mechanism of the sulfide layers leads to a complete encapsulation of

the precursor nanoparticles. This prevents the coalescence and therefore the increase in size of the precursor particles even at high synthesis temperatures.

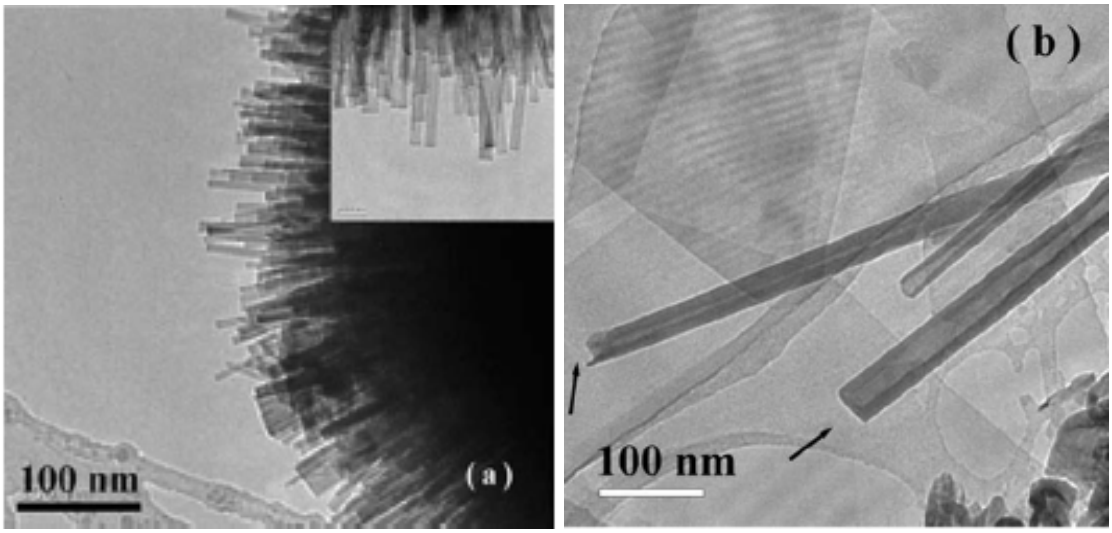

Figure 1-11. TEM images of WO_x nanorods (a) and the resulting WS_2-NT (b) obtained by Therese *et al.*[153]

The most widely used class of suitable precursor materials are the corresponding oxides. As early as 1993, Margulis[154] *et al.* oxidized a Mo film on a quartz substrate and sulfidized it subsequently with an H_2S/forming gas mixture obtaining fullerene-like MoS_2 nanoparticles. By numerous studies of the same group of Tenne this approach was extended to the synthesis of nanotubes and similar WS_2 products,[21] *e.g.* implementation of a specially designed fluidized bed reactor that allows the high-yield synthesis of WS_2 nanotubes. IF-VS_2 and IF-SnS_2 nanoparticles were obtained in a similar procedure.[21] Other groups used the same oxide-to-sulfide/selenides method, but with different starting materials or oxidizing/sulfidizing agents. Zhu *et al.* for example synthesized WO_x nanorods by heating a tungsten film in the presence of H_2O vapor and SiO_2 as oxygen source.[155] The same setup allowed the conversion into WS_2 nanotubes by annealing in H_2S. Hydrothermally prepared WO_x nanorods and amine-intercalated VO_x nanotubes, could be used to obtain high-yield, high-quality WS_2- (Figure 1-11) and VS_2 nanotubes, respectively.[66, 153] Ball-milling of ReO_2 to nanoparticles and reaction with H_2S yielded ReS_2 fullerene-like particles.[156] IF-selenides, namely WSe_2 are also accessible by this method either with H_2Se or Se as selenizing agent.[157, 158]

By mixing adequate precursors, the oxide-to-chalcogenide route allows the easy synthesis of mixed metal chalcogenide nanostructures, $M_xM'_{1-x}Q_2$, *e.g.* Nb-doped WS_2-NTs,[159, 160] Ti-doped MoS_2-NTs[161] and $W_xMo_yC_zS_2$-NTs.[162] This route reaches its limit, when very oxiphilic elements, such as Ti, Zr, Hf, are concerned. Decomposition of oxygen-free precursor materials turned out to be a solution to this issue.

1.2.4.4 Others

1.2.4.4.1 Sulfidization with H_2S

The reaction of an adequate reactant with H_2S at high temperatures is a wildly applied technique for the formation of MS_2 nanoparticles. Schuffenhauer *et al.* studied the formation of MS_2 (M=Nb, Ta) inorganic fullerene-like structures from a gas phase reaction of MCl_5 with H_2S.[88, 163]

Upon annealing in an $H_2S + H_2/N_2$ atmosphere, nano-sized WC particles yielded WC encapsulated within IF-WS_2. WC nanoparticles, obtained by carburizing WO_3 nanoparticles, were completely converted into IF-WS_2.[164]

1.2.4.4.2 Hydrothermal method

Relatively low temperatures can be employed in solvothermal synthesis approaches. This is an advantage in avoiding the formation of high crystallinity products usually obtained at higher temperatures. High surface area MoS_2 nanomaterials could be synthesized in a hydrothermal reaction from MoO_3 and Na_2S in HCl acidic solution at 260°C or from ammonium molybdate and sulfur at 150-180°C using hydrazine as reducing agent.[165, 166] Hydrothermal annealing of MoO_3 and KSCN yielded a mixture of MoS_2 nanorods and –tubes. Contrary to other nanotubes whose walls consist of parallel layers, the walls of these tubes were built from agglomerates of small bent slabs.[167] Open-ended TiS_2-NTs were obtained from a hydrothermal reaction of $TiCl_4$ and Na_2S in THF at 200°C.[71]

1.2.4.4.3 Exfoliation

Exfoliation of MoS_2 by aid of butyl lithium (BuLi) into single layers has long been known and studied.[168-171] The instability of these exfoliated layers against folding has been used to synthesize MS_2 (M=Mo, W) nanotubes. The exfoliated layers were intercalated with transition metals. Subsequent restacking, *e.g.* via a hydrothermal route, yielded

$Mn_x(Mo_yW_{1--y})_{1-x}S_2$,
$Ni_x(Mo_yW_{1-y})_{1-x}S_2$ and
Co_xMS_2 (M=Mo, W)
nanotubes.[172-175]

1.3 Scope and aim

The synthesis methods for MQ_2 nanostructures employed so far are mainly suffering from one or more of the following problems:

- low yield,

- inhomogeneity,
- high energy required,
- costly and complicated setup,
- toxic gases,
- limited number of accessible compounds.

The aim of this work was to adapt and optimize synthesis methods for nanostructures of MoS_2 and WS_2 as model systems for the class of layered transition metal chalcogenides. These methods should allow high-yield, low-cost synthesis of homogeneous samples and preferably give access to a variety of compounds with one method. Namely (i) the solvothermal and (ii) the metal-organic chemical vapor deposition (MOCVD) approach have been chosen for this investigation.

Standard sample characterization comprised X-ray powder diffraction (XRD), scanning electron microscopy (SEM), transmission electron microscopy (TEM) in conjunction with energy dispersive X-ray spectroscopy (EDX). Complementary, differential thermal analysis (DTA/TG), specific surface area measurements (BET), Raman spectroscopy, small angle X-ray scattering (SAXS) and photoluminescence spectroscopy (PL) were employed.

In ***chapter two***, the synthesis of MoS_2 nanostructured material obtained from a solvothermal approach applying a surfactant is described and compared to materials obtained either from a classical solid state reaction or a solvothermal synthesis without addition of surfactant. DIFFaX simulations of X-ray powder patterns are employed in order to study crystallite size effects and stacking faults (3R/2H-polytype) in comparison to results obtained from transmission electron microscopy studies. Furthermore, specific surface area measurements by N_2 adsorption/desorption were conducted to evaluate the potential of these materials as catalysts in the fuel desulfurization process.

In ***chapter three***, the metal organic chemical vapor deposition (MOCVD) synthesis of IF-WS_2 is presented. The effect of the synthesis temperature is investigated and the results are compared to a two-step process, in which the MOCVD product (low temperature synthesis) is subsequently annealed in an argon atmosphere. A feasible growth mechanism for the MOCVD products is discussed.

In order to further investigate the growth mechanism of MoS_2 and WS_2 nanoparticles obtained by MOCVD, especially in comparison with the results for the two-step process (MOCVD + annealing in Ar) described in chapter three, *in situ* heating transmission electron microscopy studies were conducted and a comparative presentation of these results is given in ***chapter four***.

Attempts of synthesizing selenides by a solvothermal approach led to the discovery of a simple way to produce monodisperse ZrO_2 nanoparticles from the corresponding oxalate. The effect of synthesis temperature and autogenic pressure on the morphology and composition of the resulting zirconia material is presented in ***chapter five***.

To conclude, a summary of the main results along with some feasible future pathways will be given in ***chapter six***.

Supplementary material and a list of publications can be found in the ***appendix***.

Table 1-2. Synthesis methods for MoS_2 nano-materials.

Synthesis method	Morphology	Ref.
Arc discharge	IF	44, 49, 92, 95
Ball milling + Decomposition	NT	112
CVD	IF	115, 116, 118
	NT	117, 118
Decomposition	IF	176
	NT	65
	NS	125
Electrical heating	NT	107
Electron beam	IF	100
Exfoliation	Single layer	168-171, 177
Exfoliation-intercalation-restacking	Nanocomp	178
Hydrothermal	μT	179
	NT, NR	167
	Single layer	166
	Slabs with rolled edges	165
Inverse micelle	NC	149, 150
Laser ablation	IF	37, 86, 180
Microwave induced plasma	NC	97
	NS	98
Oxide to sulfide conversion	IF	61, 154, 181-185
	NT	186
	NS	79
	NW, NS	80
Solution	NP	187
	NS	188
Solvothermal	NS	189
Sonochemical	NS	78
Sonochemical + Template	IF	143
Spray pyrolysis	IF	105
Surfactant-based	NS	126
Template	NT	142, 144, 145, 152, 190
Vapor transport	μT	119, 191
	NT	122, 192

μT = microtube

IF = inorganic fullerene-like particles

NC = nanocluster

NP = nanoparticles

NS = nanostructures

NT = nanotubes

NW = nanowire

Table 1-3. Synthesis methods for WS_2 nano-materials.

Synthesis method	Morphology	Ref.
"Activation"	NT	193
Ball milling + Decomposition	NT	110
CVD	IF	115
	NT	114
Decomposition + Template	NT	194
Exfoliation	Single layer	168-171, 177
Hydrothermal	Single layer	166
	NT	153
Laser ablation	IF	180
	NP	90
Microwave induced plasma	IF	99
	NC	97
	NS	98
Oxide to sulfide conversion	IF	50, 61, 62, 157, 181, 182, 195-198
	NT	59, 155, 199-206
Solution	NP	187
Sonochemical	NR	106
Spray pyrolysis	IF, nanoboxes	104
Sulfidization	NT	108
Template	NT	136, 137, 139, 140, 207
Vapor transport	NT	120, 122

μT = microtube

IF = inorganic fullerene-like particles

NC = nanocluster

NP = nanoparticles

NS = nanostructures

NT = nanotubes

NW = nanowire

Table 1-4. Synthesis methods for various transition metal chalcogenide and halide nano-materials.

Compound	Synthesis method	Morphology	Ref.
CdI_2	Electron beam	IF	208
CdS	Surfactant	NT	151
CdSe	Surfactant	NT	151
GaS	Lamellar precursor	NT	209
Hf_2S	Laser ablation	IF	89
HfS_2	Decomposition	NT	132
	Microwave plasma	IF	99
$Mn_y(Mo_xW_{1-x)1-y}S_2$	Exfoliation-intercalation-restacking	NT	173, 174
$Ni_x(W_yMo_{1-y})_{1-x}S_2$	Exfoliation-adulteration-hydrothermal	NT	175
		IF	175
Ti_xMoS_2	Oxide to sulfide conversion	NT	161
Ag_xMoS_2/Au_xMoS_2	Vapor transport	NT	210
MoS_2(CNT)	Hydrothermal	NT	142
MoS_2(C)	Template	NT	147
MoS_2(Mo)	Arc discharge	IF	94
$MoSe_2$	CVD	IF	116
	Decomposition	NT	129
	Electron beam	NT	211
	Exfoliation	Single layer	168-171, 177
	Laser ablation	IF	37
	Microwave induced plasma	NC	97
	Solution	NP	187
NbS_2	Decomposition	NT	127
	Sulfurization	IF	163
Ag_xNbS_2	Electron beam irradiation	NT	103
NbS_2(CNT)	Template	NT	133, 134
	Oxide to sulfide conversion		
$NbSe_2$	Decomposition	NT	36
	Electron irradiation	NT	101, 102
	Electron irradiation	NR	101, 102
	Electron irradiation	IF	101, 102
	Surfactant Decomposition	NS	212
$NiCl_2$	Laser ablation	NT	83-85
		IF	83-85
ReS_2	Oxide to sulfide conversion	IF	156
ReS_2(CNT)		NT	141
SnS_2	Microwave	NC	97
SnS_2/SnS	Laser ablation	IF	91
	Oxide to sulfide conversion	IF	21
TaS_2	Laser ablation	IF	88
	Sulfurization	IF	88
TiS_2	Decomposition	NT	132
	Sulfurization	IF	213
$TiSe_2$	Ball milling, Annealing	NT	113
		NW	113
VS_2	Oxide to sulfide conversion	IF	21, 62
		NT	66
Co_xWS_2	Exfoliation-intercalation-hydrothermal	NT	172

Compound	Synthesis method	Morphology	Ref.
Nb_xWS_2	Oxide to sulfide conversion	NT	159, 160
Ag_xWS_2/Au_xWS_2	Vapor transport	NT	210
$WS_2(CoS)$	Arc discharge	IF	94
$WS_2(W)$	Arc discharge	IF	94
$WS_2(WC)$	Carbide to sulfide conversion	IF	164
WSe_2	Decomposition	NT	129
	Microwave induced plasma	NC	97
	Oxide to selenide conversion	IF	158
	Oxide to sulfide conversion	IF	157
	Solution	NP	187
$W_xMo_yC_zS_2$	Oxide to sulfide conversion	NT	162
ZrS_2	Decomposition	NT	130, 131
	Microwave induced plasma	NC	97
		NT	99
		NR	99

μT = microtube

IF = inorganic fullerene-like particles

NC = nanocluster

NP = nanoparticles

NS = nanostructures

NT = nanotubes

NW = nanowire

1.4 References

1. NNI, In www.nano.gov/html/about/funding.html.
2. NSF, In www.nsf.gov/crssprgm/nano/activities/finalreport_ucla.jsp.
3. Moore, G. E. *Electron.* **1965,** 38.
4. Kroto, H. W.; Heath, J. R., et al. *Nature* **1985,** 318, 162.
5. Iijima, S. *Nature* **1991,** 354, 56.
6. Seifert, G., Frauenheim, Th. *J. Kor. Phys. Soc.* **2000,** 37, 89.
7. Chopra, N. G.; Luyken, R. J., et al. *Science* **1995,** 269, 966.
8. Pokropivnyi, V. V. *Powd. Metallurgy Met. Ceram.* **2001,** 40, 485.
9. Pokropivnyi, V. V. *Powd. Metallurgy Met. Ceram.* **2001,** 40, 123.
10. Pokropivnyi, V. V. *Powd. Metallurgy Met. Ceram.* **2001,** 40, 582.
11. Spahr, M. E., Bitterli, P., Nesper, R., Müller, M., Krumeich, F., Nissen, H. U. *Angew. Chem. Int. Ed.* **1998,** 37, 1263.
12. Krumeich, F.; Muhr, H. J., et al. *J. Am. Chem. Soc.* **1999,** 121, 8324.
13. Shukoor, M. I.; Therese, H. A., et al. *Chem. Mater.* **2006,** 18, 2144.
14. Kasuga, T.; Hiramatsu, M., et al. *Langmuir* **1998,** 14, 3160.
15. Wang, X.; Sun, X., et al. *Adv. Mater.* **2003,** 15, 1442.
16. Tremel, W. *Angew. Chem. Int. Ed.* **1999,** 38, 2175.
17. Rao, C. N. R.; Nath, M. *Dalt. Trans.* **2003**, 1.
18. Tenne, R. *Mater. Sci. Forum* **1996,** 232, 275.
19. Wold, A.; Dwight, K. Synthesis, structure, and properties of selected oxides and sulfides. Chapman & Hall, Inc.: New York, 1993.
20. Shriver, D. F.; Atkins, P. W. *Inorganic chemistry*. 3. ed.; Oxford University Press: Oxford, New York, 1999.
21. Tenne, R.; Homyonfer, M., et al. *Chem. Mater.* **1998,** 10, 3225.
22. Tenne, R.; Rao, C. N. R. Philos. Trans. R. Soc. Lond. Ser. A-Math. Phys. Eng. Sci. **2004,** 362, 2099.
23. Seifert, G.; Terrones, H., et al. *Solid State Commun.* **2000,** 114, 245.
24. Seifert, G.; Terrones, H., et al. *Phys. Rev. Lett.* **2000,** 85, 146.
25. Enyashin, A. N.; Ivanovskii, A. L. *Russ. J. Inorg. Chem.* **2004,** 49, 1531.
26. Enyashin, A. N.; Ivanovskaya, V. V., et al. *Inorg. Mater.* **2004,** 40, 395.
27. Seifert, G.; Terrones, H., et al. *Solid State Commun.* **2000,** 115, 635.
28. Enyashin, A. N.; Shein, I. R., et al. *Russ. J. Inorg. Chem.* **2004,** 49, 1204.
29. Enyashin, A. N.; Ivanovskaya, V. V., et al. *J. Struct. Chem.* **2004,** 45, 547.

30. Enyashin, A. N.; Shein, I. R., et al. *Internet Electr. J. Molec. Design* **2005,** 4, 316.
31. Ivanovskaya, V. V.; Enyashin, A. N., et al. *Internet Electr. J. Molec. Design* **2003,** 2, 499.
32. Ivanovskaya, V. V.; Enyashin, A. N., et al. *J. Struct. Chem.* **2004,** 45, 151.
33. Ivanovskaya, V. V.; Enyashin, A. N., et al. *Russ. J. Inorg. Chem.* **2004,** 49, 244.
34. Scheffer, L.; Rosentzveig, R., et al. *Phys. Chem. Chem. Phys.* **2002,** 4, 2095.
35. Nemanic, V.; Zumer, M., et al. *Appl. Phys. Lett.* **2003,** 82, 4573.
36. Nath, M.; Kar, S., et al. *Chem. Phys. Lett.* **2003,** 368, 690.
37. Parilla, P. A.; Dillon, A. C., et al. *J. Phys. Chem. B* **2004,** 108, 6197.
38. Frey, G. L.; Tenne, R., et al. *J. Mater. Res.* **1998,** 13, 2412.
39. Kopnov, F.; Yoffe, A., et al. *phys. stat. sol. (b)* **2006,** 243, 1229.
40. Enyashin, A. N.; Ivanovskii, A. L. *Russ. J. Phys. Chem.* **2005,** 79, 940.
41. Joly-Pottuz, L.; Martin, J. M., et al. *J. Appl. Phys.* **2006,** 99, 023524/1.
42. Joly-Pottuz, L.; Dassenoy, F., et al. *Tribology Letters* **2005,** 18, 477.
43. Huang, H. D.; Tu, J. P., et al. *Tribol. Lett.* **2005,** 20, 247.
44. Chhowalla, M.; Amaratunga, G. A. J. *Nature* **2000,** 407, 164.
45. Rapoport, L.; Leshchinsky, V., et al. *Wear* **2002,** 252, 518.
46. Katz, A.; Redlich, M., et al. *Tribol. Lett.* **2006,** 21, 135.
47. Prasad, S.; Zabinski, J. *Nature* **1997,** 387, 761.
48. Rapoport, L.; Bilik, Y., et al. *Nature* **1997,** 387, 791.
49. Hu, J. J.; Zabinski, J. S. *Tribol. Lett.* **2005,** 18, 173.
50. Greenberg, R.; Halperin, G., et al. *Tribol. Lett.* **2004,** 17, 179.
51. Drummond, C.; Alcantar, N., et al. *Adv. Funct. Mater.* **2001,** 11, 348.
52. Golan, Y.; Drummond, C., et al. *Adv. Mater.* **1999,** 11, 934.
53. Cizaire, L.; Vacher, B., et al. *Surf. Coat. Technol.* **2002,** 160, 282.
54. Leshchinsky, V.; Popovitz-Biro, R., et al. *J. Mater. Sci.* **2004,** 39, 4119.
55. Schuffenhauer, C.; Wildermuth, G., et al. *Phys. Chem. Chem. Phys.* **2004,** 6, 3991.
56. Su, F.-H.; Zhang, Z.-Z., et al. *Mater. Sci. Eng. A* **2005,** A392, 359.
57. Zhu, Y. Q.; Sekine, T., et al. *J. Am. Chem. Soc.* **2005,** 127, 16263.
58. Zhu, Y. Q.; Sekine, T., et al. *J. Am. Chem. Soc.* **2003,** 125, 1329.
59. Kaplan-Ashiri, I.; Cohen, S. R., et al. *J. Mater. Res.* **2004,** 19, 454.
60. Rothschild, A.; Cohen, S. R., et al. *Appl. Phys. Lett.* **1999,** 75, 4025.
61. Zak, A.; Feldman, Y., et al. *J. Am. Chem. Soc.* **2002,** 124, 4747.
62. Homyonfer, M.; Alperson, B., et al. *J. Am. Chem. Soc.* **1997,** 119, 2693.

63. Shimoda, H.; Gao, B., et al. *Physica B* **2002,** 323, 133.
64. Shimoda, H.; Gao, B., et al. *Phys. Rev. Lett.* **2002,** 88, 015502/1.
65. Chen, J.; Kuriyama, N., et al. *J. Am. Chem. Soc.* **2001,** 123, 11813.
66. Therese Helen, A.; Rocker, F., et al. *Angew. Chem. Int. Ed.* **2004,** 44, 262.
67. Gao, B.; Kleinhammes, A., et al. *Chem. Phys. Lett.* **1999,** 307, 153.
68. Dominko, R.; Gaberscek, M., et al. *AIP Conf. Proc.* **2002,** 633, 624.
69. Dominko, R.; Gaberscek, M., et al. *Electrochim. Acta* **2003,** 48, 3079.
70. Dominko, R.; Arcon, D., et al. *Adv. Mater.* **2002,** 14, 1531.
71. Chen, J.; Tho, Z. L., et al. *Angew. Chem. Int. Edit.* **2003,** 42, 2147.
72. Tao, Z. L.; Xu, L. N., et al. *Chem. Commun.* **2004**, 2080.
73. Tao, Z.; Gao, F., et al. *Nankai Daxue Xuebao, Ziran Kexueban* **2005,** 38, 28.
74. Raybaud, P.; Hafner, J., et al. *Phys. Rev. Lett.* **1998,** 80, 1481.
75. Salmeron, M.; Somorjai, G. A., et al. *Chem. Phys. Lett.* **1982,** 90, 105.
76. Tauster, S. J.; Pecoraro, T. A., et al. *J. Catal.* **1980,** 63, 515.
77. Jiao, H.; Li, Y.-W., et al. *J. Am. Chem. Soc.* **2001,** 123, 7334.
78. Mdleleni, M. M.; Hyeon, T., et al. *J. Am. Chem. Soc.* **1998,** 120, 6189.
79. Iwata, Y.; Sato, K., et al. *Catal. Today* **1998,** 45, 353.
80. Camacho-Bragado, G. A.; Elechiguerra, J. L., et al. *J. Catal.* **2005,** 234, 182.
81. Thomazeau, C.; Geantet, C., et al. *Oil Gas Sci. Technol.* **2005,** 60, 781.
82. Chen, J.; Li, S.-L., et al. *Chem. Commun.* **2002**, 1722.
83. Hacohen, Y. R.; Grunbaum, E., et al. *Nature* **1998,** 395, 336.
84. Hacohen, Y. R.; Popovitz-Biro, R., et al. *Adv. Mater.* **2002,** 14, 1075.
85. Hacohen, Y. R.; Popovitz-Biro, R., et al. *Phys. Chem. Chem. Phys.* **2003,** 5, 1644.
86. Parilla, P. A.; Dillon, A. C., et al. *Nature* **1999,** 397, 114.
87. Sen, R.; Govindaraj, A., et al. *Chem. Phys. Lett.* **2001,** 340, 242.
88. Schuffenhauer, C.; Parkinson, B. A., et al. *Small* **2005,** 1, 1100.
89. Nath, M.; Rao, C. N. R., et al. *Chem. Mater.* **2004,** 16, 2238.
90. Hu, J. J.; Zabinski, J. S., et al. *J. Phys. Chem. B* **2006,** 110, 8914.
91. Hong, S. Y.; Popovitz-Biro, R., et al. *J. Am. Chem. Soc.* **2003,** 125, 10470.
92. Hu, J. J.; Bultman, J. E., et al. *Tribol. Lett.* **2004,** 17, 543.
93. Sano, N.; Wang, H., et al. *Chem. Phys. Lett.* **2003,** 368, 331.
94. Si, P. Z.; Zhang, M., et al. *J. Mater. Sci.* **2005,** 40, 4287.
95. Alexandrou, I.; Sano, N., et al. *Nanotechn.* **2003,** 14, 913.
96. Hu, J. J.; Sanders, J. H., et al. *J. Mater. Res.* **2006,** 21, 1033.

97. Vollath, D.; Szabo, D. V. *Acta Mater.* **2000,** 48, 953.
98. Vollath, D.; Szabo, D. V. *Mater. Lett.* **1998,** 35, 236.
99. Brooks, D. J.; Douthwaite, R. E., et al. *Nanotechn.* **2006,** 17, 1245.
100. Jose-Yacaman, M.; Lopez, H., et al. *Appl. Phys. Lett.* **1996,** 69, 1065.
101. Galvan, D. H.; Kim, J. H., et al. *Full. Sci. Techn.* **2000,** 8, 143.
102. Galvan, D. H.; Kim, J.-H., et al. *Full. Sci. Techn.* **2001,** 9, 225.
103. Remskar, M.; Mrzel, A., et al. *Adv. Mater.* **2002,** 14, 680.
104. Bastide, S.; Duphil, D., et al. *Adv. Mater.* **2006,** 18, 106.
105. He, D.; Yin, G., et al., 1002-8674 1752023, **2006**.
106. Nikitenko, S. I.; Koltypin, Y., et al. *J. Mater. Chem.* **2002,** 12, 1450.
107. Hsu, W. K.; Chang, B. H., et al. *J. Am. Chem. Soc.* **2000,** 122, 10155.
108. Tenne, R.; Margulis, L., et al. *Nature* **1992,** 360, 444.
109. Gaffet, E.; Abdellaoui, M., et al. *Mater. Trans. JIM* **1995,** 36, 198.
110. Chen, J.; Li, S.-L., et al. *Chem. Mater.* **2003,** 15, 1012.
111. Chen, J.; Li, S., et al. *Sci. China, Ser. B* **2003,** 46, 191.
112. Chen, J.; Li, S. L., et al. *J. Alloys Compd.* **2003,** 356-357, 413.
113. Chen, J.; Tao, Z. L., et al. *Adv. Mater.* **2003,** 15, 1379.
114. Ge, J.-P.; Wang, J., et al. *Chem. Eur. J.* **2004,** 10, 3525.
115. Li, X.-L.; Ge, J.-P., et al. *Chem. Eur. J.* **2004,** 10, 6163.
116. Etzkorn, J.; Therese, H. A., et al. *Adv. Mater.* **2005,** 17, 2372.
117. Gao, B.; Xu, Q.-m., et al. *Gongneng Cailiao Yu Qijian Xuebao* **2006,** 12, 143.
118. Zhang, H.-X.; Ge, J.-P., et al. *Nanotechn.* **2006,** 17, S253.
119. Remskar, M.; Skraba, Z., et al. *Kovine, Zlitine, Tehnologije* **1997,** 31, 247.
120. Remskar, M.; Skraba, Z., et al. *Appl. Phys. Lett.* **1999,** 74, 3633.
121. Remskar, M.; Skraba, Z., et al. *Adv. Mater.* **1998,** 10, 246.
122. Remskar, M.; Mrzel, A. *Vacuum* **2003,** 71, 177.
123. Remskar, M., Mrzel, A., Skraba, Z., Jesih, A., Demsar, J., Stadelman, P., Levy, F., Mihailovic, D. *Science* **2001,** 292, 479.
124. Remskar, M.; Skraba, Z., et al. *Surf. Rev. Lett.* **1999,** 6, 1283.
125. Leist, A.; Stauf, S., et al. *J. Mater. Chem.* **1998,** 8, 241.
126. Afanasiev, P.; Xia, G. F., et al. *Chem. Mater.* **1999,** 11, 3216.
127. Nath, M.; Rao, C. N. R. *J. Am. Chem. Soc.* **2001,** 123, 4841.
128. Nath, M.; Govindaraj, A., et al. *Adv. Mater.* **2001,** 13, 283.
129. Nath, M.; Rao, C. N. R. *Chem. Commun.* **2001**, 2236.

130. Nath, M.; Rao, C. N. R. *Pure Appl. Chem.* **2002,** 74, 1545.
131. Nath, M.; Rao, C. N. R. *Angew. Chem. Int. Ed.* **2002,** 41, 3451.
132. Nath, M., Mukhopadhyay, K., Rao, C. N. R. *Chem. Phys. Lett.* **2002,** 352, 163.
133. Zhu, Y. Q.; Hsu, W. K., et al. *Chem. Commun.* **2001**, 2184.
134. Zhu, Y. Q.; Hsu, W. K., et al. *J. Phys. Chem. B* **2002,** 106, 7623.
135. Whitby, R. L. D.; Hsu, W. K., et al. *Chem. Phys. Lett.* **2002,** 359, 68.
136. Whitby, R. L. D.; Hsu, W. K., et al. *ChemPhysChem* **2001,** 2, 620.
137. Whitby, R. L. D.; Hsu, W. K., et al. *Appl. Phys. Lett.* **2001,** 79, 4574.
138. Whitby, R. L. D.; Hsu, W. K., et al. *Rec. Res. Develop. Appl. Phys.* **2002,** 5, 409.
139. Whitby, R. L. D.; Hsu, W. K., et al. *Chem. Phys. Lett.* **2002,** 359, 121.
140. Whitby, R. L. D.; Hsu, W. K., et al. *Chem. Mater.* **2002,** 14, 2209.
141. Brorson, M.; Hansen, T. W., et al. *J. Am. Chem. Soc.* **2002,** 124, 11582.
142. Ma, L.; Chen, W.-X., et al. *Nanotechn.* **2006,** 17, 571.
143. Dhas, N. A.; Suslick, K. S. *J. Am. Chem. Soc.* **2005,** 127, 2368.
144. Che, R. C.; Bai, N., et al. *Appl. Phys. Lett.* **2003,** 83, 3561.
145. Zelenski, C. M.; Dorhout, P. K. *J. Am. Chem. Soc.* **1998,** 120, 734.
146. Loh Kian, P.; Zhang, H., et al. *J. Phys. Chem. B* **2006,** 110, 1235.
147. Reza-San German, C.; Santiago, P., et al. *J. Phys. Chem. B* **2005,** 109, 17488.
148. Xiong, Y., Xie,Y., Li, Zh., Li, X., Zhang, R. *Chem. Phys. Lett.* **2003,** 382, 180.
149. Wilcoxon, J. P.; Samara, G. A. *Phys. Rev. B* **1995,** 51, 7299.
150. Chikan, V.; Kelley, D. F. *J. Phys. Chem. B* **2002,** 106, 3794.
151. Rao, C. N. R., Govindaraj, A., Leonard Deepak, F., Gunari, N. A., Nath, M. *Appl. Phys. Lett.* **2001,** 78, 1853.
152. Lavayen, V.; Mirabal, N., et al. *AIP Conf. Proc.* **2003,** 685, 473.
153. Therese, H. A.; Li, J., et al. *Solid State Sci.* **2005,** 7, 67.
154. Margulis, L.; Salitra, G., et al. *Nature* **1993,** 365, 113.
155. Zhu, Y. Q.; Hsu, W. K., et al. *Chem. Mater.* **2000,** 12, 1190.
156. Coleman, K. S., Sloan, J., Hanson, N. A., Brown, G., Clancy, G. P., Terrones, M., Terrones, H., Green, M. L. H. *J. Am. Chem. Soc.* **2002,** 124, 11580.
157. Sloan, J.; Hutchison, J. L., et al. *J. Solid State Chem.* **1999,** 144, 100.
158. Tsirlina, T.; Feldman, Y., et al. *Full. Sci. Techn.* **1998,** 6, 157.
159. Zhu, Y. Q.; Hsu, W. K., et al. *Chem. Commun.* **2001**, 121.
160. Zhu, Y. Q.; Hsu, W. K., et al. *Chem. Phys. Lett.* **2001,** 342, 15.
161. Hsu, W. K.; Zhu, Y. Q., et al. *Adv. Funct. Mater.* **2001,** 11, 69.

162. Hsu, W. K.; Zhu, Y. G., et al. *Chem. Mater.* **2000,** 12, 3541.
163. Schuffenhauer, C.; Popovitz-Biro, R., et al. *J. Mater. Chem.* **2002,** 12, 1587.
164. Rothschild, A.; Tenne, R., et al. *Chem. Commun.* **1999**, 363.
165. Li, W. J.; Shi, E. W., et al. *J. Cryst. Growth* **2003,** 250, 418.
166. Peng, Y. Y.; Meng, Z. Y., et al. *Chem. Lett.* **2001**, 772.
167. Tian, Y.; He, Y., et al. *Mater. Chem. Phys.* **2004,** 87, 87.
168. Frindt, R. F. *J. Appl. Phys.* **1966,** 37, 1928.
169. Frindt, R. F.; Arrott, A. S., et al. *J. Appl. Phys.* **1991,** 70, 6224.
170. Divigalpitiya, R. W. M.; Frindt, R. F., et al., 90-300290 382339, **1990**.
171. Yang, D.; Frindt, R. F. *J. Phys. Chem. Solids* **1996,** 57, 1113.
172. Wang, S.; Li, G., et al. *Mater. Lett.* **2006,** 60, 815.
173. Li, G.-H.; Xu, Z.-D., et al. *Gaodeng Xuexiao Huaxue Xuebao* **2003,** 24, 2155.
174. Li, G.-H.; Zeng, Y.-W., et al. *Wuji Cailiao Xuebao* **2004,** 19, 481.
175. Li, G.-H.; Ma, C.-A., et al. *Wuji Cailiao Xuebao* **2006,** 21, 70.
176. Homyonfer, M., Mastai, Y., Hershfinkel, M., Volterra, V., Hutchison, J.L., Tenne, R. *J. Am. Chem. Soc.* **1996,** 118, 7804.
177. Yang, D.; Frindt, R. F. *Am. Chem. Soc. Preprints* **1994,** 39, 612.
178. Sanchez, V.; Benavente, E., et al. *Chem. Mater.* **1999,** 11, 2296.
179. Afanasiev, P.; Geantet, C., et al. *Chem. Commun.* **2000**, 1001.
180. Sen, R.; Govindaraj, A., et al. *Chem. Phys. Lett.* **2001,** 340, 242.
181. Zak, A.; Feldman, Y., et al. *AIP Conf. Proc.* **2002,** 633, 67.
182. Feldman, Y.; Frey, G. L., et al. *J. Am. Chem. Soc.* **1996,** 118, 5362.
183. Feldman, Y.; Margulis, L., et al. *High. Temp. Mater. Proc.* **1996,** 15, 163.
184. Li, X. L.; Li, Y. D. *Chem. Eur. J.* **2003,** 9, 2726.
185. Frey, G. L.; Tenne, R., et al. *Phys. Rev. B.* **1999,** 60, 2883.
186. Feldman, Y.; Wasserman, E., et al. *Science* **1995,** 267, 222.
187. Duphil, D.; Bastide, S., et al. *Nanotechn.* **2004,** 15, 828.
188. Afanasiev, P.; Rawas, L., et al. *Mater. Chem. Phys.* **2002,** 73, 295.
189. Berntsen, N.; Gutjahr, T., et al. *Chem. Mater.* **2003,** 15, 4498.
190. Loh, K. P.; Zhang, H., et al. *J. Phys. Chem. B* **2006,** 110, 1235.
191. Remskar, M.; Skraba, Z., et al. *Surf. Sci.* **1999,** 433-435, 637.
192. Remskar, M.; Mrzel, A., et al. *Science* **2001,** 292, 479.
193. Mackie, E. B.; Galvan, D. H., et al. *Adv. Mater.* **2000,** 12, 495.
194. Li, C.; Yan, K., et al. *Mater. Sci. Forum* **2005,** 475-479, 3521.

195. Luttrell, R. D.; Brown, S., et al. *Phys. Rev. B* **2006,** 73, 035410/1.
196. Feldman, Y., Lyakhovitskaya, V., Tenne, R. *J. Am. Chem. Soc.* **1998,** 120, 4176.
197. Chen, W. X.; Tu, J. P., et al. *Chin. Chem. Lett.* **2003,** 14, 312.
198. Feldman, Y.; Zak, A., et al. *Solid State Sci.* **2000,** 2, 663.
199. Kaplan-Ashiri, I.; Cohen, S. R., et al. *Proc. Natl. Acad. Sci. U. S. A.* **2006,** 103, 523.
200. Dong, L.; Maiz, A., et al. *Mater. Res. Soc. Symp. Proc.* **2004,** 794, 29.
201. Rosentsveig, R.; Margolin, A., et al. *Appl. Phys. A* **2002,** 74, 367.
202. Margolin, A.; Rosentsveig, R., et al. *J. Mater. Chem.* **2004,** 14, 617.
203. Rosentsveig, R.; Margolin, A., et al. *Chem. Mater.* **2002,** 14, 471.
204. Rothschild, A.; Frey, G. L., et al. *Mater. Res. Innov.* **1999,** 3, 145.
205. Rothschild, A.; Popovitz-Biro, R., et al. *J. Phys. Chem. B* **2000,** 104, 8976.
206. Rothschild, A.; Sloan, J., et al. *J. Am. Chem. Soc.* **2000,** 122, 5169.
207. Li, Y. D.; Li, X. L., et al. *J. Am. Chem. Soc.* **2002,** 124, 1411.
208. Popovitz-Biro, R.; Sallacan, N., et al. *J. Mater. Chem.* **2003,** 13, 1631.
209. Hu, P. A.; Liu, Y. Q., et al. *Appl. Phys. A* **2005,** 80, 1413.
210. Remskar, M.; Skraba, Z., et al. *Adv. Mater.* **2000,** 12, 814.
211. Galvan, D. H.; Rangel, R., et al. *Fuller. Nanotub. Carbon Nanostruct.* **2002,** 10, 127.
212. Sekar, P.; Greyson, E. C., et al. *J. Am. Chem. Soc.* **2005,** 127, 2054.
213. Margolin, A.; Popovitz-Biro, R., et al. *Current Nanosci.* **2005,** 1, 253.

2 A solvothermal route to high surface area nanostructured MoS_2

2.1 Introduction

The layered structure of the early transition metal dichalcogenides MQ_2 easily lend themselves to the formation of a variety of nanostructures. A number of years ago, Divigalpitiya *et al.*[1] showed that MoS_2 can be separated sheet-by-sheet by a process of exfoliation, and then restacked with organic molecules in order to obtain interesting hybrid materials. The huge body of work on carbon nanostructures, particularly the discovery of carbon nanotubes[2] and carbon onions[3] encouraged Tenne and coworkers[4, 5] to pursue related MQ_2-based, concentric, closed-shell materials, laying the foundations for an entire area of nanostructures based on layered inorganic materials.[6] A characteristic feature of closed shell MQ_2-derived structures is that they require high temperatures of preparation (~1100 K) for the ends of single MQ_2 sheets to "knit" together through the formation of rhomboidal and triangular point defects which provide curvature to the otherwise flat MQ_2 sheet.[7] Low preparation temperatures (less than 700 K) have been attempted by many researchers. While these do not usually result in perfect closed-shell structures, interesting nano architectures do arise. For example, Leist *et al.*[8] showed that a number of different ammonium thiomolybdates could be decomposed by heating in sealed quartz tubes and in dynamic vacuum (up to 673 K) resulted in onion like lamellae of MoS_2, but with open edges. It was also noted that the precursor $(NH_4)_2Mo_3S_{13} \cdot xH_2O$ shows decomposition behavior that is distinct from other ammonium thiomolybdates, in that its conversion to MoS_2 is characterized by a sharp exotherm. The explanation provided for this was the topochemical nature of the reaction resulting from structural relations between precursor and product. Zelenski and Dorhout[9] used alumina membranes as templates to decompose various ammonium thiomolybdates and obtained tubular nanostructures comprising linked spheres of lamellar MoS_2. Bezhverkhy *et al.*[10] have prepared highly disperse MoS_2 from an aqueous, pH adjusted solution of ammonium thiomolybdate and hydrazine. The hydrothermal reaction of MoO_3 and Na_2S in HCl at 533 K results in bent MoS_2 sheets with a high surface area.[11] Afanasiev *et al.*[12] studied the effect of the surfactant cetyltrimethylammonium chloride on the thermal decomposition of $(NH_4)MoS_4$ using a two-step reaction. They obtained single MoS_2 layers at intermediate reaction temperatures (~ 723 K) with very high surface areas of about 210 m^2/g. Similar sheet-like structures have been obtained by Peng *et al.*[13] by the reductive hydrothermal reaction of molybdates with sulfur between 423 K and 453 K. Iwata *et al.*[14] have prepared MoS_2 hydrogenation and

hydrodesulfurization catalysts by thermal decomposition of ammonium thiomolybdate under 10% H_2S-H_2. It is of interest to be able to prepare lamellar MoS_2 nanostructures in organic solvents, because of ease of incorporation of structure-directing template molecules and surfactants. Surfactant molecules are well-known in their ability to control crystallite morphology, and in rare cases, the aggregation of crystallites.[15] Using solvothermal toluene as a reaction medium allows relatively high temperatures (required for crystallization) to be easily achieved, in an inexpensive and relatively non-toxic solvent. In the presence of capping agents, solvothermal toluene can be used to prepare oxide and chalcogenide nanoparticles, either through direct reaction or through decomposition of precursors.[16-18] We present here our results on the use of solvothermal toluene at 653 K to decompose the thiomolybdate precursor $(NH_4)_2Mo_3S_{13} \cdot xH_2O$, in the absence and presence of the surfactant cetyltrimethylammonium bromide (CTAB). We have employed novel and inexpensive means of obtaining the solvothermal conditions (using a simple Swagelok™-based autoclave). The samples have been characterized by X-ray diffraction in conjunction with DIFFaX simulations,[19, 20] by transmission electron microscopy, and by surface area measurements. These studies indeed reflect the distinct natures of the products obtained by solvothermal decomposition as opposed to decompositions in static vacuum. The influence of the surfactant is also clearly manifested.

2.2 Experimental Details

2.2.1 Synthesis

The $(NH_4)_2Mo_3S_{13} \cdot xH_2O$ precursor was prepared as described in the literature[21] with some modifications as suggested by Leist.[8] Saturated $(NH_4)_2S_x$ (ammonium polysulfide) solution was prepared by bubbling a moderate flow of H_2S through a suspension of 80 g of sulfur in 400 cm^3 of 10% NH_3 solution for 3 hours. The exothermic reaction yielded a dark red solution which was prepared just before being used, and filtered to remove unreacted sulfur and polysulfide precipitates. 240 cm^3 of $(NH_4)_2S_x$ solution was then added to a solution of 8 g of $(NH_4)_6(Mo_7O_{24}) \cdot 4H_2O$ in 40 cm^3 of H_2O, and the mixture heated under reflux for 3 days at 363-373 K. The warm solution was filtered and the precipitated product washed thoroughly with a $(NH_4)_2S_x$ solution, H_2O, CS_2 and EtOH (in that order) and then dried under vacuum. Identity was confirmed from the powder X-ray diffraction (XRD) pattern acquired on a Bruker D5000 diffractometer (CuK_α, 40 kV, 40 mA, transmission Bragg-Brentano geometry). In this paper we compare results from two different synthetic routes. Preliminary experiments suggested that the precursor $(NH_4)_2Mo_3S_{13} \cdot xH_2O$ could be decomposed by heating at temperatures as low as 653 K for 24 h in a static vacuum (sealed quartz tube). Therefore,

samples were prepared by decomposing the precursor by heating at 653 K for 1 day, using the following conditions: (i) a sealed quartz tube: 300 mg of precursor was placed in an evacuated sealed quartz tube (10 to 12 cm in length, 7 and 9 mm inner and outer diameter, respectively) and heated in a Thermolyne 1300 furnace. This sample is henceforth referred to as Q. (ii) Solvothermal preparation: 300 mg of precursor taken in 3 cm^3 of toluene (EM Science, 99.5%+, GR ACS) was heated in a sealed autoclave of 10 cm^3 total volume. The autoclave comprised an SS316 tube, about 17 cm in length and 0.3" and 0.5" in diameter (inner and outer, respectively) with the ends closed by Swagelok™ caps made from SS316 (SS-810-C, 0.5"). This sample is referred to as S. (iii) Preparations with surfactant: To the solvothermal preparation described above, 50 mg of CTAB was added at before sealing the autoclave. This sample is referred to as C. In one case, 300 mg of CTAB was used. All the C samples were thoroughly washed between 5 and 10 times, each time with 50 mL of isopropanol. After the last wash, the samples were dried at 343 K in air. *Caution*: Heating the closed autoclave results in very high autogenous pressure build up. It is important to use relatively small filling fractions in the autoclave (here approximately 30 volume %). The autoclaves were heated by placing in a cold Thermolyne furnace that in turn was placed in an explosion proof cabinet. The furnace was equipped with an external (outside the cabinet) temperature controller. The cabinet was not opened when the furnace temperature was above 373 K.

2.2.2 Characterization

The products of decomposition were characterized by XRD on a Scintag-X2 diffractometer (CuK_α, 45 kV, 35 mA) operated in reflection Bragg-Brentano geometry, and by transmission electron microscopy (TEM) on a JEOL 2000 (200 kV acceleration voltage) equipped with energy dispersive X-ray spectroscopy (EDS). Samples for TEM were prepared by depositing drops of an ethanolic suspension of the decomposition products (obtained by sonication) on to carbon-coated copper grids. Thermogravimetry analysis (TGA) was performed on a Mettler Toledo TGA/SDTA 851e and BET specific surface area measurements on a Micromeritics ASAP2000 with N_2 as adsorption gas. Samples for surface area measurements were first treated by heating for 2 h at 623 K under N_2 purge on a Micromeritics FlowPrep060, followed by vacuum degassing overnight on the ASAP2000 at 623 K. For each of the different preparation conditions, several samples were prepared and their powder XRD patterns recorded as a means of ensuring reproducibility of the preparation conditions.

2.3 Results and Discussion

Figure 2-1 displays powder XRD patterns of the products obtained from the three different routes described above, as well as a Rietveld simulation[22] of the powder XRD profile of crystalline 2H-MoS_2. Profile parameters used in the Rietveld simulation corresponded to what is typically obtained from the specific diffractometer.

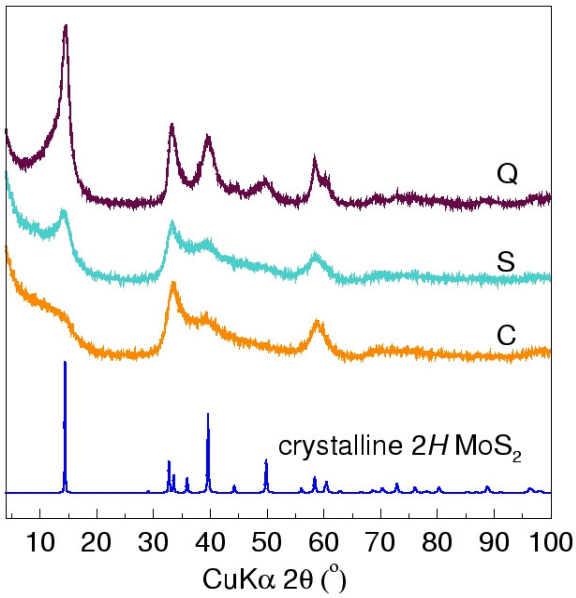

Figure 2-1. Powder X-ray diffraction patterns of the product obtained from decomposition of $(NH_4)_2Mo_3S_{13} \cdot xH_2O$ at 653 K for 24 h in an evacuated, sealed quartz tube (Q), in toluene (S), and in toluene in the presence of CTAB (C). A simulated XRD pattern of crystalline 2H-MoS_2 is also displayed.

In all cases 2H-MoS_2 (JCPDS Card No. 37-1492) was obtained. The patterns of the three samples show broadening of the peaks which is typical for nanostructured phases, as well as the sawtooth patterns characteristic of layered disordered materials.[23] The solvothermal products (S and C) display patterns which are quite distinct from the product obtained after decomposition of the precursor in a sealed quartz tube. Notably, the (002) reflection at about 13° (2θ) is much less pronounced in S and has almost no intensity in C. A more detailed analysis of the nanostructures based on DIFFaX simulations of powder XRD patterns is presented in what follows. Figure 2-2 shows thermogravimetric curves (in N_2) of the three MoS_2 products Q, S and C.

The product from the sealed quartz tube reaction (Q) has a large mass loss that we ascribe to adsorbed sulfur, because, for this sample, the purging and degassing associated with the BET surface area measurements resulted in yellow sulfur deposits on the walls of the vial. Such deposits were not observed for the other samples. It is possible that in static vacuum, there is no process of cleaning the high surface area MoS_2 that is formed, unlike in the solvothermal preparations where the samples are “washed” by the solvent during preparation.

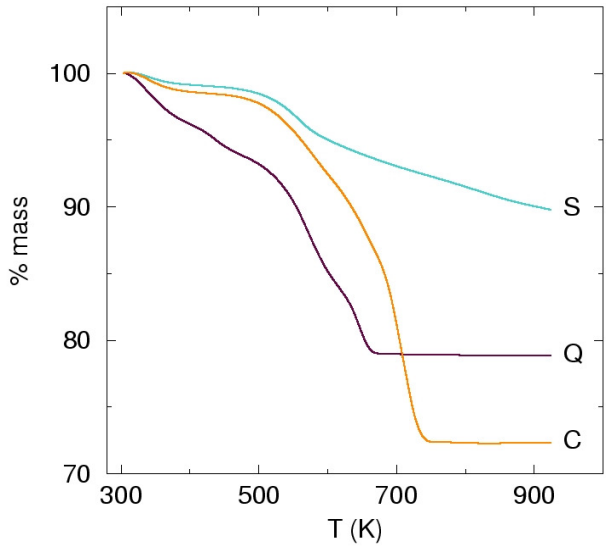

Figure 2-2. Thermogravimetric curves under flowing N_2 of the products Q, S and C.

The mass loss of the solvothermally prepared sample is associated with small amounts of absorbed matter (perhaps products of the decomposition of the precursor) and indeed, the extent of the mass loss is the smallest in this sample. The sample prepared in the presence of CTAB (C) shows the largest mass loss (about 27 mass %).

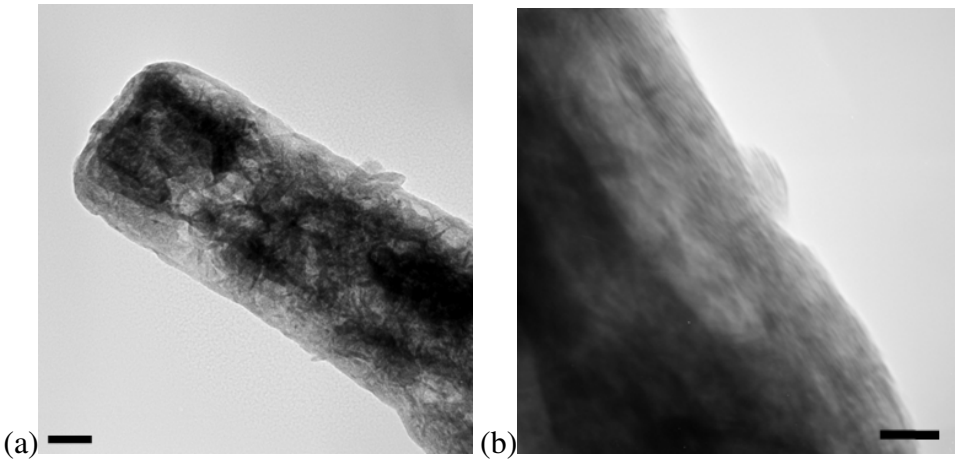

Figure 2-3. TEM images of the product Q. The scale bars are (a) 50 nm and (b) 10 nm.

Up to nearly 580 K, the mass loss in sample C is quite similar to what is seen for S, and perhaps corresponds to adsorbed material. After this temperature, there is a sharper fall in mass corresponding to the strip-off of CTAB adsorbed in the sample. This CTAB that was not removed by the extensive washing is intrinsic to the nanostructure. However, CTAB could not be detected in EDS analysis of the C sample.

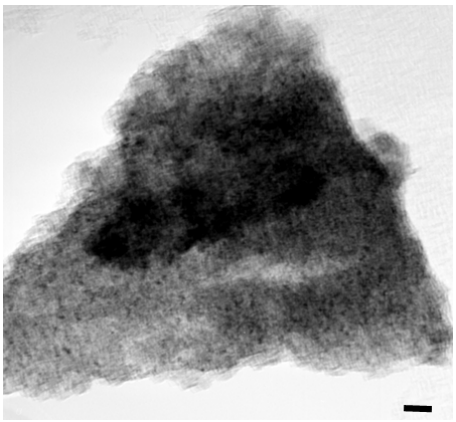

Figure 2-4. TEM image of the product S. The scale bar is 20 nm.

Transmission electron micrographs of the different decomposition products are displayed in Figure 2-3, Figure 2-4, and Figure 2-5. The samples obtained from sealed-tube decompositions (Q) retain the needle-like morphology (Figure 2-3(a)) of the starting material for which scanning electron microscope images have been presented previously.[8] A closer examination at high magnification reveals characteristic MoS_2 lamellae, with sheets separated by about 7 Å. The sample obtained by solvothermal decomposition in pure toluene (Figure 2-4) is seen to be quite distinct from Q.

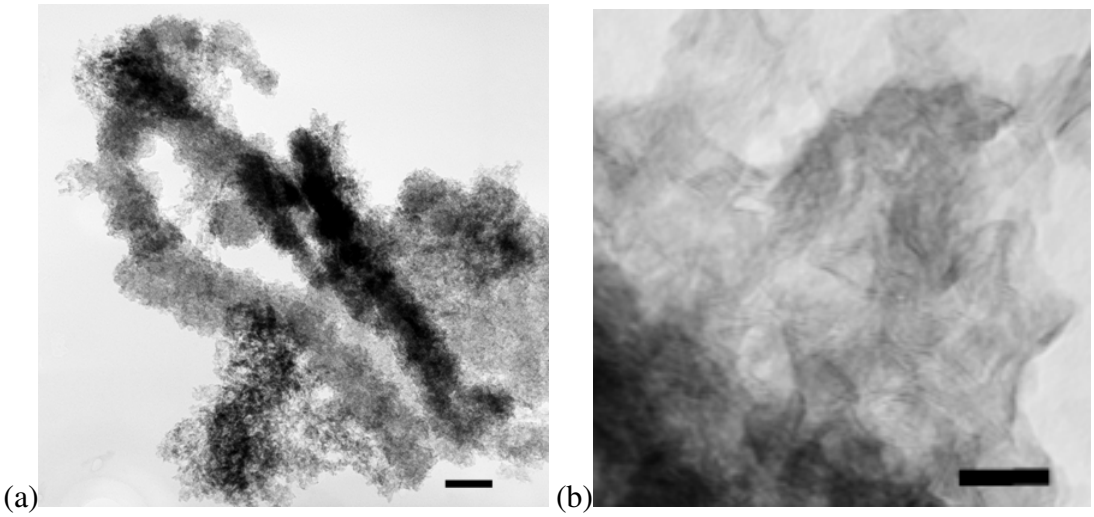

Figure 2-5. TEM images of the product C. The scale bars are (a) 100 nm and (b) 10 nm.

The morphology does not display the needle-like shapes seen for the Q sample, but instead displays isotropic agglomerates. Towards the edges of the agglomerate, the sheet-like nature of the constituent MoS_2 becomes apparent. When the surfactant CTAB is added to the solvothermal preparation, we once again observe in the TEM that the morphologies of the MoS_2 so formed (C) are quite distinct from what is obtained from the sealed-quartz tube de-

composition Q. Some portions of the C samples that we studied by TEM resembled images that were obtained from the S sample. In addition, certain regions of the TEM grid displayed string-like structures (Figure 2-5(a)). We propose that aggregation of surfactant molecules is responsible for the formation of such unusual morphologies. Examined in higher magnification (Figure 2-5(b)), the sample C shows bent MoS_2 lamellae with an interlayer spacing of about 7 Å. Whereas in Q the regions of stacked sheets were up to 100 nm long with stacking perpendicular to the needle surface, these regions are significantly shorter for C and their orientation is completely at random with respect to other similar stackings. TEM studies, while providing details of morphology, can be unsatisfactory in terms of how representative they are with respect to the entire sample. In order to arrive at a quantitative description of the different MoS_2 samples, we have used the DIFFaX program[19, 20] to generate different stackings of individual MoS_2 lamellae and simulated powder X-ray diffraction patterns from the structures so obtained. Many series of DIFFaX simulations were carried out, varying the in-plane extent of the layer, the number of layers, and finally the proportion of faulted stackings, *e.g.* stackings that ignore orientational relationships between layers, to the simple ABAB stacking of crystalline 2H-MoS_2. Those that matched most closely (visual comparison) with the corresponding experimental X-ray diffraction patterns are displayed in Figure 2-6 (for Q) and Figure 2-7 (for C).

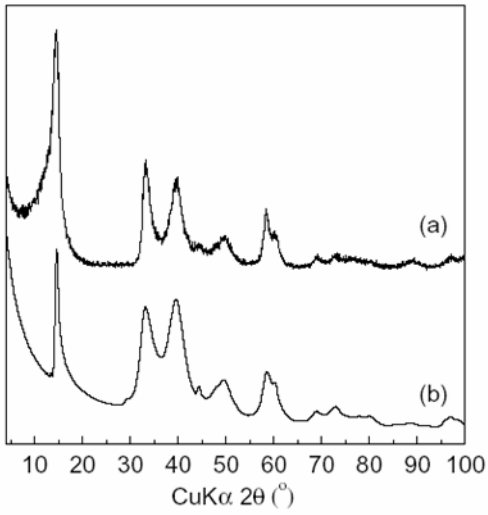

Figure 2-6. Powder X-ray diffraction patterns of (a) the product Q and (b) DIFFaX simulation of 20 layers of MoS_2, each 10 x 10 nm on side and using a probability of 60% random stacking.

Each DIFFaX simulation is time consuming and the nature of the parameters that can be varied does not permit the program being used as a "best-fit"' tool. By choosing 20 layers with a rather small layer (in-plane) size of (10 x 10 nm) and a probability of 60% completely random stacking, we could obtain a simulated pattern which showed the characteristics of the

Q experimental XRD pattern: The relatively sharp and intense (002)-reflection corresponding to the number of layers, and the sawtooth peak shape resulting from the stacking disorder. Random stacking was necessary to obtain the correct relative intensities. It also contributed to the peak broadening, and the peak shape. To simulate the C experimental pattern far fewer (five) layers with the same in-plane size (10 x 10 nm), as well as completely random stacking of the MoS_2 layers were required for the simulation to correspond to what was observed experimentally. This is in agreement with TEM results. TEM images suggest a larger in-plane size for the Q sample when compared with the C sample. The suitability of using the same in-plane size (10 x 10 nm) for both sets of simulations can perhaps be reconciled as follows: X-ray diffraction is sensitive to crystalline correlations, whereas TEM images are a physical representation of the electron density.

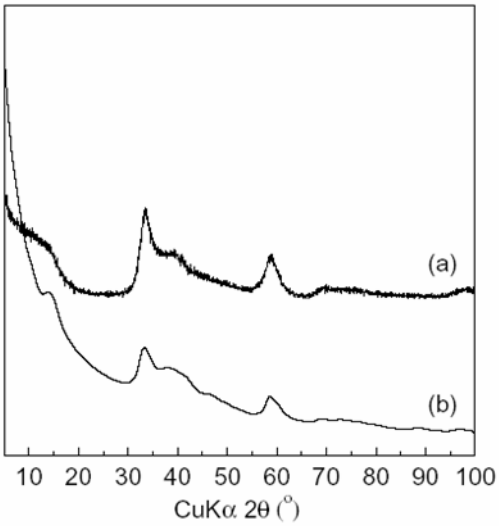

Figure 2-7. Powder X-ray diffraction patterns of (a) the product C and (b) DIFFaX simulation of 5 layers of MoS_2, each 10 x 10 nm in size stacked in a completely random manner.

It is possible that the (larger) sheets observed in the TEM image of the Q sample are defective, with small X-ray correlation lengths. We note that the sharp rise in the low-angle regions of the experimental powder XRD patterns is not easily modeled by the DIFFaX simulation. In the experiment, it corresponds to scattering from a collection of small particles (as opposed to a perfect crystal which would not scatter at $2\theta = 0$). DIFFaX does not account for low-angle scattering that arises from a collection of particles. The consequences of the different nanostructurings manifest as rather different surface areas. The results of BET surface area measurements are summarized in Table 2-1. All samples display relatively high surface areas (> 50 m^2/g).

The values for the product from sealed quartz tube reactions are slightly higher (77.7 m^2/g) than previously reported (max. 64.4 m^2/g) for this method.[8] The solvothermal method

without surfactant does not increase the surface area, but introducing CTAB with the precursor significantly increases the BET specific surface areas (152.9 m^2/g). The median pore diameter determined by the Horvath-Kawazoe method is similar for all products being about 8 Å.

Table 2-1. Surface areas and median pore diameters obtained from N_2 adsorption measurements.

	Q	S	C[a]	
			(6:1)	(1:1)
Surface area (m^2/g)[b]	77.7	52.6	152.9	175.3
Median pore diameter (Å)[c]	8.1	8.2	7.7	7.5

[a] Two samples, prepared with different starting mass ratios of $(NH_4)_2Mo_3S_{13} \cdot xH_2O$ to CTAB were prepared for BET measurements as indicated (6:1 and 1:1), [b] determined using the BET method, [c] determined using the Horvath-Kawazoe method.

2.4 Conclusion

Here, we have presented a one-step, low-temperature method to obtain high surface area, nanostructured MoS_2, using solvothermal conditions. The presence of the surfactant CTAB was crucial to obtain the interesting string-like morphology of the product MoS_2 as well as high surface areas. The distinct nature of the product prepared in the presence of the surfactant has been confirmed by TEM, BET and TG analysis, and XRD in conjunction with DIFFaX simulations.

2.5 References

1. Divigalpitiya, W. M. R.; Frindt, R. F., et al. *Science* **1989,** 246, 369.
2. Iijima, S. *Nature* **1991,** 354, 56.
3. Ugarte, D. *Nature* **1992,** 359, 707.
4. Tenne, R.; Margulis, L., et al. *Nature* **1992,** 360, 444.
5. Feldman, Y., Wasserman, E., Srolovitz, D.J., Tenne, R. *Science* **1995,** 267, 222.
6. Rao, C. N. R.; Nath, M. *Dalt. Trans.* **2003**, 1.
7. Tenne, R. *Adv. Mater.* **1995,** 7, 965.
8. Leist, A.; Stauf, S., et al. *J. Mater. Chem.* **1998,** 8, 241.
9. Zelenski, C. M.; Dorhout, P. K. *J. Am. Chem. Soc.* **1998,** 120, 734.
10. Bezverkhyy, I.; Afanasiev, P., et al. *Chem. Mater.* **2003,** 15, 2119.
11. Li, W. J.; Shi, E. W., et al. *J. Cryst. Growth* **2003,** 250, 418.
12. Afanasiev, P.; Xia, G. F., et al. *Chem. Mater.* **1999,** 11, 3216.
13. Peng, Y. Y.; Meng, Z. Y., et al. *Chem. Lett.* **2001**, 772.
14. Iwata, Y., Sato, K., Yoneda, T., Miki, Y., Sugimoto, Y., Nishijima, A., Shimada, H. *Catal. Today* **1998,** 45, 353.

15. Li, M.; Schnablegger, H., et al. *Nature* **1999,** 402, 393.
16. Gautam, U. K.; Rajamathi, M., et al. *Chem. Commun.* **2001**, 629.
17. Rajamathi, M.; Seshadri, R. *Curr. Opin. Solid State Mater. Sci.* **2002,** 6, 337.
18. Thimmaiah, S.; Rajamathi, M., et al. *J. Mater. Chem.* **2001,** 11, 3215.
19. Treacy, M. M. J.; Deem, M. W. *DIFFaX*, v. 1.803; 1996.
20. Treacy, M. M. J.; Deem, M. W. **1996**.
21. Spahr, M. E., Bitterli, P., Nesper, R., Müller, M., Krumeich, F., Nissen, H. U. *Angew. Chem. Int. Ed.* **1998,** 37, 1263.
22. Bérar, J.-F.; Garnier, P. *NIST Special Publication* **1992,** 846, 212.
23. Warren, B. E. *Phys. Rev.* **1941**, 693.

3 Selective synthesis of hollow and filled fullerene-like (IF) WS_2 nanoparticles via metal-organic chemical vapor deposition (MOCVD)

3.1 Introduction

Most of the transition metal chalcogenides, MQ_2 (M = group 4 - 7 metal; Q = S, Se, Te), display a characteristic layered structure. MQ_2 slabs are formed by two layers of close-packed chalcogenide atoms sandwiching one metal layer between them. These slabs are stacked, with just van der Waals forces between the slabs. The metal coordination may vary depending on M; while Group 4, 5 and 7 metals prefer octahedral coordination geometry, a trigonal prismatic coordination is adopted by the group 6 metals Mo and W, which is directly related to the semiconducting properties of MoS_2 and WS_2.[1, 2] The steric shielding of the metal atoms by the chalcogenide layers combined with the semiconducting properties make MoS_2 and WS_2 so inert that (in contrast to the II-VI semiconductors or TiS_2) they resist oxidation even in moist air at temperatures close to 100°C[3] are therefore regarded as interesting materials in the fields of catalysis, electrocatalysis, electrochemical intercalation and solid lubrication.

As in other layered compounds such as graphite[4] or boron nitride[5] the instability of the weakly van der Waals bonded sheets against folding and the need to saturate dangling bonds at the layer edges lead to the formation of spherical or cylindrical particles in contrast to the flat crystalline polymorphs.[6] A characteristic feature of closed-shell MQ_2-derived structures is that they are only metastable phases at room temperature because high preparation temperatures (> 800°C) are needed in order to interconnect the edges of single MQ_2 layers through the formation of rhomboidal and triangular point defects which provide curvature to the otherwise flat 2D MQ_2 slabs. Tenne and co-workers were the first to show that fullerene-type nanoparticles or nanopolyhedra and nanotubes represent an integral part of the phase diagram of MoS_2 and WS_2.[7] In the following decade a variety of methods including arc discharge,[8, 9] sulfurization/selenization of metal oxides,[10-20] chlorides[21, 22] or carbonyls,[23] decomposition of ammonium thiometallates,[24-27] chemical vapor transport,[28, 29] laser ablation,[30-33] microwave-induced plasma,[34, 35] atmospheric pressure chemical vapor deposition (APCVD),[22, 36] metal-organic chemical vapor deposition (MOCVD),[37] and spray pyrolysis[38] were utilized for the synthesis of inorganic fullerene (IF)- or nanotube-like (NT) structures of MQ_2 materials.

These nanostructures are not only interesting as model systems to overcome the gap between the chemistry at the atomic/molecular level and that of bulk compounds or as playground for research on quantum confinement effects[39] but also for diverse applications in engineering (*e.g.* as lubricants[40-46] with anti-wear effect,[47] as highly shock wave resistant materials,[48, 49] in energy industry, *e.g.* photovoltaic films,[50] material for H_2 storage,[51, 52] electrode material in lithium batteries,[52-54] or for catalysis[10, 55-58]).

A particular problem in the synthesis of WS_2 fullerene-type nanoparticles and nanotubes is that they are high-temperature and low-pressure phases in the W-S diagram which are not accessible by traditional solid state synthesis. In conventional high-temperature reactions the energy required for the solid state diffusion of the reactants would exceed the nucleation energy of the metastable WS_2 nanoparticles. A consequence of these bulk reactions is that only the most thermodynamically stable final products, *i.e.* 2H-WS_2 in the present case, can be produced. In contrast, reactions in which solid state diffusion plays only a minor role are kinetically controlled, and a phase may nucleate and grow until its growth exhausts the supply of the reactants. The sequence of phases formed depends upon the relative activation energies for nucleation of the various compounds, and compounds in the equilibrium phase diagram may be temporarily skipped if they have a large activation energy for nucleation. In fact, all synthetic approaches to chalcogenide nanoparticles mentioned above rely on the minimization of solid state diffusion.

Our approach to suppress solid state diffusion as a reaction parameter is based on a gas phase MOCVD reaction. In a recent communication we have described the gas-phase synthesis of MoS_2 and $MoSe_2$ hollow IF particles by using a two-step MOCVD based reaction.[37] In the first synthetic step chalcogenide nanoparticles are formed in a gas phase reaction between Mo, produced by thermal decomposition of $Mo(CO)_6$, and sulfur or selenium, respectively. One might speculate that in a subsequent growth step the lamellar sheet fragments continue to grow and begin to loosen at their ends until they roll up into onion-type structures. The particular advantages of this method are that (i) the generalized procedure might be extended to other members of the MQ_2 group, provided that volatile precursors are available, (ii) the synthesis of solid solutions $M_{1-x}M'_xQ_2$ or $MQ_{1-x}Q'_x$ or even ternary phases may be envisioned, and (iii) the reaction can be stopped at any time in order to perform a time-dependent structural investigation of the reaction products. (iv) The procedure may be upscaled for the synthesis of large quantities by parallelization with the aid of microreactors, (v) the use of the highly toxic reactants H_2S and H_2Se is avoided, (vi) a facile and fast synthesis of selenides (and even tellurides) without the thermally labile H_2Se (H_2Te)

is possible in quantitative yields, and (vii) with sophisticated techniques *in situ* studies could be done.

Important questions emerging from this study were (i) how the product structure and particle size distribution are affected by the process parameters such as gas flow and reaction time and (ii) whether the two-step procedure, *i.e.* the formation of precursor nanoparticles by MOCVD and the subsequent formation of fullerene-type particles in a separate annealing step, might be simplified to a one-step procedure thereby decreasing time and loss of material due to additional transfers, and (iii) whether the reaction may be transferred in a 1:1 fashion to WS_2 particles considering the differences in the Mo-S and W-S phase diagrams.[59] We report here, a large-scale one-step synthesis of inorganic fullerene-type WS_2 nanoparticles by a MOCVD approach starting from tungsten hexacarbonyl and sulfur.

3.2 Experimental

In a first set of experiments hollow IF-WS_2 particles were synthesized using conditions similar to those employed for the synthesis of IF-MoS_2. Firstly, an MOCVD synthesis (*e.g.* at 450°C, reaction time 2h) was carried out and the resulting material – collected from the inner walls of the small glass cylinder – was subjected to annealing (*e.g.* at 800°C for 1h under Ar) in a conventional tube furnace. Different synthesis temperatures (T_{ind}), annealing temperatures (T_{anneal}) and times (t_{anneal}) were studied as summarized in Table 3-1.

Table 3-1. Summary of reaction parameters (T_{ind}, T_{anneal} and t_{anneal}) of the two-step synthesis.

1. MOCVD		2. Annealing		
T [°C]	Name	*T* [°C]	*t* [h]	Name
450	WS_2 (450)	800	1	WS_2 (450/800-1)
450	WS_2 (450)	800	12	WS_2 (450/800-12)
550	WS_2 (550)	800	1	WS_2 (550/800-1)
650	WS_2 (650)	500	0.5	WS_2 (650/500-0.5)
650	WS_2 (650)	500	12	WS_2 (650/500-12)
650	WS_2 (650)	800	1	WS_2 (650/800-1)
650	WS_2 (650)	800	12	WS_2 (650/800-12)
650	WS_2 (650)	800	18	WS_2 (650/800-18)
750	WS_2 (750)	800	1	WS_2 (750/800-1)

Previous results for an APCVD synthesis,[36] where hollow IF-MS_2 (M=Mo, W) particles were synthesized by the reaction of metal chlorides with sulfur in a tube furnace at 850°C as well as our own experiments in the Mo/S system showed that the reaction temperature was the most important parameter for the formation of closed nested structures. In order to test whether the two-step reaction could be simplified to a single-step procedure, a series of experiments was carried out in which the reaction temperatures were varied between 450°C and 750°C in steps of 100°C.

3.2.1 Synthesis

Figure 3-1 shows the schematic representation of the experimental setup for the synthesis of filled fullerene-like WS_2 nanostructures and nanocrystallites. A more detailed description is given in Etzkorn et al.[37] While the precursors $W(CO)_6$ and S were heated at 150°C and 250°C, respectively, for all experiments, the temperature of the hot zone was varied from 450°C to 750°C in steps of 100°C for different experiments. A constant reaction time of 2 h was used for the MOCVD step of all experiments. For a comparison of the morphologies of WS_2 described here with MoS_2/$MoSe_2$ obtained by Etzkorn et al.[37] samples synthesized by a single-step process were annealed under Ar at 500 and 800°C for durations between 0.5 to 18h. Relevant reaction parameters of the two-step process (T_{ind}, T_{anneal} and t_{anneal}) are also summarized in Table 3-1.

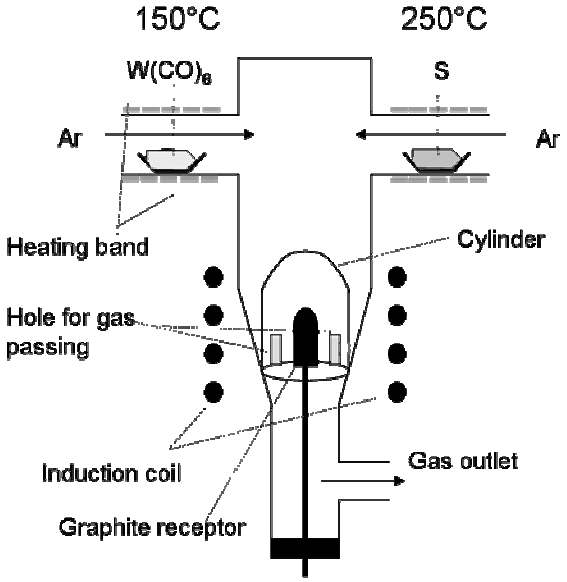

Figure 3-1. Schematic representation of the MOCVD experimental setup.

In a typical MOCVD run 1.83 mmol (0.645 g) of $W(CO)_6$[iii] (Aldrich, 99%) and 7.99 mmol (0.256 g) (4.32 mmol excess) of S (Alfa Aesar, 99.5%+, -100 mesh, sublimed) were weighed in and inserted into the setup under constant Ar flow. Prior to the synthesis the setup was flushed with Ar for at least 30 min. Subsequently, the graphite receptor was heated to the desired reaction temperatures (temperature at the induction coil (T_{ind}) = 450, 550, 650, and 750°C, respectively) by induction. Once the graphite receptor had reached the appropriate reaction temperature the precursors were heated. The heating rates were chosen in such a way that both reactants reach their final temperature in about the same time in order to provide a homogeneous reaction mixture for the whole duration of the experiment. The possibility of fast heating/cooling of the reaction zone makes this induction heated setup advantageous as compared to a slow tube furnace because "quenching" of the reaction is possible at any time. This allowed us to monitor the structure of the reaction products as a function of the reaction time by taking samples after given time intervals.

3.3 Characterization

3.3.1 Electron microscopy

The products were characterized using high resolution scanning electron microscopy (HRSEM) (LEO 1530 Field emission SEM, 6 kV extraction voltage) and transmission electron microscopy (TEM) carried out on a Philips EM420 instrument with a twin lens and a Philips CM12 with a twin lens at an acceleration voltage of 120 kV. High resolution images were taken with a Philips FEI TECNAI F30 ST electron microscope (field-emission gun, 300 kV extraction voltage) equipped with an Oxford EDAX (energy-dispersive X-ray) spectrometer with a Si/Li detector and an ultrathin window for elemental analysis. Samples for TEM measurements were prepared from ethanolic suspensions of the samples. Three drops of the ultrasonicated suspension were administered on a Cu grid coated with FORMVAR polymer and an amorphous carbon layer.

3.3.2 X-ray powder diffraction

X-ray diffraction patterns (XRD) were recorded using a Bruker AXS D8 Discover powder microdiffractometer (Cu $K_{\alpha 1}$ radiation, graphite monochromator) equipped with a 2D HiStar detector. Profiles were fitted with TOPAS 3.0P[60] using SPVII profile functions, in order to elucidate crystallinity and crystal size. Phase analyses were performed by means of

[iii] $W(CO)_6$ is toxic. It is hazardous because of the release of poisonous carbon monoxide. CO forms explosive mixtures with air. (Explosion limits: 12.5-74%, autoignition temperature 620°C). Therefore, oxygen-free atmosphere has to be assured throughout the experiment.

Rietveld refinements based on the fundamental parameter approach and the structure models given in reference[61] using TOPAS Academic.[62]

3.4 Results and discussion

In the sequel, the results of the two-step- and the single-step process will be discussed in two subsequent sections. For the two-step process various experimental conditions were used (see Table 3-1), but the discussion is restricted to the pristine WS_2 (650) and the annealed WS_2 (650-800/12) samples in the first section. In the second section the results of the single-step process will be reviewed. For the single-step process, the discussion will focus only on the reaction temperature. Variations of Ar flow and reaction time turned out to play only a minor role.

3.4.1 Hollow IF-WS_2 particles by a two-step synthesis

The synthesis of WS_2 via MOCVD at T_{ind} = 650°C for 2h resulted in a black deposit at the inside of the inner glass cylinder that could easily be removed with a spatula. The yield was in the mg range. This comparably large amount of material and the specially equipped microdiffractometer allowed us to employ X-ray diffractometry to obtain information about the bulk composition and structure of the samples before (Figure 3-2(a)) and after (Figure 3-2(b)) annealing.

3.4.1.1 Characterization of the products by X-ray powder diffraction

Both patterns can be attributed to WS_2. The diffraction patterns of the 2H- and 3R-polymorph are similar in the 2θ–range from 10-30°. A distinction between these two polymorphs is mainly possible regarding the splitting of the 2H-(103)- and (105)-reflection at ~ 40° and 50° (2θ).

For the non-annealed MOCVD product it is difficult to decide whether the 3R-polymorph is present in addition to 2H-WS_2 due to extensive peak broadening. The (002)/(003)-reflection[iv] at about 2θ = 14.2° corresponds to the stacking of WS_2-layers. This is in agreement with the value for either 2H- or 3R-WS_2 (d_{calc} = 0.616 nm; JCPDS card no. 8-237 and 35-651, respectively). The broad (002)-reflection indicates a large variation in the interlayer distances and only minor crystallinity. The center of the reflection corresponds to an interlayer spacing of d_{exp} = 0.627 nm which is somewhat larger than the value reported for the bulk material. The increased *d*-spacing can be attributed to lattice expansion due to

[iv] For the sake of clarity only (002) will be used to design the 2H-(002)/3R-(003)-reflection hereafter.

curvature[37] and/or defects[63] (note, this work was done on thin films) as reported in literature. The amount of 1.8% lattice expansion corresponds well with the value of 2% for IF-WS_2 obtained by Feldman.[12]

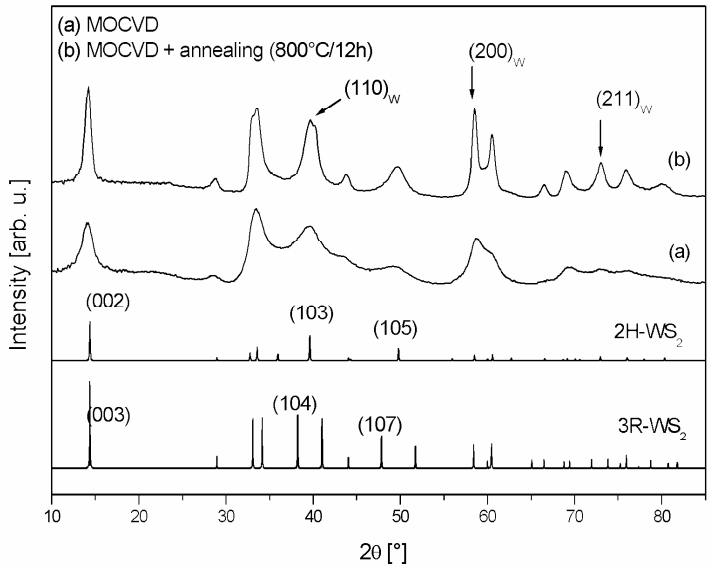

Figure 3-2. XRD patterns of a sample synthesized at 650°C before (a) and after (b) annealing at 800°C for 12 h. The arrows indicate the (110)-, (200)- and (211)-reflection of α-W, respectively. Simulated diffraction patterns of 2H- and 3R-WS_2 are given for comparison.

Table 3-2 summarizes important parameters (d_{002}, lattice expansion, FWHM) concerning the (002)/(003)-reflection for pristine and annealed samples.

The extent of peak broadening is reduced for the annealed sample which may be attributed to a crystallization process during annealing where the thermodynamically favored 2H-polymorph is formed. At around 39 and 50° (2θ), respectively, the (103)- and the (105)-reflection of the 2H-WS_2 polymorph are clearly observed. Rietveld refinements indicate the presence of the 3R-polymorph in addition to the main phase 2H-WS_2. Furthermore, reflections due to unreacted W are observed at ~ 40°, at 58° and at 73.4° (2θ) (HT-phase, stable > 373 K, JCPDF card no. 4-806).

Table 3-2. Summary of d_{002}-values obtained from XRD and TEM studies of the WS_2 (650) and WS_2 (650/800-12) sample. The corresponding lattice expansion (in percent) and the ratio of the left to right half of the FWHM are given in parentheses below the d- and FWHM-values, respectively.

	XRD		TEM	
	d_{002} [nm]	FWHM [°] 2θ	d_{002} (S/N) [nm]	d_{002} (R/O) [nm]
WS_2 (650)	0.627 (1.8)	1.5 (1.1)	0.636 (3.2)	0.654 (6.2)
WS_2 (650/800-12)	0.622 (1.0)	0.7 (1.3)	0.672 (3.1)	0.635 (9.1)

S, R, N and O correspond to the particle types small irregular (S) and round (R) for the non-annealed sample, and needle-like particles (N) and onions (O) for the annealed sample, respectively (Figure 3-4).

The d_{002}-value of WS_2 (650/800-12) is shifted to 0.622 nm (= 1% lattice expansion) which is still larger than the value reported for the bulk material but smaller than the one for the sample before annealing. This reduction of the d_{002}-value for annealed samples can be observed for all samples regardless of their original synthesis temperature T_{ind}. The effect is more pronounced (reduction to a lattice expansion of 0.3%, *i.e.* the theoretical value is nearly reached) for longer annealing times (18h, see Figure 3-3).

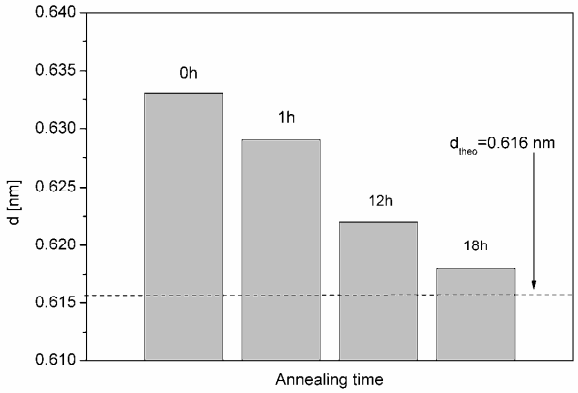

Figure 3-3. Development of d_{002}-values obtained from XRD as a function of annealing time for a WS_2 (650) sample.

3.4.1.2 Characterization of the products by HRSEM

High resolution scanning electron microscopy (HRSEM) revealed agglomerates of spherical particles with about 30 nm in diameter. The resolution of the instrument is not high enough to clarify whether or not these particles consist of even smaller particles as indicated by transmission electron microscopy studies. In addition to these spherical particles, the annealed sample exhibits a minor portion (10-20%) of needle-like particles of 10-20 nm in diameter and 50 to more than 100 nm in length (see appendix-ad chapter 3).

3.4.1.3 Characterization of the products by (HR)TEM

Figure 3-4 displays (HR)TEM images of samples synthesized at 650°C before (a) and after (b) annealing. All samples consist of network-like agglomerates of small particles. Samples without further thermal treatment exhibit two types of particles: Small irregular-shaped particles (S) with visible WS_2 layers and a significant amount of bigger (> 50 nm) round particles (R) with lattice fringes at the outer edges.

The values for the *d*-spacings range from 0.62 to 0.66 nm (corresponding to a lattice expansion of 0.6 to 7.1%), confirming the large variation of interlayer distances already observed by XRD .

As can be seen in Figure 3-4(b) the annealed sample consists of two types of particles: nanorods (N) and hollow nested onion-like (O) particles in about equal quantities.

The nanorods are about 10-15 nm in diameter with an aspect ratio ranging from 1.9 to 6.0. As can be seen in the high resolution TEM image (Figure 3-4(b)) they consist of highly crystalline, well-stacked layers with an average interlayer-distance of d = 0.64 nm (3.9% lattice expansion). This value is only slightly larger than the one obtained by XRD (d = 0.622 nm, ~ 1% lattice expansion). If defects occur (in form of edge dislocations) they tend to be close to the tips of the nanorods. All rods grow perpendicular to *c*, *e.g.* the stacking direction of the WS_2 slabs.

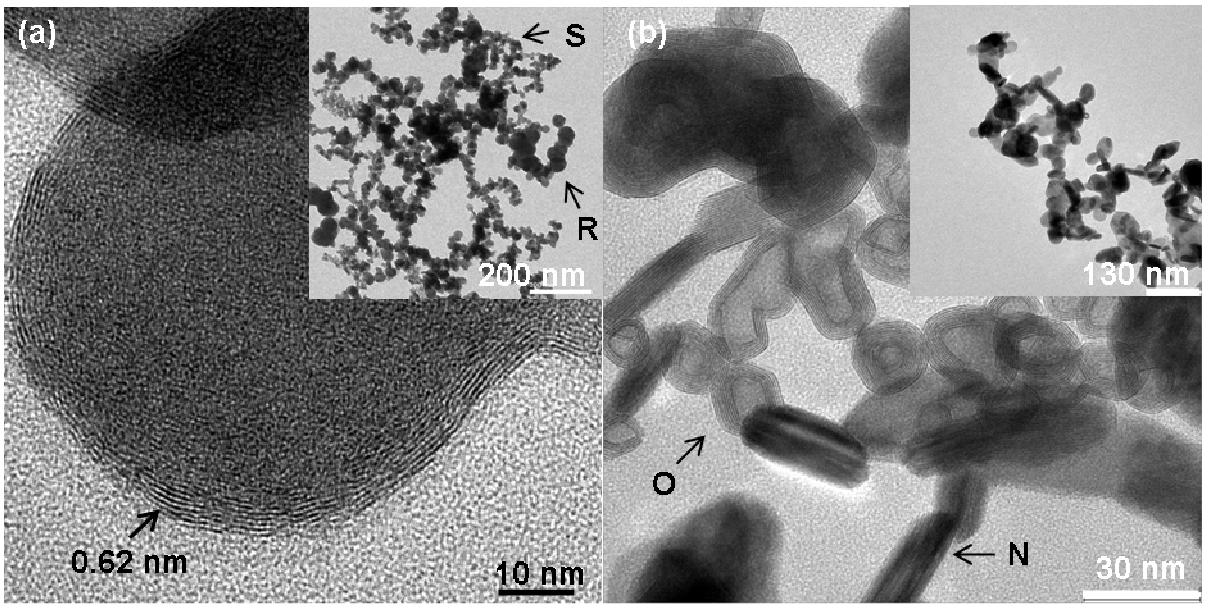

Figure 3-4. HRTEM images of a sample synthesized at 650°C before (a) and after (b) annealing for 12 h at 800°C. A corresponding overview TEM image is given in the inset.

The onion-like structures vary from 15 to 100 nm in size. Onion-like structures of 15-30 nm are mainly spherical consisting of 3-10 „shells“ of WS_2 layers around a hollow core. Bigger onion-like structures with diameters between 30 and 100 nm are mostly elongated or consist of “onions in an onion-structure” that can have 20 and more shells in total. The concave structures are obtained either by bending of the layers or by polyhedral joints of layer fragments with angles < 180° (often ~ 130-145°) resulting in the formation of faceted structures. The average d_{002}-spacing of 0.67 nm corresponds to a lattice expansion of 9%, a value significantly higher than d_{002} obtained by XRD. As the annealed samples exhibit well-ordered and well-stacked layers in comparison to the non-annealed samples, this lattice expansion has to be attributed to curvature (especially of the small diameter onions) and not to defects.

The decrease in lattice expansion for the annealed sample compared to the pristine material can be explained either by the healing of defects that were one reason for increased *d*-spacings. Secondly, the (002)-reflection near the ideal bulk value contains contributions from (i) needle-like nanocrystals with straight layers and a relatively small d_{002}-value and (ii) those parts of the onion-like structures which are built up from straight-layered fragments in a faceted manner. Because the XRD pattern is the superposition of contributions from all particles, that part of the sample with highly-ordered, straight-layered particles will induce a reduced overall d_{002}-value. On the other hand, the effect by the formation of onion-like structures (with curved layers) is superimposed and should lead to a lattice expansion as well as to strain (confirmed by an increase of the peak asymmetry, see FWHM ratio in Table 3-2). Because the fullerene-like structures are hollow, very small radii do not occur. Therefore, less lattice expansion is necessary (as for filled structures described in the second part). In summary, the healing of defects and the formation of straight layered particles is outweighing the effect of curvature on the development of the d_{002}-value.

In order to shed light on the question whether the faceted or the bent structures are the thermodynamically favored forms of WS_2, reactions were carried out with longer annealing times at 800°C. After 18 h of annealing, both particle types are still present with none of it prevailing. Bending or faceting seems to be more dependent on the radius of the particle as already observed in NbS_2 onion-like particles.[22] At the inner parts faceted growth is more often observed whereas the outer layers tend to be bent.

In summary, hollow IF-WS_2 particles could be obtained from a two-step synthesis using conditions similar to those reported for the synthesis of MoS_2 or $MoSe_2$. A slight drawback was the contamination of the final product with a considerable amount of needle-like particles. *In situ* heating HRTEM studies indicate that the ratio of onion-like structures to needles is dependent on the morphology of the product before heating (see the following section) and not on the annealing conditions.

3.4.2 Single-step process – influence of the reaction temperature in the induction-heated zone

The MOCVD synthesis of WS_2 from $W(CO)_6$ and S was carried out at four different temperatures of the induction heated zone (T_{ind} = 450, 550, 650, 750°C) in order to investigate the role of temperature for the formation of closed-shell structures in a single step. Deposition of a black product started on the cold parts at the inside of the inner cylinder, *i.e.* above the heating zone of the induction furnace, about 10 minutes after the final reaction temperature

was reached. For T_{ind} > 650°C a metallic product was observed at the outside of the inner cylinder as well as in the lower inner part. The yield of WS_2 nanoparticles increased with increasing reaction temperature T_{ind}.

3.4.2.1 Characterization of the products by X-ray powder diffraction

X-ray diffractometry was used to determine the overall composition and structure of the products. X-ray diffraction patterns of all samples (see Figure 3-5) indicate the presence of tungsten disulfide (JCPDF card no. 8-237 and 35-651, respectively) independent of the choice of reaction parameters.

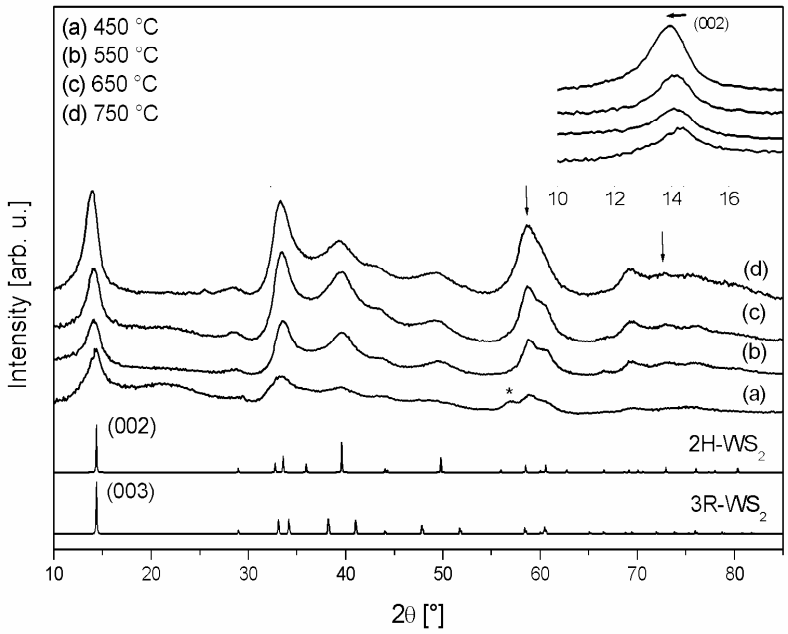

Figure 3-5. XRD traces of samples synthesized at 450°C (a), 550°C (b), 650°C (c) and 750°C (d) and the calculated diffraction patterns of 2H- and 3R-WS_2, respectively. A magnification of the (002)-reflection is displayed in the inset. The arrows mark the (200)- and (211)-reflection, respectively, of α-W (JCPDS card no. 4-806). One unidentified reflection is indicated with an asterisk (*).

Due to peak broadening a clear distinction whether the 3R modification of WS_2 is present in addition to the 2H-phase is difficult. The results of Rietveld refinements indicate that the 3R-variant predominates (~ 60-80%) while the 2H-variant is the minority component (see appendix – ad chapter 3). A tungsten impurity can be identified by its (200)- and (211)-reflection (indicated by arrows in Figure 3-5) for samples synthesized at $T_{ind} \geq 550$°C. As the synthesis temperature T_{ind} is increased from 450 to 750°C several tendencies can be noted:

(i) an increase in intensity especially for the (002)-reflection,

(ii) a decrease in its peak broadness (see inset Figure 3-5 and FWHM values in Table 3-3),

(iii)a linear increase in the d_{002}-values (*e.g.* decrease in 2θ-values, see inset Figure 3-5) and their variance as displayed in Figure 3-6,

(iv)a decrease in peak asymmetry up to $T_{ind} \leq 650°C$ and an increase for T_{ind} = 750°C (see ratio of left and right contribution to FWHM in Table 3-3).

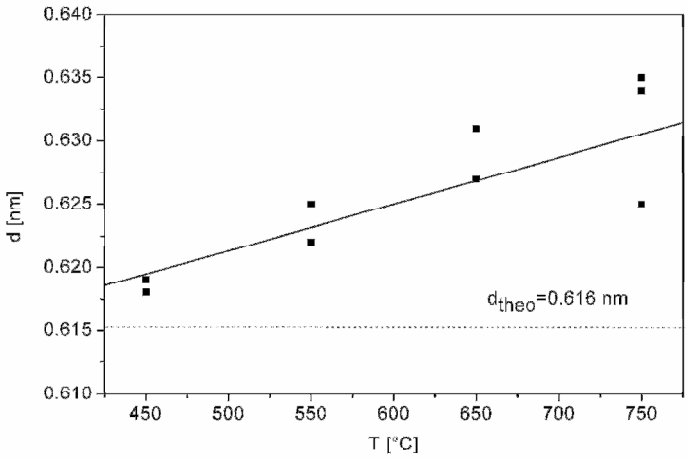

Figure 3-6. Lattice expansion monitored by means of the d_{002}-values of samples synthesized at 450, 550, 650 and 750°C. A linear fit is displayed as black line.

The (002)-reflection is indicative of the stacking of the WS_2 layers. Its presence even in the 450°C samples shows that a reaction between $W(CO)_6$ and S has taken place resulting in the formation of small regions of stacked WS_2 layers. For higher reaction temperatures the order and the crystallinity of the products improves continuously. This is reflected in the increasing intensity, sharpness and symmetry of the (002)-reflection shown in the inset of Figure 3-5. Another indicator are the decreasing FWHM-values and the ratio of left and right contributions of the FWHM compiled in Table 3-3. Note that the asymmetry increases again for samples prepared at 750°C. An explanation for this observation will be provided during the discussion of the TEM results (*vide infra*).

Table 3-3. Summary of (002)-peak shape parameters: Given are the values for samples synthesized at 450, 550, 650 and 750°C, respectively.

T		FWHM [°]			d	
[°C]	2θ [°]	Left	Right	Sum	[nm]	Lat. exp.[a]
450	14.3068	1.1711	0.8518	2.0229	6.19	0.4%
550	14.1579	0.9970	0.7534	1.7504	6.25	1.5%
650	14.1124	0.7952	0.7149	1.5101	6.27	1.8%
750	13.9647	0.8639	0.6555	1.5194	6.34	2.9%

[a] Lattice expansion in relation to the bulk d_{002}.

All d_{002}-values (see Table 3-3), *i.e.* the stacking distances of the WS_2 layers, are significantly enlarged as compared to the bulk material. This has also been observed for other IF-structures (such as MoS_2 synthesized in a fluidized bed reactor[64]) and can be attributed to a

lattice expansion due to curvature of the sheets or defects. The increase in lattice expansion for samples synthesized at higher temperatures is due to an increased amount of curved structures with decreasing radius. A detailed discussion will be given in the following TEM section.

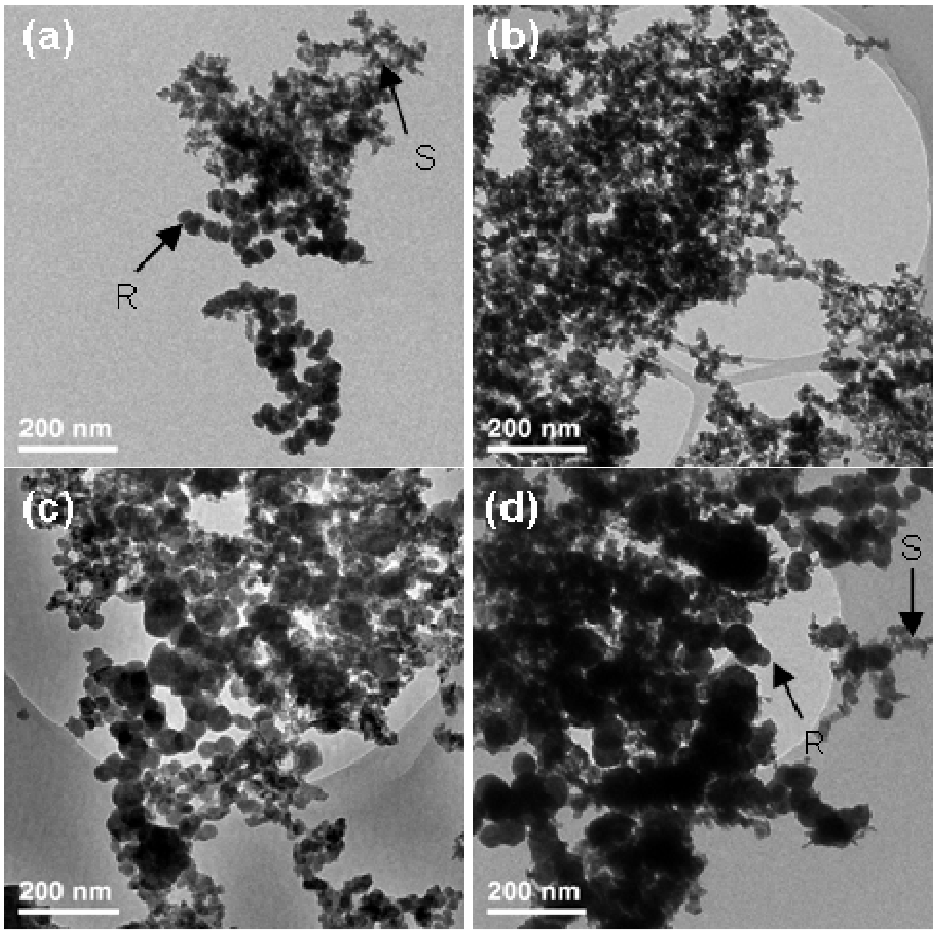

Figure 3-7. TEM images of samples synthesized at 450 (a), 550 (b), 650 (c) and 750°C (d). The arrows in (a) and (d) highlight irregular-shaped, small (S-type) particles and bigger, round (R-type) particles.

3.4.2.2 Characterization of the products by HRTEM

Figure 3-7 shows representative TEM micrographs of samples synthesized at 450 (a), 550 (b), 650 (c) and 750°C (d). All samples consist of network-like agglomerates of small particles with diameters ranging from about 10 to 150 nm. Two sorts of particles can be distinguished according to their diameters and shapes. The fraction of particles with the smallest diameters (~ 10 nm) (referred to as S-type particles in the sequel) contains irregular shaped but rather round particles, which are often interconnected in a manner observed for melted metals. In contrast to the S-type particles obtained in the case of MoS_2 and $MoSe_2$,[37] these layers are straight and not curved. This increased stability of the WS_2 layers may be the result of stronger van der Waals interactions between the slabs due to the higher polarizibility of S by Mo compared to W. This observation would also be consistent with the lower

reactivity of WS_2 in intercalation reactions.[37] The second fraction of particles that are mainly round (R-type) exhibits mean diameters between 25 and 200 nm, although high resolution images show faceting due to non-connected layer "packages".

3.4.2.2.1 Samples prepared at 450°C

In samples synthesized at 450°C the S-type particles are predominant, with a small portion of R-type particles. A high resolution (HRTEM) image of the S-type particle agglomerate is provided in Figure 3-8(a). It confirms the small coherence length that has been proposed from the XRD measurements due to (i) the presence of partly amorphous material and (ii) the small number of WS_2 layers (up to 7) and the small particle size (ca. 10 nm in length) of the crystalline parts. The *d*-spacing of 0.640 nm corresponds to a lattice expansion of 3.8%.

3.4.2.2.2 Samples prepared at 550°C

Figure 3-7(b) shows the TEM micrograph of a sample synthesized at 550°C. It contains S- and R-type particles as found for the reaction at 450°C, but the fraction of R-type particles has increased. In HRTEM studies more layered particles were detected compared to samples prepared at lower temperature (450°C).

The S-type particles (Figure 3-8(b)) are made up of 4-10 layers of about 10 nm in length. For some of them the length of the outer layers is smaller than that of the inner layers, which leads to a spherical appearance of the particles even though the individual layers are not bent. A decrease in the interlayer spacing to 0.633 nm (2.8% lat. exp.) can be observed. The R-type particles consist of fragments containing 4-6 curved layers in a stacked arrangement. These fragments are arranged around an amorphous core in a spherical fashion. They are not intergrown, and their overall appearance resembles that of an onion-type structure (Figure 3-8(f)).

The interlayer separation for these fragments is 0.651 nm (5.7% lattice expansion). We note that the interlayer distance varies not only between two different pairs of layers, but also for an individual pair, especially in curved layers, whereas in elongated particles the interlayer distance is mainly constant. This points to a larger number of defects (namely edge dislocations) and stacking faults for the curved structures. As a matter of fact, we observe a higher defect concentration for the curved structures in HRTEM studies. Thus, the relatively large lattice expansion reflected in a large d_{002}-value is not only due to curvature but also to the large number of defects present in these particles.

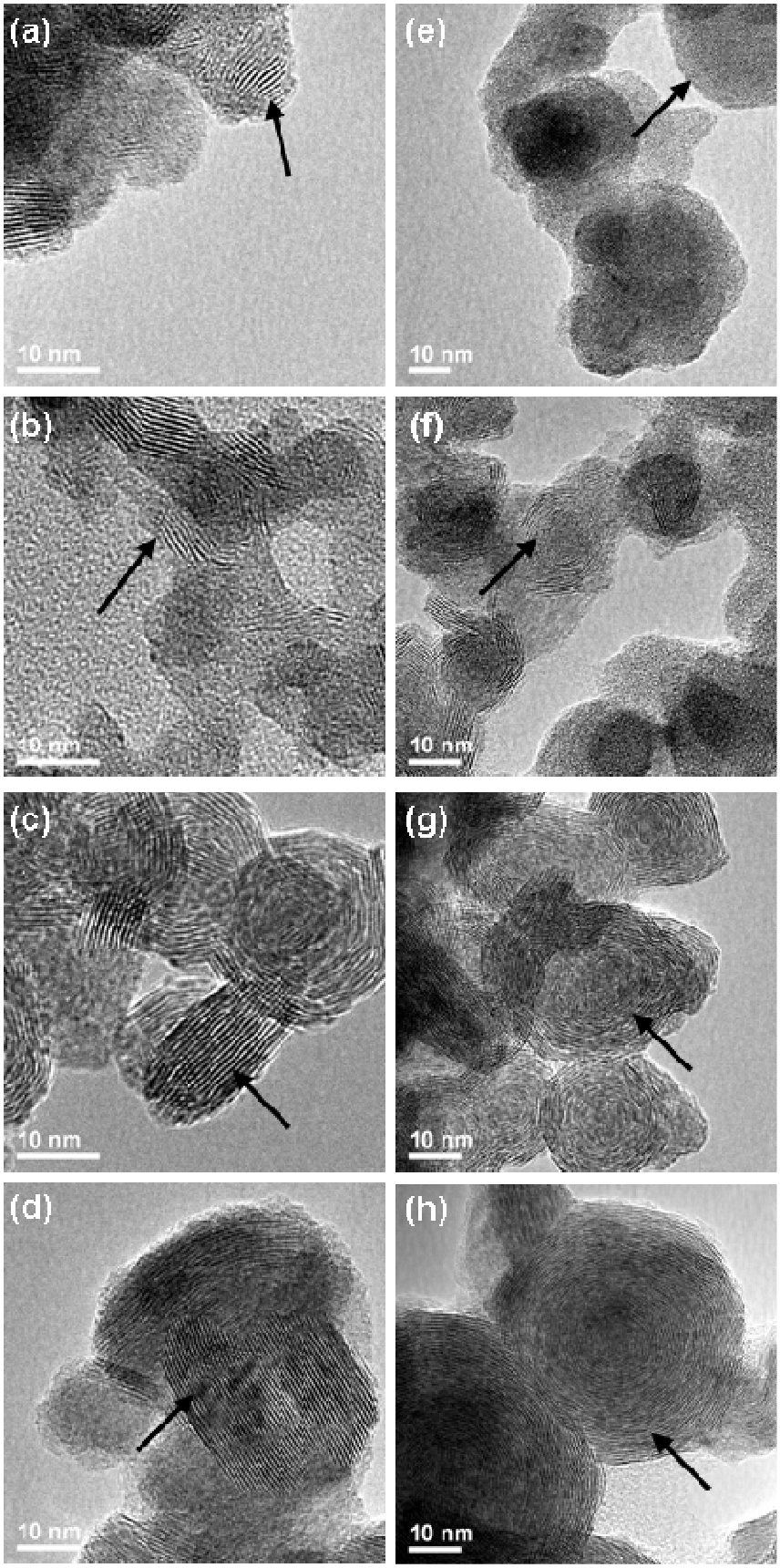

Figure 3-8. HRTEM images of S-type (a-d) and R-type (e-h) particles, respectively, in samples synthesized at 450 (a/e), 550 (b/f), 650 (c/g) and 750°C (d/h).

3.4.2.2.3 Samples prepared at 650°C

Increasing the reaction temperature leads to enhanced particle growth through the formation of larger sheets and a higher degree of agglomeration through a stacking of sheets. S-type particles (Fig. 8c) exhibit up to 18 layers with sheet diameters of approx. 20 nm and an average interlayer spacing of 0.636 nm (3.3% lattice expansion). The amount of S-type particles decreases with increasing temperature, while the number of R-type particles (Figure 3-8(g)) increases. In R-type particles the lateral growth of the layered fragments leads to particle intergrowth and therefore to the formation of closed structures with up to 10 layers with d_{002} = 0.654 nm corresponding to a lattice expansion of 6.2%. The large number of defects resulting from the temperature increase suggests that fullerene-type particles may be formed at higher temperatures, because a sufficiently strong curvature is induced through the formation of rhomboidal or triangular defects of the otherwise flat 2D MQ_2-sheets.

3.4.2.2.4 Samples prepared at 750°C

When the reaction temperature was raised to 750°C onion-shell-like structures were obtained. Their structure differs considerably from that of the particles obtained by the two-step method described above and the structure of the IF-MoS_2/$MoSe_2$ structures reported previously.[37] In the former case the onion shell contained only few, very well ordered layers (see Figure 3-9(a)) leaving a hollow core. In contrast, the single-step approach at T_{ind} = 750°C leads to the formation of onion shell-like structures with a large number (up to 25) of layers with a filled core. Filled core particles have already been synthesized by several groups, the core being a material equal[33] or different from MS_2,[17, 32, 65] *e.g.* from remaining oxide due to incomplete sulfurization of the precursor material.[66] Our filled onion-like particles still exhibit some edge dislocations, but significantly less than the particles synthesized at 650°C. The average *d*-spacing of 0.656 nm indicates a lattice expansion of about 6.5%.

In most of the onion-like particles no lattice fringes can be observed in the central part (~ 3 nm), but the contrast in low resolution TEM images is stronger than that of the center of the hollow particles found after annealing. This indicates that the particles are filled either with amorphous material or yet some sheets for which the higher thickness of the particles at the center of the particle prevents the detection of the lattice fringes of crystalline material. We also observe the formation of S-type particles (in small amounts). The number of layers (d_{002} = 0.640 nm = 3.8% lat. exp.) and concomitantly their size have increased, but rod-like structures as observed in annealed samples obtained from the two-step reaction are not formed. This implies a pronounced difference in the growth mechanism, and we will dwell on this point below.

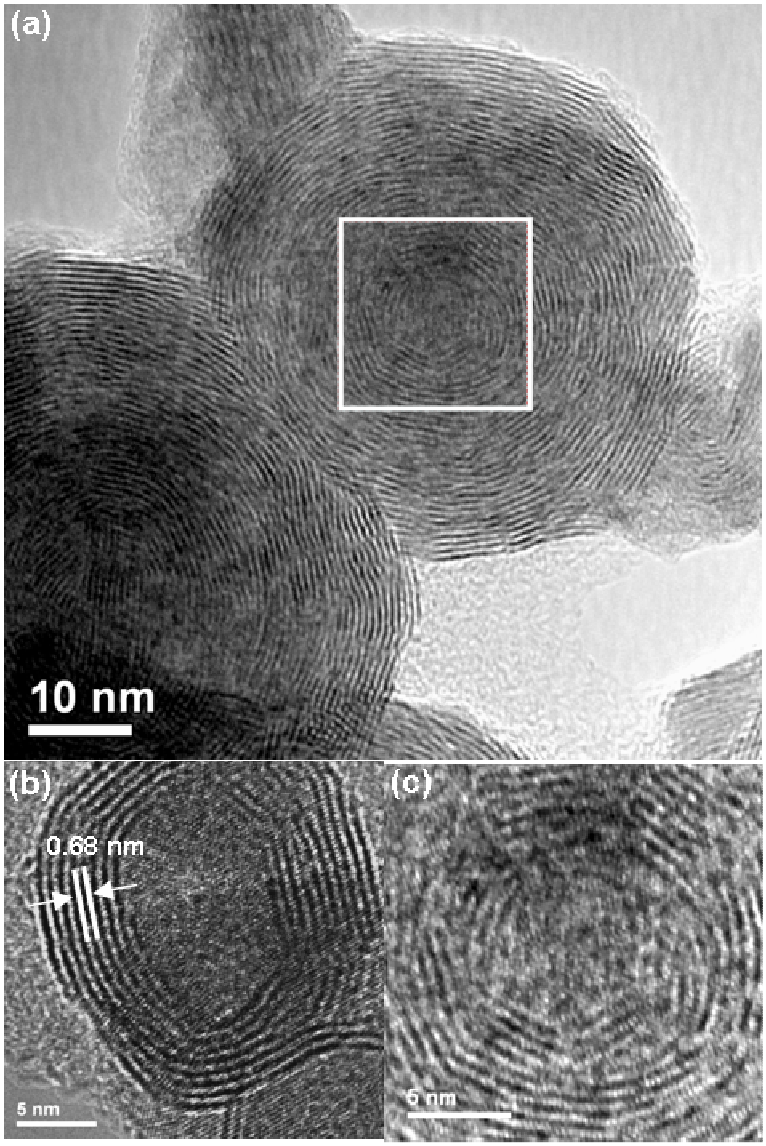

Figure 3-9. Filled (a) and hollow (b) onion-like structures, obtained from a WS_2 (750) and a WS_2 (650/800-12) sample, respectively. Background filtered IFFT of the central part (white square in (a)) of the filled IF-structure is given in (c). The corresponding FFT is given in the appendix (ad chapter 3).

To summarize, we can conclude that an increase in temperature leads to increased crystallinity as has been already proposed from the XRD results. It has to be noted that the *d*-values of the S-type particles do not exhibit a specific tendency whereas for the R-type particles an increase of the lattice expansion can be observed. Therefore, the shift to lower 2θ-values of the (002)-reflection, *i.e.* to higher d_{002}-values, found in XRD measurements can be attributed to the formation of these R-type particles. The increasing asymmetry of peak shape for the WS_2 (750) sample can be explained by the formation of nearly closed onion-like structures and therefore a higher amount of curvature and strain at this reaction temperature. The outward-in direction of the crystallization process leads to the formation of the innermost shells, *i.e.* the most bent ones, only at higher temperatures, therefore adding to the total

amount of strain. This finding would also explain the increase in the inner strain when the reaction temperature is raised to 750°C.

Figure 3-10 shows a representative EDX spectrum of a sample synthesized at 450°C. The overall W : S ratio is 1 : 2. The S-type particles are typically more tungsten rich than the R-type particles. Increasing the reaction temperature leads to a depletion in the sulfur content especially for the R-type particles, in harmony with thermodynamic predictions.

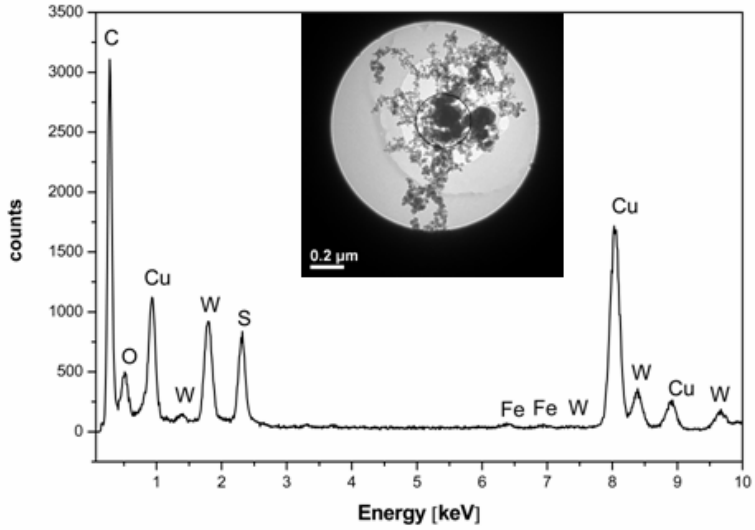

Figure 3-10. EDX spectrum of a 450°C sample. The analyzed area is marked in the corresponding TEM image in the inset. W(L) : S(K) ratio is determined as 1 : 2.

3.4.2.3 Characterization by scanning electron microscopy

Scanning electron microscopic studies confirm the network-like morphology of all samples regardless of the reaction temperature. Figure 3-12 displays an overview of a WS_2 (550) sample where the sponge-like structure is clearly visible. Samples obtained at different reaction temperatures look similar, except for the WS_2 (750) sample, which appears slightly denser.

High resolution SEM imaging (see inset of Figure 3-12) allows the distinction between round R-type and more irregular shaped S-type particles as already described before. We note that the S-type particles imaged by HRSEM must be regarded as an ensemble of the S-type particles described in the TEM section because the resolution of HRSEM is not high enough to clearly visualize the small crystallites. The resolution limit may also be the reason why a quantification of the R/S-type particle ratio is not possible from these measurements. From a qualitative point of view none of the two particle types is predominant and no distinctive change in their proportion can be observed. The average diameter of the R-type particles increases from 30 to 40 nm with increasing temperature.

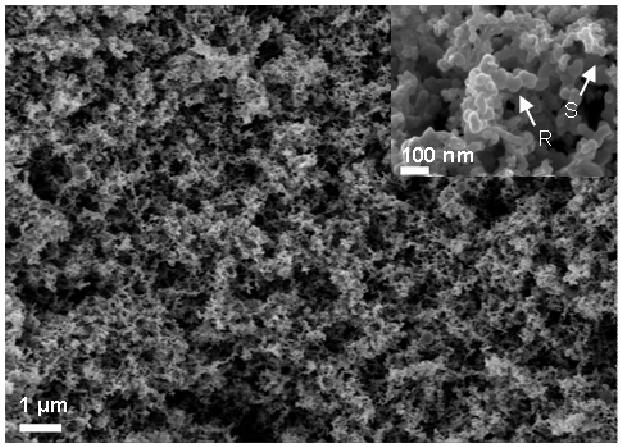

Figure 3-11. HRSEM image of a sample synthesized at 550°C. S- and R-type particles are marked with arrows.

3.4.3 Growth mechanism

TEM studies of the reaction products reveal the formation of two types of particles (S and R). The size of both types of particles increases and the crystallinity improves when the reaction temperature is raised from 450°C to 750°C. After introducing general aspects, a feasible growth mechanism of these particles depending on the synthesis temperature is discussed in the following section.

Conceptually, the formation of solid-state compounds can be broken down into two key steps: the interdiffusion of the reactants and the nucleation/crystallization of products. Since IF- and NT-type WS_2 represent binary non-equilibrium phases, our key goal must be to gain kinetic control of the reaction pathway by eliminating diffusion as a rate-limiting step. This leaves nucleation, a kinetic phenomenon dependent upon overcoming a reaction barrier, as the crucial step to control. A homogeneous, amorphous mixture of the components is an ideal reaction intermediate for the preparation of extended solids. The interdiffusion of the reactants is driven by the large negative heat of mixing and only the growth of this amorphous mixture would be diffusion-controlled. For particles with diameters of approx. 5-10 nm, diffusion is completed in the formation of this mixture. This leaves nucleation as the rate-limiting step in the formation of a crystalline solid. The nucleation barrier depends upon the free energy gain per unit volume, surface energy of the growing embryo, and the energy necessary to rearrange the amorphous mixture.[67] This last term is minimized for the polymorph closest to the composition of the amorphous mixture. If the rearrangement energy is large relative to the other terms, composition may control the formation of the polymorph that nucleates. When the amorphous particles shown in Figure 3-13 are heated, WS_2 starts to nucleate and grows until its growth exhausts one of the reactants within the particle volume or until the particle boundary is reached - only then another crystalline phase might nucleate at

the compound-element interface. The new compound grows until it exhausts either the supply of compound or element. This process repeats until the equilibrium mix of products is obtained. The sequence of phases formed on the way to this state depends upon the relative activation energies for nucleation of the respective compounds. The tungsten sulfur phase diagram suggests that WS_2 is the only binary phase to be formed.

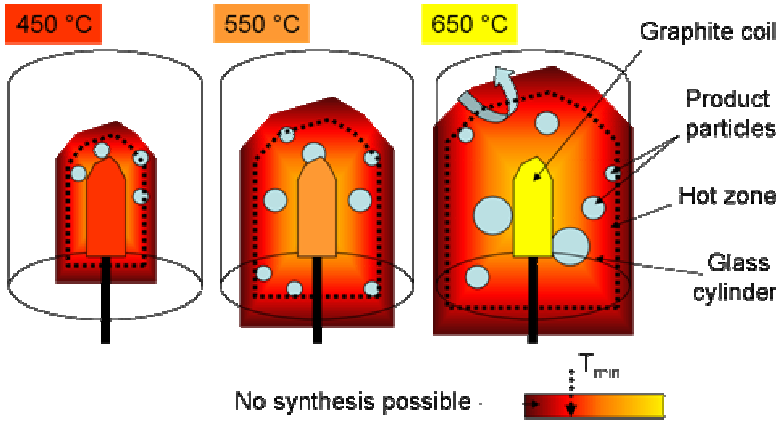

Figure 3-12. Schematic representation of the hot zone around the graphite coil. A dotted line represents the minimum temperature needed for particle growth.

If we assume that intraparticle growth is preferred over interparticle growth, an additional size restriction imposed by reducing the diameter of the particles containing the amorphous mixture may lead to the formation of discrete nested fullerenes or nanotubes provided that the energy required for the bending of the otherwise flat WS_2 sheets can be supplied before particle intergrowth takes place.

We reasoned that an amorphous mixture might be formed by reacting molecular precursors according to

(3-1) $$W(CO)_6 + 2S_g \xrightarrow{\Delta T} WS_2 + 6CO$$

In a first reaction step the precursors $W(CO)_6$ and S_8 are heated in a continuous Ar flow. At 250°C the sulfur precursor has passed its melting point and a constant vapor pressure has built up. Heating the precursor $W(CO)_6$ to 150°C results in its decomposition according to

(3-2) $$W(CO)_6 \xrightarrow{\Delta T} W + 6CO$$

The decomposition/evaporation products are transported with the Ar carrier gas flow to the central part of the reactor. In the upper part of the reactor the carrier gas streams containing W, CO and S_g mix intimately to form a homogeneous amorphous “alloy” that is a suitable reaction intermediate for the preparation of nanoparticles or extended solids of the binary phase. Nucleation of WS_2 is induced and controlled by temperature. It occurs in the hot

zone of the induction furnace around the graphite coil if $T > T_{min}$ (as W and S are highly dispersed T_{min} will be lower than for the bulk synthesis of WS_2 out of the elements).

The spatial dilation of this hot zone is small for low temperatures and increases upon increasing temperature (see Figure 3-12).

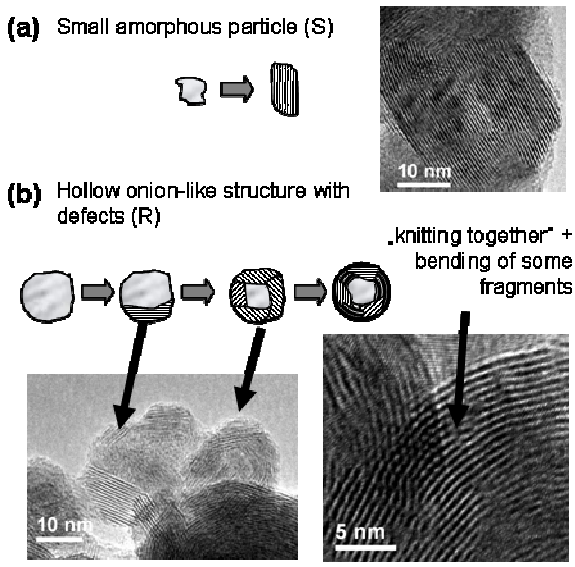

Figure 3-13. Formation of S (a) and R-type (b) particles: scheme and TEM images.

The key factor for the formation of particles with different sizes would be the difference in the retention times of the particles in the growth region, *i.e.* the region with $T > T_{min}$. S-Type particles seem to traverse only a short path through the growth region. These particles can be trapped by contact with the glass cylinder, which leads to their irregular shape. Particles experiencing a longer path through the growth region are more likely to form spherical intergrown aggregates as illustrated in Figure 3-13(b). The longer reaction time also enables these particles to adopt the energetically preferred spherical equilibrium morphologies. The higher the synthesis temperature the more extended the growth region and therefore the more different pathways and length exist resulting in a less controllable particle size and type distribution.

This growth model would explain (i) the formation of two different particle types, (ii) of the increasing amount R-type particles, (iii) their increasing size with increasing reaction temperatures and (iv) the increasing variance of the *d*-values (see Figure 3-6) for higher temperatures.

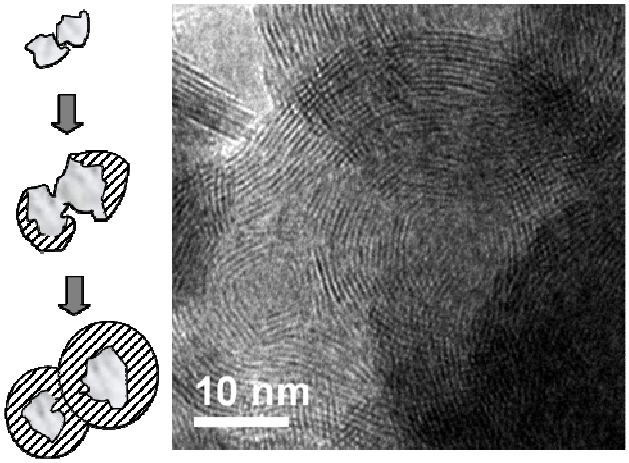

Figure 3-14. Formation of a binuclear particle (left: schematic representation, right: corresponding HRTEM image).

In HRTEM studies, we find incipient crystallization at T_{ind} = 450°C for the S-type particles, whereas the R-type particles are still amorphous. This suggests that for the partly amorphous small particles crystallization is favored, whereas for the larger round particles surface/defect minimization by particle intergrowth is dominant. At elevated reaction temperatures (T > 550°C) crystallization is also observed for R-type particles. It starts at the outer boundaries of the particles with the layers oriented tangential to the surface. Beyond a critical size, crystallization starts simultaneously at several sites of the surface. Several layered fragments start to intergrow by enclosing an amorphous core (see Figure 3-13(b)). As a result, we observe facetted particles based on interconnected fragments with numerous defects at the boundaries. The main portion of the fragments contains planar layers that are not yet bent. Only at higher reaction temperatures (> 650°C) a bending of these layers and an associated formation of defects is observed.

The outside-in growth in the interior of the layered fragments leads to an increase in the number of layers. In addition, multinuclear particles have been observed (see Figure 3-14). The present studies could not clarify whether the interconnection of these particles has been already established in the amorphous state or only after incipient crystallization.

3.5 Summary and conclusion

We have demonstrated a novel and simple synthetic approach to hollow and filled WS_2 fullerene-type nanoparticles which are difficult to obtain by other methods. In the first MOCVD step nanoparticles of the layered material are synthesized from gaseous precursors. In the second reaction step, an annealing under argon atmosphere, the resulting nanoparticles were allowed to grow until they convert to nano-sheets which then automatically roll up into

nested fullerene-type structures. This simple and inexpensive approach may be easily upscaled and allows the synthesis of nanostructured WS_2 in bulk quantities.

Elimination of the second annealing step by heating the reaction zone of the reactor to temperatures between 450°C and 750°C leads to two different types of particles, small irregular (S-type) and bigger spherical (R-type), for all experimental conditions. The crystallinity and the size of the particles (*i.e.* the number of layers per particle and the diameters of the individual WS_2 sheets) increase with increasing reaction temperature. EDX analyses revealed a W : S ratio of 1 : 2. For reaction temperatures > 650°C the incipient segregation of W nanoparticles was observed (in accordance with the W-S phase diagram). The optimum processing temperature for the synthesis of filled fullerene-like structures was 750°C.

A growth mechanism explaining the formation of two different types of particles in the one-step approach was proposed. We conclude that the MOCVD approach is an excellent method to synthesize inorganic fullerene-like nanoparticles which allows the selective synthesis of hollow or filled onion-type nanoparticles. It can be applied for a variety of different binary and even ternary layered compounds under environmentally friendly conditions with the prospect of easy upscaling, *e.g.* by using microreactor techniques. The investigation of the applicability of these IF-MQ_2 particles as lubricating materials is subject to ongoing studies.

3.6 References

1. Tremel, W.; Seshadri, R.; Finckh, E. W. *Chem. unserer Zeit* **2001,** 35, 42.
2. Tremel, W.; Finckh, E. W. *Chem. unserer Zeit* **2004,** 38, 326.
3. Ross, S.; Sussman, A. *J. Phys. Chem.* **1955,** 59, 889.
4. Kroto, H. W.; Heath, J. R.; O'Brien, S. C.; Curl, R. F.; Smalley, R. E. *Nature* **1985,** 318, 162.
5. Chopra, N. G.; Luyken, R. J.; Cherrey, K.; Crespi, V. H.; Cohen, M. L.; Louie, S. G.; Zettl, A. *Science* **1995,** 269, 966.
6. Tremel, W. *Angew. Chem., Int. Ed. Engl.* **1999,** 38, 2175.
7. Tenne, R.; Margulis, L.; Genut, M.; Hodes, G. *Nature* **1992,** 360, 444.
8. Alexandrou, I.; Sano, N.; Burrows, A.; Meyer, R. R.; Wang, H.; Kirkland, A. I.; Kiely, C. J.; Amaratunga, G. A. J. *Nanotechn.* **2003,** 14, 913.
9. Hu, J. J.; Bultman, J. E.; Zabinski, J. S. *Tribol. Lett.* **2004,** 17, 543.
10. Camacho-Bragado, G. A.; Elechiguerra, J. L.; Olivas, A.; Fuentes, S.; Galvan, D.; Yacaman, M. J. *J. Catal.* **2005,** 234, 182.

11. Chen, W. X.; Tu, J. P.; Ma, X. C.; Xu, Z. D.; Tenne, R.; Rosenstveig, R. *Chin. Chem. Lett.* **2003,** 14, 312.
12. Feldman, Y.; Frey, G. L.; Homyonfer, M.; Lyakhovitskaya, V.; Margulis, L.; Cohen, H.; Hodes, G.; Hutchison, J. L.; Tenne, R. *J. Am. Chem. Soc.* **1996,** 118, 5362.
13. Feldman, Y.; Margulis, L.; Homyonfer, M.; Tenne, R. *High. Temp. Mater. Proc.* **1996,** 15, 163.
14. Feldman, Y.; Zak, A.; Popovitz-Biro, R.; Tenne, R. *Solid State Sci.* **2000,** 2, 663.
15. Zak, A.; Feldman, Y.; Alperovich, V.; Rosentsveig, R.; Tenne, R. *J. Am. Chem. Soc.* **2000,** 122, 11108.
16. Li, X. L.; Li, Y. D. *Chem. Eur. J.* **2003,** 9, 2726.
17. Rothschild, A.; Tenne, R.; Sloan, J.; York, A. P. E.; Green, M. L. H.; Sloan, J.; Hutchison, J. L. *Chem. Commun.* **1999**, 363.
18. Tsirlina, T.; Feldman, Y.; Homyonfer, M.; Sloan, J.; Hutchison, J. L.; Tenne, R. *Full. Sci. Techn.* **1998,** 6, 157.
19. Whitby, R. L. D.; Hsu, W. K.; Lee, T. H.; Boothroyd, C. B.; Kroto, H. W.; Walton, D. R. M. *Chem. Phys. Lett.* **2002,** 359, 68.
20. Coleman, K. S., Sloan, J., Hanson, N. A., Brown, G., Clancy, G. P., Terrones, M., Terrones, H., Green, M. L. H. *J. Am. Chem. Soc.* **2002,** 124, 11580.
21. Margolin, A.; Popovitz-Biro, R.; Albu-Yaron, A.; Moshkovich, A.; Rapoport, L.; Tenne, R. *Current Nanoscience* **2005,** 1, 253.
22. Schuffenhauer, C.; Popovitz-Biro, R.; Tenne, R. *J. Mater. Chem.* **2002,** 12, 1587.
23. Lee, G. H.; Jeong, J. W.; Huh, S. H.; Kim, S. H.; Choi, B. J.; Kim, Y. W. *Int. J. Mod. Phys. B* **2003,** 17, 1134.
24. Zelenski, C. M.; Dorhout, P. K. *J. Am. Chem. Soc.* **1998,** 120, 734.
25. Chen, J., Li, S-L., Gao, F., Tao, Zh.-L. *Chem. Mater.* **2003,** 15, 1012.
26. Nath, M.; Rao, C. N. R. *Chem. Commun.* **2001**, 2236.
27. Nath, M.; Kar, S.; Raychaudhuri, A. K.; Rao, C. N. R. *Chem. Phys. Lett.* **2003,** 368, 690.
28. Remskar, M.; Mrzel, A.; Skraba, Z.; Jesih, A.; Ceh, M.; Demsar, J.; Stadelmann, P.; Levy, F.; Mihailovic, D. *Science* **2001,** 292, 479.
29. Remskar, M.; Skraba, Z.; Regula, M.; Ballif, C.; Sanjines, R.; Levy, F. *Adv. Mater.* **1998,** 10, 246.
30. Parilla, P. A.; Dillon, A. C.; Parkinson, B. A.; Jones, K. M.; Alleman, J.; Riker, G.; Ginley, D. S.; Heben, M. J. *J. Phys. Chem. B* **2004,** 108, 6197.

31. Hacohen, Y. R.; Popovitz-Biro, R.; Prior, Y.; Gemming, S.; Seifert, G.; Tenne, R. *Phys. Chem. Chem. Phys.* **2003,** 5, 1644.
32. Sen, R.; Govindaraj, A.; Suenaga, K.; Suzuki, S.; Kataura, H.; Iijima, S.; Achiba, Y. *Chem. Phys. Lett.* **2001,** 340, 242.
33. Schuffenhauer, C.; Parkinson, B. A.; Jin-Phillipp, N. Y.; Joly-Pottuz, L.; Martin, J.-M.; Popovitz-Biro, R.; Tenne, R. *Small* **2005,** 1, 1100.
34. Vollath, D.; Szabo, D. V. *Mater. Lett.* **1998,** 35, 236.
35. Vollath, D.; Szabo, D. V. *Acta Mater.* **2000,** 48, 953.
36. Li, X.-L.; Ge, J.-P.; Li, Y.-D. *Chem. Eur. J.* **2004,** 10, 6163.
37. Etzkorn, J.; Therese, H. A.; Rocker, F.; Zink, N.; Kolb, U.; Tremel, W. *Adv. Mater.* **2005,** 17, 2372.
38. Bastide, S.; Borra, J. P.; Duphil, D.; Levy-Clement, C. *Abstracts of Papers of the American Chemical Society* **2004,** 228, U482.
39. Chikan, V.; Kelley, D. F. *J. Phys. Chem. B* **2002,** 106, 3794.
40. Rapoport, L.; Bilik, Y.; Feldman, Y.; Homyonfer, M.; Cohen, S. R.; Tenne, R. *Nature* **1997,** 387, 791.
41. Chhowalla, M.; Amaratunga, G. A. J. *Nature* **2000,** 407, 164.
42. Joly-Pottuz, L.; Martin, J. M.; Dassenoy, F.; Belin, M.; Montagnac, G.; Reynard, B.; Fleischer, N. *J. Appl. Phys.* **2006,** 99, 023524/1.
43. Cizaire, L.; Vacher, B.; Le Mogne, T.; Martin, J. M.; Rapoport, L.; Margolin, A.; Tenne, R. *Surf. Coat. Technol.* **2002,** 160, 282.
44. Golan, Y.; Drummond, C.; Homyonfer, M.; Feldman, Y.; Tenne, R.; Israelachvili, J. *Adv. Mater.* **1999,** 11, 934.
45. Hu, X. G.; Hu, S. L.; Zhao, Y. S. *Lubric. Sci.* **2005,** 17, 295.
46. Greenberg, R.; Halperin, G.; Etsion, I.; Tenne, R. *Tribol. Lett.* **2004,** 17, 179.
47. Joly-Pottuz, L.; Dassenoy, F.; Belin, M.; Vacher, B.; Martin, J. M.; Fleischer, N. *Tribol. Lett.* **2005,** 18, 477.
48. Zhu, Y. Q.; Sekine, T.; Li, Y. H.; Fay, M. W.; Zhao, Y. M.; Poa, C. H. P.; Wang, W. X.; Roe, M. J.; Brown, P. D.; Fleischer, N.; Tenne, R. *J. Am. Chem. Soc.* **2005,** 127, 16263.
49. Zhu, Y. Q.; Sekine, T.; Li, Y. H.; Wang, W. X.; Fay, M. W.; Edwards, H.; Brown, P. D.; Fleischer, N.; Tenne, R. *Adv. Mater.* **2005,** 17, 1500.
50. Homyonfer, M.; Alperson, B.; Rosenberg, Y.; Sapir, L.; Cohen, S. R.; Hodes, G.; Tenne, R. *J. Am. Chem. Soc.* **1997,** 119, 2693.

51. Chen, J., Kuriyama, N., Yuan, H., Takeshita, H. T., Sakai, T. *J. Am. Chem. Soc.* **2001,** 123, 11813.

52. Zak, A.; Feldman, Y.; Lyakhovitskaya, V.; Leitus, G.; Popovitz-Biro, R.; Wachtel, E.; Cohen, H.; Reich, S.; Tenne, R. *J. Am. Chem. Soc.* **2002,** 124, 4747.

53. Imanishi, N.; Kanamura, K.; Takehara, Z. *J. Electrochem. Soc.* **1992,** 139, 2082.

54. Dominko, R., Arcon, D., Mrzel, A., Zorko, A., Cevc, P., Venturini, P., Gaberscek, M., Remskar, M., Mihailovic, D. *Adv. Mater.* **2002,** 14, 1531.

55. Afanasiev, P.; Rawas, L.; Vrinat, M. *Mater. Chem. Phys.* **2002,** 73, 295.

56. Mdleleni, M. M.; Hyeon, T.; Suslick, K. S. *J. Am. Chem. Soc.* **1998,** 120, 6189.

57. Bollinger, M. V.; Lauritsen, J. V.; Jacobsen, K. W.; Norskov, J. K.; Helveg, S.; Besenbacher, F. *Phys. Rev. Lett.* **2001,** 87, 196803/1.

58. Li, Y.-W.; Pang, X.-Y.; Delmon, B. *J. Phys. Chem. A* **2000,** 104, 11375.

59. Massalski, T. B.; Okamoto, H.; Subramanian, P. R.; Kacprzak, L., *Hf-Re to Zn-Zr*. 2nd ed.; ASM International,: Ohio, 1990; Vol. 3, p 2664.

60. *TOPAS*, 3.0P; Bruker AXS: Karlsruhe, 2003.

61. Schutte, W. J.; De Boer, J. L.; Jellinek, F. *J. Solid State Chem.* **1987,** 70, 207.

62. Coelho, A. *TOPAS Academic*, 1.0; Bruker AXS.

63. Dunn, D. N.; Seitzman, L. E.; Singer, I. L. *J. Mater. Res.* **1997,** 12, 1191.

64. Margolin, A.; Rosentsveig, R.; Albu-Yaron, A.; Popovitz-Biro, R.; Tenne, R. *J. Mater. Chem.* **2004,** 14, 617.

65. Si, P. Z.; Zhang, M.; Zhang, Z. D.; Zhao, X. G.; Ma, X. L.; Geng, D. Y. *J. Mater. Sci.* **2005,** 40, 4287.

66. Sloan, J.; Hutchison, J. L.; Tenne, R.; Feldman, Y.; Tsirlina, T.; Homyonfer, M. *J. Solid State Chem.* **1999,** 144, 100.

67. Meyer, K. *Physikalisch-chemische Kristallographie*. Dt. Verl. für Grundstoffindustrie: Leipzig, 1977; p 368 pp.

4 *In situ* heating TEM study of onion-like WS_2 and MoS_2 nanostructures obtained via MOCVD

4.1 Introduction

The synthesis of nanostructures from layered materials such as onion-like particles and nanotubes was first achieved in the carbon system.[1, 2] Tenne and co-workers opened up the pathway to another class of compounds, the layered transition metal chalcogenides MQ_2 (M=transition metal, Q=S, Se, Te), that are forming similar morphologies, and dubbed them inorganic fullerene-like materials (IF).[3-6] Various synthesis techniques for these IFs have been established so far, among them oxide to sulfide conversion,[7-11] decomposition of suitable precursors,[12-15] transport reactions,[16-18] laser ablation,[19-21] arc discharge, template methods,[8] microwave synthesis[22, 23] and chemical vapor deposition (CVD).[24]

Except for the oxide to sulfide conversion, which has been scrutinized[25, 26] the growth mechanism of such nanostructures is still subject to discussion. Understanding the principles of the growth mechanism will facilitate to tailor the chemical synthesis according to specific needs concerning compound, size, morphology etc. *In situ* heating transmission electron microscopy is a powerful method to monitor structural changes,[27-31] nucleation processes[32] and phase evolutions[21, 33, 34] during the process itself. In this contribution, we will employ this technique to evaluate the growth mechanism of MS_2 (M=Mo, W) nanoparticles synthesized via the MOCVD method.

Recently, the synthesis of inorganic fullerene-like MoS_2, $MoSe_2$, and WS_2 particles with the aid of the metal-organic chemical vapor deposition (MOCVD) method was reported.[35, 36] The results of a two-step and a single-step reaction process were compared.[36] The two-step synthesis consisted of the MOCVD process of primary nanoparticles followed by an annealing in inert atmosphere in a conventional tube furnace. For the single-step process the MOCVD synthesis was carried out at higher temperatures without isolating the intermediate product. Depending whether a two-step or a single-step process was used the main product consisted of hollow or filled onion-like structures, respectively. The MOCVD synthesis alone resulted in the formation of two types of nanoparticle intermediates: (i) small, irregular shaped particles (S-type) and (ii) bigger, round particles (R-type). Annealing in argon led to two types of product nanoparticles: (i) needle-like, well-crystallized (N-type) and (ii) hollow onion-like particles (O-type).

The parameter fields (*e.g.* temperature within the MOCVD reactor, heating/cooling rates, gas flow, annealing time, annealing temperature etc.) are large, thus, the set of parameters for optimum synthesis conditions is difficult to screen experimentally. The resemblance in morphology of round (R) and hollow onion-like (O) particles on the one hand and small, straight layered (S) and needle-like (N) particles on the other hand lent support to the hypothesis that R- and O-, as well as S- and N-type particles, respectively, are in some way related to each other. If S- and R-type particles were intermediates in the formation of N- and O-particles, an optimization should mainly concern the first MOCVD reaction step. Otherwise, the influence of reaction parameters of the annealing process such as temperature, time and gas flow should be more thoroughly examined.

In order to understand the transformation of S- and R-type particles upon annealing, we followed their structural evolution by *in situ* heating in a transmission electron microscope (TEM) thereby extracting information about the growth mechanism of inorganic fullerene-like particles (by real-space imaging) as well as their ordering and crystallinity (by electron diffraction).

4.2 Experimental

The experiment requires two steps: (i) the synthesis of MS_2 (M=Mo, W) nanoparticles and (ii) the subsequent annealing within a transmission electron microscope.

4.2.1 MOCVD synthesis

Reactants ($M(CO)_6$ (M=Mo, W) and S) are heated with the aid of heating tapes in the left and right arms of a T-shaped quartz reactor setup. An Ar flow transports the reactants to the reaction zone which is located in the coil of an induction furnace. A schematic representation of the experimental setup for this first step and a more detailed description of the experimental conditions was given by Etzkorn et al.[35] The MS_2 (M = M, W) samples obtained in this first reaction step are named MOCVD product in the sequel, T_{ind} corresponds to the reaction temperature of the MOCVD experiment, *i.e.* the temperature of the induction coil. For the two-step process (MOCVD + annealing), T_{anneal} and t_{anneal} are the annealing temperature [°C] and annealing time [h] of the subsequent annealing step in Ar in a tube furnace. MOCVD products are labeled MS_2 (T_{ind}) and MS_2 (T_{ind}/T_{anneal}-t_{anneal}) for products of the two-step process (see also chapter three).

4.2.2 *In situ* heating TEM study

For this second step, samples synthesized at 450°C were deposited on a Cu grid coated with a holey amorphous carbon film (Plano, S147-3) from an ethanolic suspension. The grids were placed in a single tilt heating stage (GATAN). To minimize thermal drift, a water cooling of the outer part of the sample holder was installed.

Before heating, the sample was screened for suitable particles and their positions were registered. Image recording was started only after temperature constancy/stability had been achieved throughout the sample. The sample was subsequently analyzed at 200, 250, 300, 350, 400, 450, 500, 600, 700, and 800°C for the WS_2 and at 100, 300, 500, 600, 700, 750°C for the MoS_2 samples.

4.2.3 Instrumental details

Transmission electron microscopy (TEM) was performed on a Philips CM12 instrument at an acceleration voltage of 120 kV. High-resolution (HR) and *in situ* heating studies were carried out on a FEI TECNAI F30 ST microscope (300kV acceleration voltage, field emission gun). Fourier filtering was employed for noise-reduction in some of the images. An example of the procedure is given in the supplementary information.

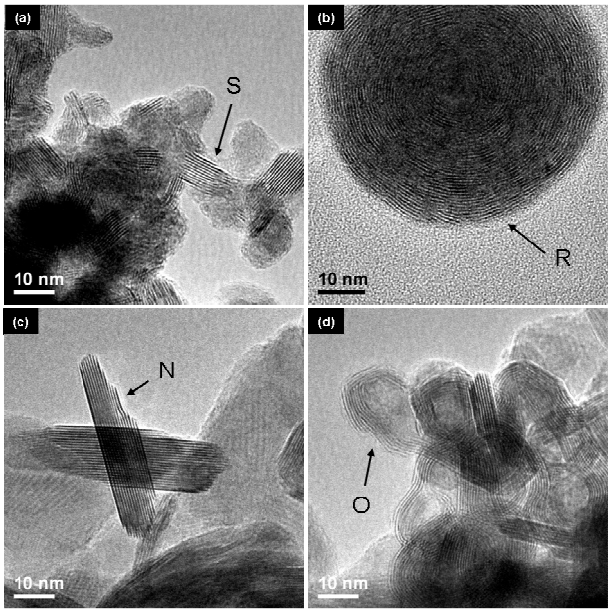

Figure 4-1. HRTEM images of (a) small particles (S) with straight layers and (b) round particles (R) in a pristine WS_2 (750) sample and of (c) needle-like (N) and (d) onion-like (O) particles in an annealed WS_2 (450/800-1) sample. Note, R-type particles (b) in low temperature (450°C) syntheses are similar in morphology but do not exhibit layer fringes.

4.3 Results and Discussion

4.3.1 Pristine sample at the example of WS_2

Figure 4-1(a) and (b) show the pristine WS_2 particles, (i) small, irregular shaped particles (S-type) and (ii) bigger, round particles (R-type) that were obtained from the MOCVD process at 750°C before the annealing step. Figure 4-1(c) and (d) display the (i) needle-like, well-crystallized (N-type) and (ii) hollow onion-like particles (O-type) particles resulting from the subsequent annealing step under argon.

Figure 4-2 displays an overview TEM image of a WS_2 (450) sample before annealing. The pristine material consists of a network-like agglomerate of nanoparticles. Two distinct types of particles can be observed: smaller, irregular-shaped particles (named S-type hereafter) and bigger round particles (R-type). High-resolution pictures of a typical S- and R-type particle are shown in Figure 4-2(b) and (c), respectively.

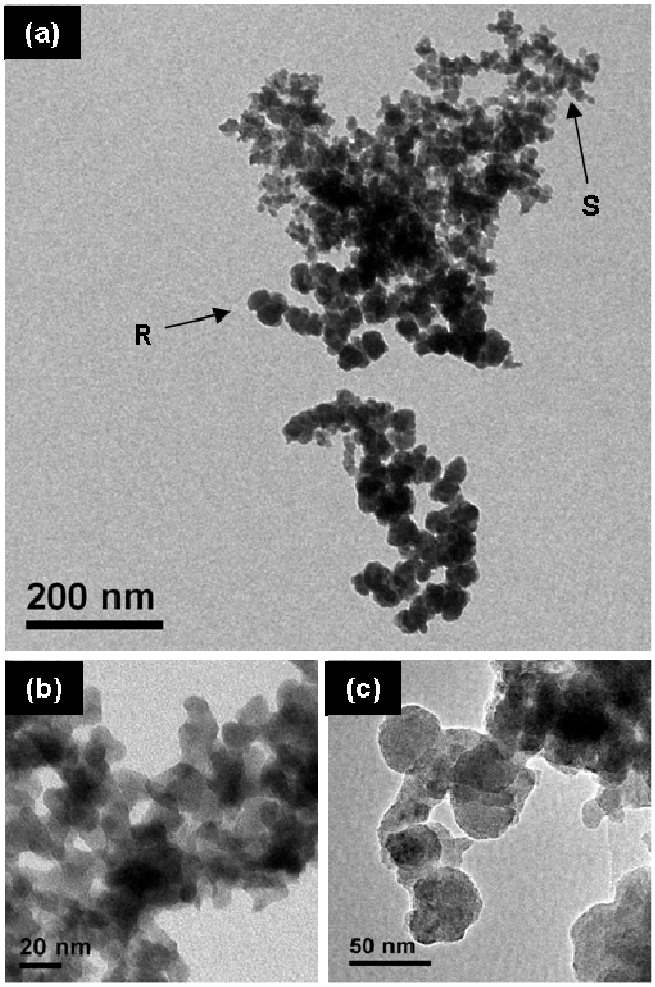

Figure 4-2. TEM image of a WS_2 (450) sample (a). High resolution TEM micrographs of S- (b) and R-type (c) particles.

4.3.2 *In situ* heating TEM study

In the following section, the results of the *in situ* heating TEM studies are presented, first for WS_2 and then for MoS_2.

4.3.2.1 Tungsten disulfide

In Figure 4-3 a high resolution TEM image of an R-type particle heated to 250°C is shown. The following discussion is based on the evolution of three marked areas (white rectangles) upon annealing.

Figure 4-4 represents Fourier filtered HRTEM images of the central part of the R-type particle (area 1 in Figure 4-3). At 250°C, layer formation in the central part can already be observed. This contradicts a strict outward-in growing process as might have been expected. The inner part is more or less an isotropic amorphous mixture. Therefore, no preferred orientation of the layers, *e.g.* to avoid dangling bonds, should be observed. This is indeed the case, as can be seen from the arbitrary orientation of the colored lines (representing a parallel package of layers) in Figure 4-4(a). At 400°C (b) the orientation of the red line has turned about 90°. This re-orientation may be triggered by an incoming outer layer front (black line), thus leading to the observed re-arrangement of the inner layers (red line).

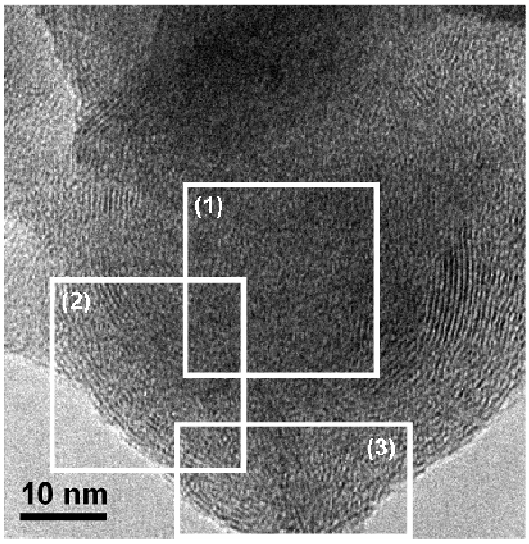

Figure 4-3. HRTEM picture of an R-type particle at 250°C. The structural transformation within three marked areas (white rectangles) is monitored in the sequel.

This process of reorientation in favor of tangential layers can also be observed exemplarily considering the yellow line in Figure 4-4(b). At 600°C (Figure 4-4(c)) a tangential orientation of the layer packages emerges. The size of the layers has increased in both directions and an incipient bending of the layers is observed. At 800°C (Figure 4-4(d))

adjacent layer packages are joined at their edges enclosing one half of the particle center. Only few defects are remaining.

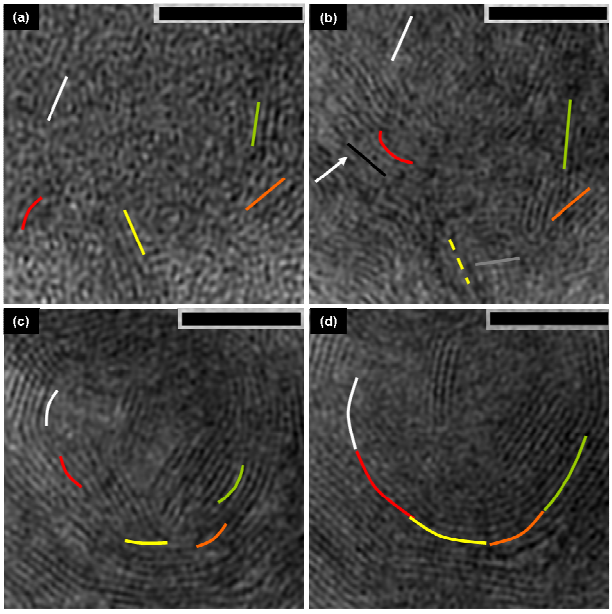

Figure 4-4. Evolution in the central part (area 1 in Figure 4-3) of R-type particles monitored by means of IFFT of HRTEM images upon annealing at 250 (a), 400 (b), 600 (c) and 800°C (d). Colored lines mark areas with WS_2 layers. The center remains filled throughout the heating. Scale bar = 10 nm.

In the second area of Figure 4-3 (shown in detail in Figure 4-5), the layer formation at the particle boundary can be studied. Between 250 (Figure 4-5(a)) and 400°C (Figure 4-5(b)) WS_2 layers are formed tangentially to the outer boundary. Along the layer numerous defects can be observed (arrows). Note that stacking faults between layers would not abound. At higher temperatures, first the defects in the outer layers start healing (Figure 4-5(c)) followed by those in the more central portion of the particle, according to a defect annealing kind of process.

Two processes can be observed in the third area of Figure 4-3 (shown in detail in Figure 4-6). WS_2 layers that are stacked along the radial direction exhibit unsaturated bonds at the outer surface ("dangling bonds"). This is energetically unfavorable. Therefore, a transformation to the thermodynamically more stable arrangement of tangential layers occurs at higher temperatures (see white arrow Figure 4-6(a-c)).

Upon annealing the simultaneous formation and growth of WS_2 layers at different positions becomes evident. Interconnection of two layer packages leads to defects resembling edge dislocations that are subsequently healed upon annealing (see black arrow in Figure 4-6(a-c)).

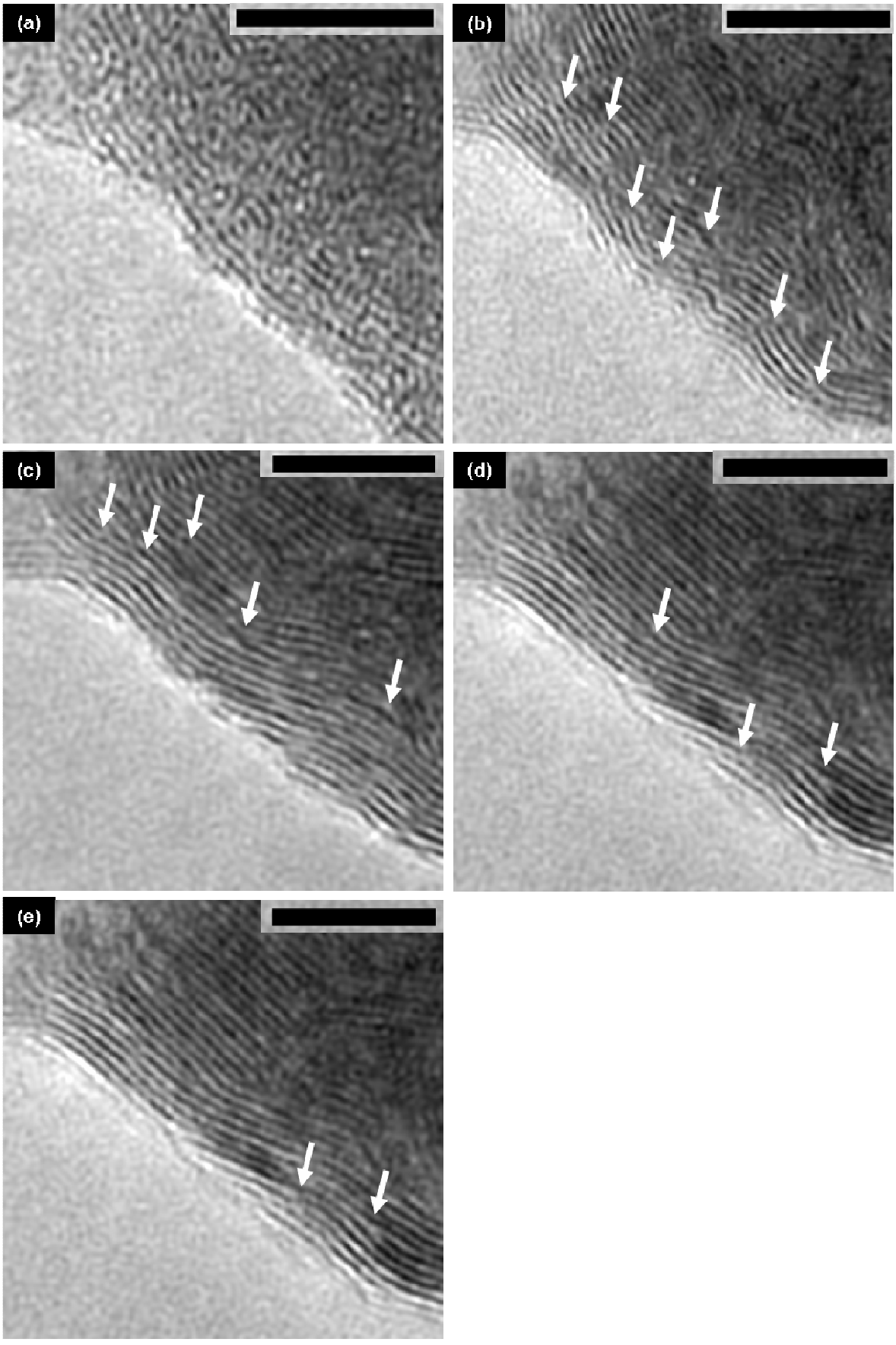

Figure 4-5. IFFT of HRTEM images of an area at the particle boundary (area 2 in Figure 4-3) at 250 (a), 400 (b), 600 (c), 700 (d) and 800°C (e). Some defects are marked with white arrows. Scale bar = 10 nm.

d_{002}-values as obtained from FFT analyses of the *in situ* heating TEM images are well above the d_{calc}-value = 0.616 nm for the bulk material. This can be attributed to a large number of defects, *e.g.*, interstitial atoms between the layers.

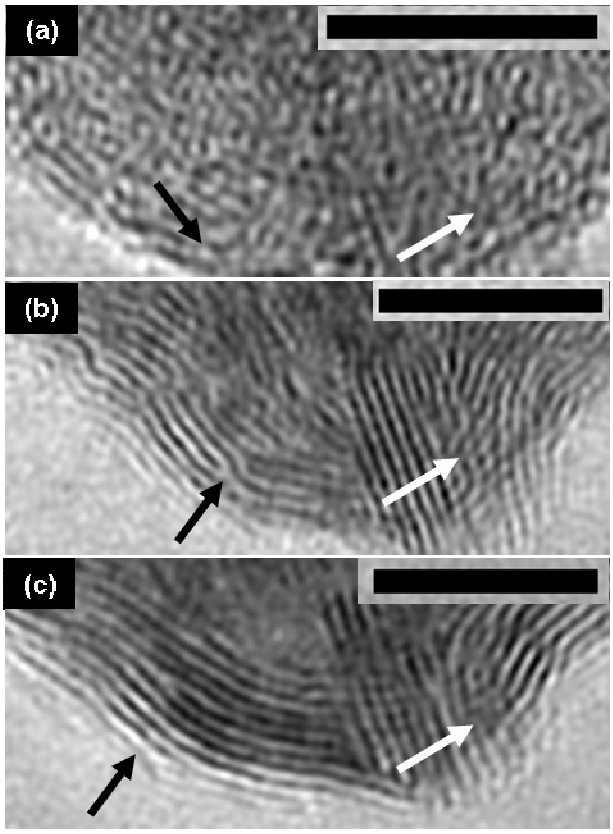

Figure 4-6. IFFT of HRTEM images of an R-type particle heated at 250 (a), 400 (b), and 800°C (c). Successive healing of defects and transformation of radial to tangential layers are indicated with black and white arrows, respectively. Scale bar = 10 nm.

In conclusion, annealing of spherical amorphous WS_2 particles leads first to the nucleation of several crystallites which coalesce upon sustained annealing at higher temperatures. Grains whose basal planes are parallel to the surface of the particles are preferred since surface dangling bonds can be prevented. Hence, an energetically favorable structure with spherically closed concentric layers is formed (see Figure 4-7).

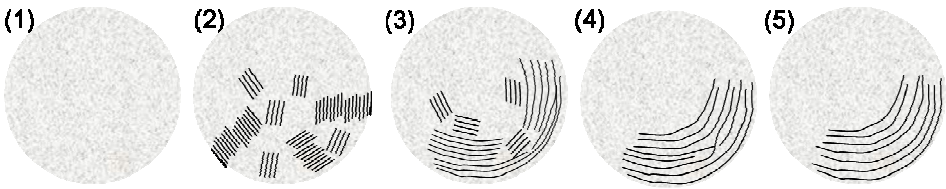

Figure 4-7. Schematic growth mechanism for R-type particles in a WS_2 sample: Amorphous material (1), incipient layer formation (2), preferred formation of closed shells at the boundary with basal layers parallel to the surface (3), movement of defects to the outside (4), formation of closed shells (5). Layers are only shown for part of the particle.

Small straight-layered (S) particles, which are already crystalline before annealing, become nearly defect-free when heated to 250°C (Figure 4-8a). Further annealing does not lead to a significant increase in layer size or number of layers or to the formation of anisotropic, needle-like structures (N-type) as observed in annealed samples. At some positions, a bending of layer packages can be observed at higher temperatures (Figure 4-8b).

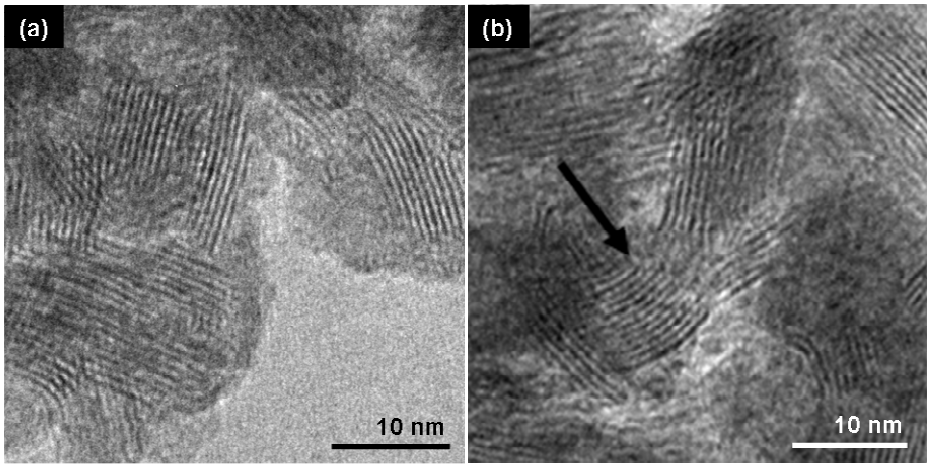

Figure 4-8. HRTEM images of S-type WS_2 particles at 250 (a) and 800°C (b). Bending of layers is indicated with a black arrow.

A possible explanation for the lack of layer growth as compared to the round (R) particles might be related to the different nature of the original amorphous material for S- and R-type particles. In R-type particles a stoichiometric mixture of W : S = 1: 2 is achieved whereas in S-type particles tungsten is prevailing as was shown by energy dispersive X-ray analyses. We assume that during the heating process polynuclear metal clusters are formed by decarbonylation. Eventually this process leads to the formation of W clusters or nanoparticles.

$$(4\text{-}1) \quad 2\ W(CO)_6 \xrightarrow{\Delta T} W_2(CO)_{10} + 2\ CO \xrightarrow{\Delta T} ..... \xrightarrow{\Delta T} W_n$$

In the reaction zone of the MOCVD setup, sulfur from the gas phase will react with a part of this amorphous W material resulting in the formation of amorphous S-type WS_2 particles. The amount of sulfur that diffuses into these W-clusters is limited and therefore only nano-sized particles can be formed. The vacuum in TEM prevents the delivery of more sulfur from other parts of the sample to the S-type particles. Therefore the heating leads only to an increase in crystallinity, but not in the size of the particles. In contrast, when the sample is annealed under Ar, sulfur from sulfur-rich parts of the sample can be transported to the S-type WS_2 particles where it reacts with the outermost layer of still unreacted amorphous W to complete the formation of WS_2. It is likely, that the formation of new WS_2 is more favorable at the edges of the WS_2 sheets (where unsaturated metal atoms are present). This leads to

anisotropic particle growth perpendicular to the stacking direction *c*. It remains unclear, why needles and not slabs are formed, as *a* and *b* direction are crystallographically equivalent. A preferred growth in only one of these directions is difficult to rationalize.

One possible explanation might be the presence of WO_x impurities (with adsorbed water or air as oxygen source) as a reaction intermediate as WO_x is known to exhibit needle-like morphology and a subsequent resulfurization would then be responsible for this peculiar behavior.

The amorphous R-type particles on the other hand should consist of an intimate mixture of W and S on an atomic scale. The presence of both W and S is confirmed by EDX analyses in a 1:1.5 – 1:2 ratio. The amount of S as a much lighter material than W might be underestimated by EDX semi-quantitative analysis. The spherical morphology of R-type particles could hint to the growth from a liquid sulfur droplet into which W is diffused.

4.3.2.2 Molybdenum disulfide

In the following section, the results for *in situ* heating experiments of MoS_2 obtained from a MOCVD synthesis at 450°C will be discussed.

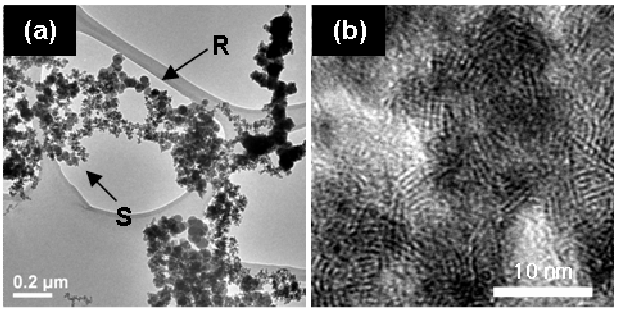

Figure 4-9. TEM overview (a) and HRTEM of S-type particles in a MoS_2 sample before annealing. Refer to text for definition of S- and R-type particles marked with arrows in (a).

The R-type particles are amorphous. In some of them, small layer fragments (d_{002} = 0.645 nm) in the outer region can be observed already at room temperature. At 100°C more layered material is formed at the particle boundaries and primarily tangential to them. At 300°C layer fragments can be seen throughout the particle, *i.e.* the major portion of the amorphous material has transformed to MoS_2.

The newly formed layers exhibit a vast number of defects. Upon further heating a defect annealing takes place in both, the central and outer parts of the particles, leading to increased crystallinity. Simultaneously, a transformation from non-tangential to tangential layers is observed. Bending of layers starts as early as at 500°C.

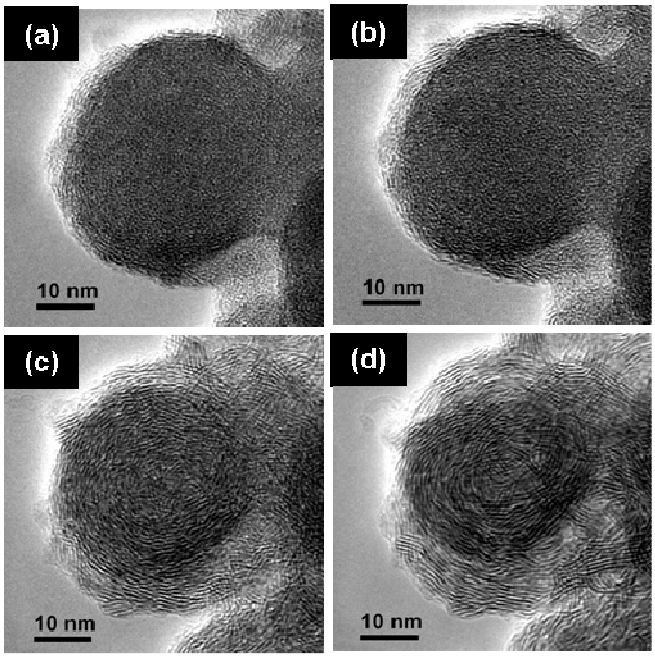

Figure 4-10. TEM image of an R-type particle in a MoS_2 sample at 24 (a), 100 (b), 300 (c) and 500°C (d).

At about 700 - 750°C, the continued healing of defects and the bending of layers leads to the formation of onion-like particles with a hollow core (Figure 4-11). The d_{002}-values scatter strongly. Among the variety of R-type particles, two extremes can be distinguished according to their size: (i) particles with diameters of 50 nm and less (majority, Figure 4-11(a)) and those with diameters of 100 nm and more (only few examples, Figure 4-11(b)). Surprisingly, the larger particles do not contain significantly more outer layers (30-50 layers) than the smaller ones (10-30 layers), but have a rather distinctly larger hollow core compared to the smaller ones. Two explanations for the occurrence of the restricted number of layers are feasible: (i) material depletion, *i.e.* no amorphous "material" that could crystallize is available any more or (ii) the time/temperature of reaction was not sufficient to complete the reaction. As in samples heated for 12 h (and more) under Ar at 800°C no filled onion-like structures could be observed even for large particles, we think that a "shortage" of material is responsible for the formation of hollow nanoparticles with a restricted number of layers. A similar phenomenon was observed in the formation of hollow calcium carbonate particles and was attributed to densification upon crystallization of amorphous calcium carbonate along with an outward-in growing mechanism.[37]

S-type particles consist of up to 6, essentially defect-free layers with a maximum width of 5 nm and show only minor growth upon annealing. A minor part of the primary particles showed a resemblance in their outer morphologies to S-type particles, although only very few or no (002)-layer fringes were observed. A more detailed analysis revealed weak lattice fringes with d = 0.224 nm ± 0.046 which corresponds either to elemental Mo

(d_{110} = 0.223 nm) or 2H-MoS_2 (d_{103} = 0.228 nm). Upon annealing, a "halo" of lighter contrast appeared and the formation of very few (002) lattice fringes was noticed at the boundaries.

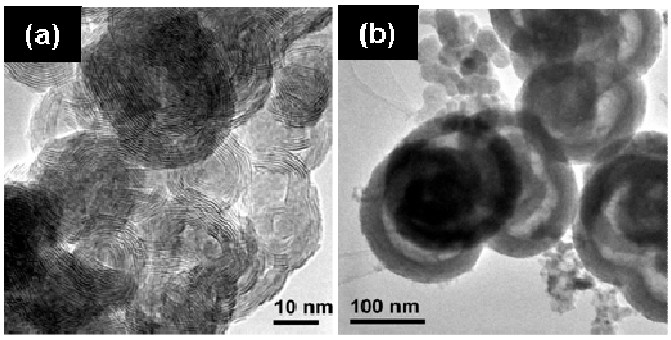

Figure 4-11. TEM images at 700°C of hollow onions in a MoS_2 sample. Note the significantly larger hollow core for bigger particles (b) as compared to particles of half the size (a).

In EDX analyses, Mo, C, O and Cu (due to the grid) could clearly be identified. Due to the overlap of the S(K)- and Mo(L)-signal the Mo/S ratio could not be evaluated. Nevertheless, the results peak fitting with and without S point towards the absence of S in these. Thus, we think that this part of the sample can be attributed to Mo-clusters in analogy to the results presented above for the formation of WS_2.

4.3.2.3 Comparison of IF-WS_2 and IF-MoS_2

In this last section we compare the results for tungsten and molybdenum sulfide. In both compounds the crystallization of the pristine sample, consisting of two types of particles (small, straight-layered (S), round (R)), starts upon annealing with more or less randomly orientated layers. To minimize the amount of unsaturated bonds at the MS_2-layer edges (twofold coordination instead of threefold for S, fourfold coordination instead of six-fold for the transition metal[38]) a transformation of layers arranged in a random or non-tangential orientation into tangential layers in the R-type particles takes place. The large number of defects (*e.g.* edge dislocations) observed in the primary particles is reduced considerably upon annealing. Hollow onion-like particles are formed in this step. Annealing has no considerable effect on the S-type particles except for healing of the small amount of defects and a slight increase in size. This was attributed to sulfur deficiency in the metal clusters (M = Mo, W) formed in the initial phase of the synthesis by the thermal decarbonylation of the metal carbonyl precursors.

Despite the similarities in the general morphology of WS_2 and MoS_2 particles and their behavior upon annealing some noteworthy differences are observed:

(i) the formation of the R-type particles for MoS_2 starts already in the pristine samples,

(ii) the nucleation and growth, *i.e.* the formation of layers of ordered "crystalline" from amorphous material (although defects are still present) is completed at lower temperatures (< 300°C) for MoS_2 compared to WS_2 (400-500°C),

(iii) the crystallization process seems different: for MoS_2, the layer formation starts throughout the R-type particle, and the layers are already tangentially aligned. Above 300°C, the healing of defects is the predominant process. In contrast, for WS_2, the crystallization starts at the outer particle boundaries (although some arbitrarily oriented layer fragments are also present in the central portion of the particles). An outside-in growing process of the tangentially oriented outer layers finally leads to a reorientation of the central layer fragments. This development takes place over a wide temperature range (300 to 800°C) in contrast to the very fast process in MoS_2.

In summary, we conclude that the formation of IF-MoS_2 proceeds more smoothly than that of IF-WS_2. This may be attributed to stronger metal-metal-bondings for W as compared to Mo, hampering the reaction with sulfur.

4.3.2.4 Comparison to the ex situ-annealed sample

The present TEM *in situ* heating study establishes a link between the morphologies of MoS_2 and WS_2 nanoparticles obtained by MOCVD before and after annealing under Ar, *i.e.* between S- and N-type particles on the one hand and R- and O-type particles on the other hand. For both compounds, MoS_2 and WS_2, a transformation of R-type particles into hollow onions (similar to O-type particles obtained from ex situ-annealing experiments) could be demonstrated.[36] The crystallinity of the ex-situ samples is slightly higher than that of the *in situ* samples. This can be attributed to enhanced surface diffusion (and therefore more facile particle growth) in the surrounding Ar gas atmosphere compared to the vacuum in a transmission electron microscope, where no surface diffusion is possible.

An (anisotropic) growth of S-type particles into needle-like (N-type) structures could not be observed. We therefore believe that surface diffusion (*i.e.* presence of a gas phase) plays a substantial role in the formation of N-type particles.

Nevertheless, the present study shows that the amount of the desired hollow onion-like structures originates from R-type particles present in the pristine sample. The screening of optimized parameters for a (preferable) pure O-type sample should therefore essentially be limited to the reaction parameters of the MOCVD setup (such as reaction temperature and time, gas flow, choice of precursors, geometry of the glass setup, ...).

4.4 Conclusion

To summarize, the *in situ* heating TEM study of MoS_2 and WS_2 nanoparticles obtained via MOCVD allowed us to monitor the growth mechanism of hollow onion-like nanoparticles in which defect annealing processes play a major role. A relationship between particles of the pristine sample with a round morphology (R-type) and the resulting hollow onion-like particles (O) could be established (Figure 4-12). Therefore, an optimization of the synthesis of such hollow fullerene-like structures should primarily concern the optimization of the MOCVD process in order to obtain only R-type particles in the first reaction step that can be converted to IF-MQ_2 (M = Mo, W) by subsequent annealing. S-type particles did not grow into needles upon *in situ* annealing. Although the morphologies of the pristine particles (MoS_2/WS_2) obtained during the first step of the synthesis are similar, the layer formation in the MoS_2 primary particles proceeds more smoothly than that for WS_2.

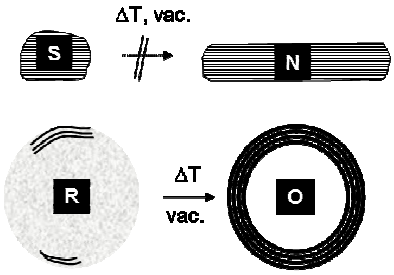

Figure 4-12. Schematic representation of monitored particle development during *in situ* heating TEM study. Refer to text for particles type (S, N, R, O) definition.

4.5 References

1. Kroto, H. W.; Heath, J. R., et al. *Nature* **1985,** 318, 162.
2. Iijima, S. *Nature* **1991,** 354, 56.
3. Tenne, R.; Margulis, L., et al. *Nature* **1992,** 360, 444.
4. Tenne, R.; Margulis, L., et al. *Adv. Mater.* **1993,** 5, 386.
5. Homyonfer, M., Mastai, Y., Hershfinkel, M., Volterra, V., Hutchison, J.L., Tenne, R. *J. Am. Chem. Soc.* **1996,** 118, 7804.
6. Tenne, R.; Margulis, L., et al. *Mater. Res. Soc. Symp. Proc.* **1995,** 359, 111.
7. Rothschild, A.; Tenne, R., et al. *Chem. Commun.* **1999**, 363.

8. Whitby, R. L. D.; Hsu, W. K., et al. *Chem. Phys. Lett.* **2002,** 359, 68.
9. Hsu, W. K.; Zhu, Y. Q., et al. *Adv. Funct. Mater.* **2001,** 11, 69.
10. Therese, H. A.; Li, J. X., et al. *Solid State Sci.* **2005,** 7, 67.
11. Li, X. L.; Li, Y. D. *Chem. Eur. J.* **2003,** 9, 2726.
12. Nath, M.; Govindaraj, A., et al. *Adv. Mater.* **2001,** 13, 283.
13. Nath, M.; Rao, C. N. R. *Chem. Commun.* **2001**, 2236.
14. Zelenski, C. M.; Dorhout, P. K. *J. Am. Chem. Soc.* **1998,** 120, 734.
15. Chen, J., Li, S-L., Gao, F., Tao, Zh.-L. *Chem. Mater.* **2003,** 15, 1012.
16. Zhu, Y. Q.; Hsu, W. K., et al. *J. Mater. Chem.* **2000,** 10, 2570.
17. Remskar, M., Mrzel, A., Skraba, Z., Jesih, A., Demsar, J., Stadelman, P., Levy, F., Mihailovic, D. *Science* **2001,** 292, 479.
18. Remskar, M.; Mrzel, A., et al. *Adv. Mater.* **2003,** 15, 237.
19. Nath, M.; Rao, C. N. R., et al. *Chem. Mater.* **2004,** 16, 2238.
20. Sen, R.; Govindaraj, A., et al. *Chem. Phys. Lett.* **2001,** 340, 242.
21. Schuffenhauer, C.; Parkinson, B. A., et al. *Small* **2005,** 1, 1100.
22. Vollath, D.; Szabo, D. V. *Mater. Lett.* **1998,** 35, 236.
23. Vollath, D.; Szabo, D. V. *Acta Mater.* **2000,** 48, 953.
24. Etzkorn, J.; Therese, H. A., et al. *Adv. Mater.* **2005,** 17, 2372.
25. Tenne, R.; Homyonfer, M., et al. *Chem. Mater.* **1998,** 10, 3225.
26. Tenne, R. *Chem.-Eur. J.* **2002,** 8, 5297.
27. Lee, H. J.; Ni, H., et al. *Mater. Trans.* **2006,** 47, 527.
28. Hu, P. A.; Liu, Y. Q., et al. *Appl. Phys. A* **2005,** 80, 1413.
29. Agrawal, A.; Cizeron, J., et al. *Microsc. Microanal.* **1998,** 4, 269.
30. Rankin, J. *J. Am. Ceram. Soc.* **1999,** 82, 1560.
31. Rankin, J.; Sheldon, B. W. *Mater. Sci. Eng. A* **1995,** 204, 48.
32. Hidaka, K.; Tanikoshi, S., et al. *Mater. Trans. JIM* **1995,** 36, 251.
33. Chatterjee, K.; Howe, J. M., et al. *Acta Mater.* **2004,** 52, 2923.
34. Ballif, C.; Regula, M., et al. *Surf. Sci.* **1996,** 366, L703.
35. Etzkorn, J.; Therese, H. A., et al. *Adv. Mater.* **2005,** 17, 2372.
36. Zink, N.; Pansiot, J., et al. *J. Am. Chem. Soc.* **2006**, submitted.
37. Loges, N.; Graf, K., et al. *Langmuir* **2006,** 22, 3073.
38. Tenne, R. *Angew. Chem.-Int. Edit.* **2003,** 42, 5124.

5 Low temperature synthesis of monodisperse ZrO_2 nanoparticles with high specific surface area

5.1 Introduction

The synthesis of MSe_2 (M=Zr, V, Nb, Mo) nanoparticles by a solvothermal approach was attempted from the corresponding oxalates (ox) or acetylacetonates (acac) and *in situ* generated H_2Se under various conditions summarized in Table 5-1. Although the selenides were only obtained in their bulk form or not at all, interesting nanostructures of zirconia were achieved, and a thorough study to optimize the synthesis parameters was carried out. The results of this study will be presented in the sequel.

Table 5-1. Parameters for the attempted synthesis of MSe_2 nanostructures.

Precursor (M)	Precursor (X)	Solvent	T
$Mo(ox)_3$	Se + ß-sitosterol	Toluene	340
	Se	Toluene	340
	-	Toluene	340
	-	-	340
$VO(ox)_2$	Se + ß-sitosterol	Toluene	380
$VO(acac)_2$	Se + ß-sitosterol	Toluene	380
	Se	Toluene	380
	ß-sitosterol	Toluene	380
	-	Toluene	380
	-	-	380
$(NH_4)_3NbO(ox)_3 \cdot 2H_2O$	Se + ß-sitosterol	Toluene	240
	Se + ß-sitosterol	Toluene	380
	Se	Toluene	240
	-	Toluene	240
$Zr(ox)_2 \cdot 4H_2O$	Se + ß-sitosterol	Toluene	380
	-	Toluene	380
	-	-	380

Zirconia is a non-toxic material that finds application in numerous fields (catalysis,[1, 2] solid oxide fuel cells,[3-5] mem-branes,[6] thermal barrier coatings,[7, 8] dental filling ceramics,[9, 10] high performance liquid chromatography (HPLC) packings,[11] wear material,[12, 13] gas sensors[14]) due to its interesting properties such as chemical resistance, high melting point, high hardness and toughness, defect chemistry and the resulting ionic conductivity, low thermal conductivity paired with a large thermal expansion coefficient.[15]

These properties can be improved when using nano-sized (n) ZrO_2, *e.g.* n-ZrO_2 exhibits superior sintering behavior[16, 17] and superplasticity.[18-20] The high surface to volume ratio of n-ZrO_2 is ideal in the field of catalysis both as catalyst or catalyst support.[21]

The synthesis methods for n-ZrO_2 comprise sol-gel,[22-26] inverse micelle technique,[27-30] forced hydrolysis,[28, 31, 32] thermal decomposition,[33, 34] hydro- and solvothermal approaches,[35-38] plasma spraying,[39] flame spray pyrolysis,[40-42] thermal hydrolysis,[43] gas condensation,[44, 45] template-based,[46] chemical vapor synthesis,[17] inorganic metathesis,[47] and mechano-chemical[48-50] synthesis approaches

ZrO_2 has three polymorphs: The monoclinic (m) form is the stable modification at room-temperature up to 1170°C at atmospheric pressure, the tetragonal (t) one between 1170 and 2370°C.[51] Above this temperature a phase transition into the cubic (c) modification is observed. A high-pressure synthesis leads to the formation of several orthorhombic (o) modifications.[24, 52, 53] From the application point of view, the tetragonal and cubic phases are preferred over m-ZrO_2. Therefore, a stabilization of these modifications at room temperature and the operation temperature, respectively, is a main issue. So far, two main routes for the synthesis of partially or fully stabilized t- or c-ZrO_2 are in use: (i) doping with cations such as rare earth elements (Y^{3+} and Sc^{3+})[54] or (ii) limiting the grain size to the nanometer range.[32]

Here, we report on a simple high-yield and low-temperature synthesis of monodisperse m- and t-ZrO_2 nanoparticles and t-ZrO_2 nanostructured material with high specific surface areas using the decomposition of $Zr(C_2O_4)_2{\cdot}4H_2O$ within an autoclave, which can be upscaled easily. X-ray diffraction (XRD), small angle X-ray scattering (SAXS), scanning electron microscopy (SEM), transmission electron microscopy (TEM), N_2 sorption according to Brunauer-Emmett-Teller, photoluminescence and Raman spectroscopy were employed to characterize the materials. The effect of autogenic pressure, *i.e.* surface diffusion, on the formation of nanoparticles was studied.

5.2 Experimental Details

5.2.1 Synthesis

$Zr(C_2O_4)_2{\cdot}4H_2O$ was prepared as follows: 1.7 g of $ZrCl_4$ (Alfa Aesar, 99.5%) were suspended in 25 mL of Methanol (p.a., Fluka); 7.5 mL of warm 2M oxalic acid aqueous solution (prepared from 99+% oxalic acid dihydrate, Fluka) were then added to the yellow suspension. The white precipitate was filtered and washed several times with small amounts of deionized water and isopropanol (p.a., Fluka), then dried overnight. X-ray diffraction (XRD) measurements showed the formation of $Zr(C_2O_4)_2{\cdot}4H_2O$ (JCPDS card no. 12-0859).[55]

The decomposition temperatures of 300 and 380°C, respectively, were chosen from the results of differential thermal analysis (DTA). 0.3 g of $Zr(C_2O_4)_2 \cdot 4H_2O$ were enclosed in a stainless steel autoclave (AC) described elsewhere[56] or placed on an Al_2O_3 boat in a tube furnace (TF). The sample underwent a slowly heating (1 K/min) to 300 and 380°C, respectively, was held at that temperature for 12h and then cooled to room temperature (5K/min). The white product was filtered and then washed with isopropanol. Table 1 gives an overview of the synthesis conditions and the sample labeling.

Table 5-2. Experimental conditions and labeling.

T_{decomp} [°C]	Method	Name
300	Autoclave	300AC
	Tube furnace	300TF
380	Autoclave	380AC
	Tube furnace	380TF

5.2.2 Characterization

X-ray diffraction (XRD) data were obtained using a Bruker D8 Discover microdiffractometer ($Cu_{K\alpha}$, 40kV, 40mA, graphite monochromator) operated in reflection Bragg-Brentano geometry. Phase analyses were performed by means of Rietveld refinements (TOPAS Academic V1.0, A. Coelho, Bruker) based on the fundamental parameter approach and the structure models of monoclinic (ICSD-Nr. 68782), tetragonal (ICSD-Nr. 66781) and cubic (ICSD-Nr. 105553) ZrO_2, respectively. Scanning electron microscopy (SEM) imaging was done on a LEO Gemini1530 instrument at 3-5 kV acceleration voltage. Products were further characterized by transmission electron microscopy on a Philips 420 instrument (acceleration voltage: 120 kV) and – for high resolution imaging and energy dispersive X-ray (EDX) analysis – an FEI Tecnai F30 ST (operated at an extraction voltage of 300 kV) equipped with an EDAX energy dispersive X-ray spectrometer, respectively.

Differential thermal analysis (DTA) combined with thermal gravimetry (TG) was carried out on a NETZSCH model 429 instrument .

Specific surface areas and pore size distributions were obtained from N_2 sorption measurements performed with an Autosorb-6 (Quantachrom) instrument.

Small angle X-ray scattering (SAXS) experiments were performed on the µ-spot beamline at BESSYII using a MarMosaic 225 (Marresearch, Norderstedt, Germany) CCD area detector. The detector to sample distance was 0.85 m. Measurements were performed with

10 keV radiation (λ = 1.2398 Å, double multilayer monochromator). The SAXS data were recorded as a function of the modulus of the scattering vector q defined as:

(5-1) $$q=(4\pi/\lambda)\cdot\sin\theta$$

where θ is half of the scattering angle. The maximum scattering vector value was 1.5 nm^{-1}.

In order to improve the statistics of the SAXS scattering curves, I(q), the average of several spectra was taken (data collection time 240 s). I(q) takes into account the normalization of the incident beam intensity and was corrected by sample absorption. The SAXS curves were evaluated using the Primus[57] and GNOM[58] software.

Photoluminescence spectroscopy was performed on a Bruins Omega-10 spectrometer with excitation wavelengths being in the range of 250-280 nm.

Raman spectroscopy was carried out on a LabRAM HR800 (Jobin Yvon, Horiba, notch-filter, focus length 800mm) confocal microspectroscope equipped with an optical microscope Olympus BX41 and Peltier-cooled CCD (charge-coupled device) The 514.532 nm Ar^+-laser emission was used for sample excitation. The spectral resolution was 2.7 cm^{-1}.

5.3 Results and Discussion

5.3.1 Differential thermal analysis and thermogravimetry

The thermogravimetric and DTA curves of $Zr(C_2O_4)_2\cdot 4H_2O$ (named $Zr(ox)_2$ in the sequel) under air are displayed in Figure 5-1. Three steps in the TG curve are visible: (i) 2.7% mass loss up to ~ 110°C, (ii) 16.3% mass loss up to ~ 260°C, and (iii) 28.6% mass loss up to 360°C. The second and third step are associated with three exothermic signals at 180, 194 and 338°C in the DTA trace and might be attributed to loss of 2 molecules of CO/f. u. $Zr(ox)_2$ (theor. 16.5%) and 2 molecules of CO_2/f. u. $Zr(ox)_2$ (theor. 25.9%), respectively.

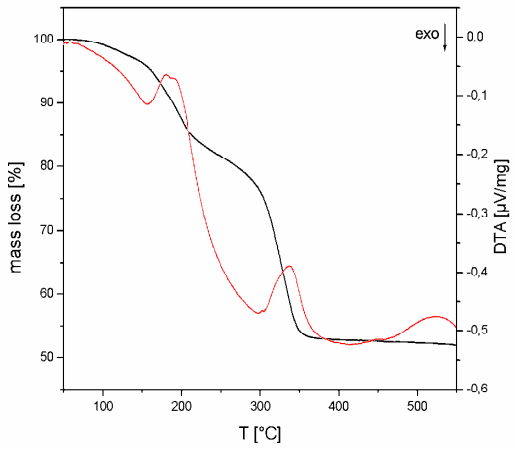

Figure 5-1. Thermogravimetric curve of $Zr(C_2O_4)_2\cdot 4H_2O$ under air.

Above 450°C, a very small endothermic peak can be observed, probably due to incipient crystallization or t-m-phase transformation

5.3.2 X-ray diffraction

XRD measurements were carried out to characterize the chemical nature of the products as well as to determine the mean particle size (see Figure 5-2). Results of the Rietveld refinement analyses are summarized in Table 2 (see supplementary material in the appendix). Note, that the values have to be regarded as semi-quantitative due to extensive peak broadening. Complementary techniques (Raman, SAXS, TEM) were used to corroborate these data.

Table 5-3. Results of the Rietveld refinements of the XRD patterns.

	300°C tube furnace	380°C tube furnace	300°C autoclave	380°C autoclave
Monoclinic	n. a.[a]	-	-	47%
a [Å]				5.21
b [Å]				5.23
c [Å]				5.35
β [°]				99.97
d_{cryst}[b] [nm]				9.4
Pref. orient.[c]				-
Tetragonal	n. a.	100%	100%	53%
a [Å]		3.62	3.61	3.61
c [Å]		5.18	5.21	5.20
d_{cryst}[b] [nm]		9.4	4.9	8.0
Pref. orient.[b]		1.48 [001]	1.29 [110]	0.81 [001]
R_{wp}	n. a.	3.48	4.15	6.20

[a] Not applicable, [b] crystallite size, [c] preferred orientation was determined according to the model of Marsh as implemented in TOPAS.

No sample exhibited reflections due to the precursor, indicating a complete decomposition of $Zr(ox)_2$ to ZrO_2. The modifications obtained depended on the synthesis conditions. For 300TF and 380TF as well as for 300AC samples, only the tetragonal modification ($P4_2/nmc$) was formed. In 380AC samples the monoclinic modification ($P2_1/c$) of ZrO_2 was present in about the same amount as the tetragonal ZrO_2.

Peak broadening indicated a small crystallite size for all samples. Rietveld analyses revealed a mean crystallite size of 8 and 9 nm for 380AC/TF, and 4 to 5 nm for 300AC samples. The diffraction patterns of the 300TF samples point to a mostly amorphous material.

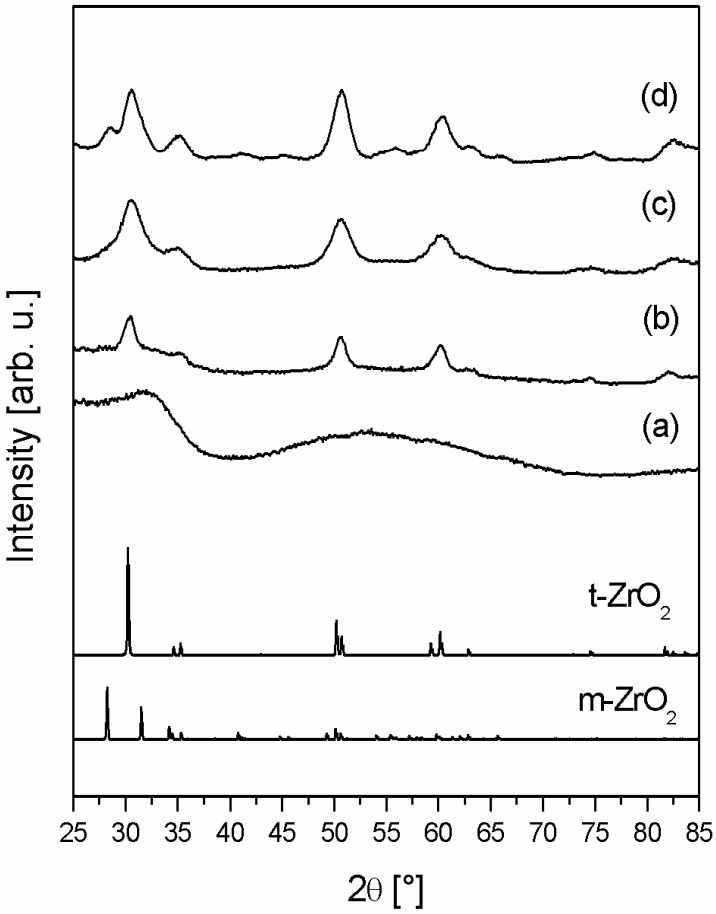

Figure 5-2. XRD pattern of ZrO_2 300TF (a), 380TF (b), 300AC (c), and 380AC (d) samples. Calculated patterns of monoclinic (m) and tetragonal (t) ZrO_2 are given for comparison.

5.3.3 Scanning electron microscopy

SEM revealed micron-sized particles consisting of smaller particles that could not be completely resolved even at highest magnification. The samples exhibited no characteristic differences for different synthesis conditions (Figure 5-3).

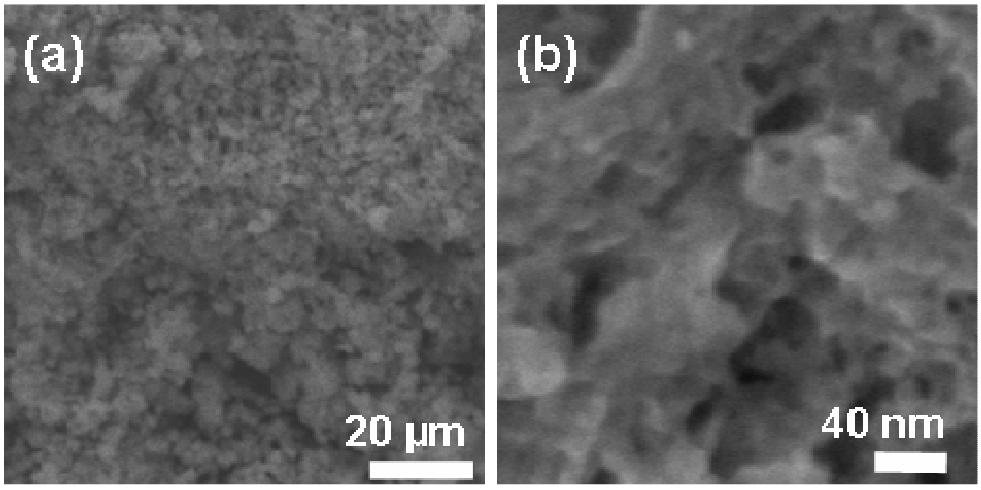

Figure 5-3. SEM image of a 380AC (a) and HRSEM image of a 380TF ZrO_2 sample (b).

5.3.4 Transmission electron microscopy

TEM studies allowed us to gain some deeper insight in the particle size distribution and more detailed information about the structure of the particles. The samples consist of agglomerates of monodisperse, mainly anisotropic particles (Figure 5-4).

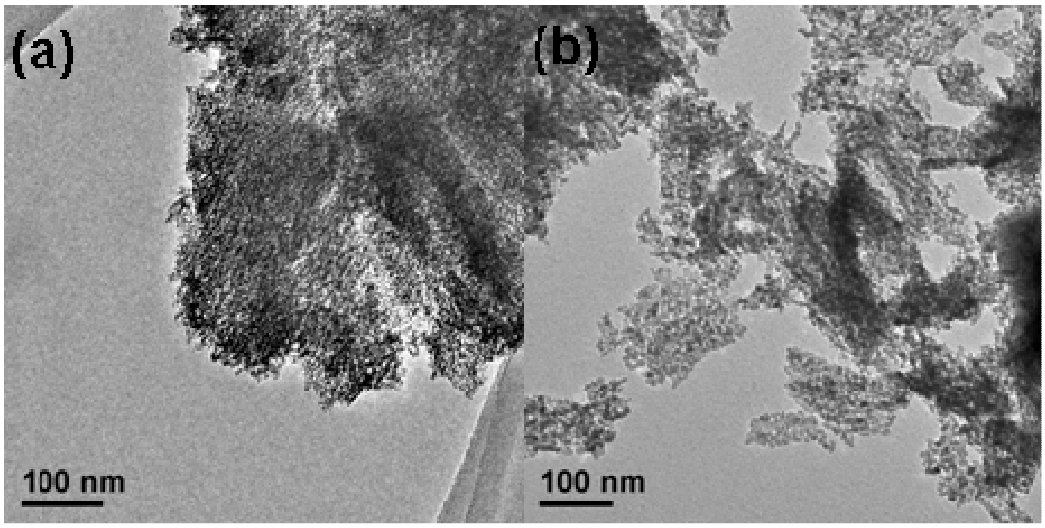

Figure 5-4. TEM images of a 300AC (a) and a 380AC (b) ZrO_2 sample.

5.3.4.1 Autoclave reactions

Information concerning the particle size distribution (Figure 5-5) were obtained from analyses of different overview TEM micrographs of 300AC and 380AC samples. The mean size of the nanoparticles was 4.35 nm (300AC) and 6.75 nm (380AC), respectively. The standard deviation was very small (0.64 nm and 0.83 nm, respectively) confirming the monodispersity of both samples.

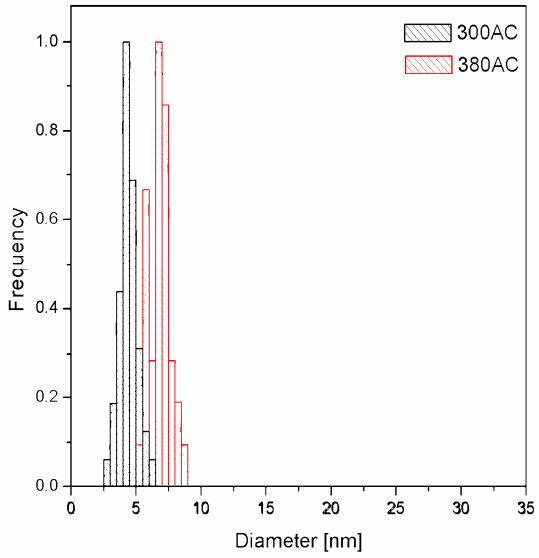

Figure 5-5. Normalized size distribution for a 300AC (black) and 380AC (red) ZrO_2 sample as determined from TEM.

In high resolution TEM images of 380AC ZrO_2 samples, highly crystalline tetragonal and monoclinic nanoparticles that were sometimes interconnected could be observed (Figure 5-6(a) and (b), respectively). The *d*-spacings were obtained from Fourier transformation analyses of the marked areas and correspond well to the calculated values of d_{101} = 0.295 nm and d_{111} = 0.284 nm of tetragonal and monoclinic ZrO_2, respectively.

Figure 5-7 shows a high resolution TEM image of a 300AC ZrO_2 sample. It also exhibits agglomerates of nanoparticles, but these particles are interconnected to a higher extent than in the 380AC sample. The tetragonal modification is prevailing with minor contaminations of m-ZrO_2 particles that were not detected in the X-ray analysis. Energy dispersive X-ray spectroscopy confirmed the 1 : 2 ratio of Zr to O (Figure 5-8) for all samples.

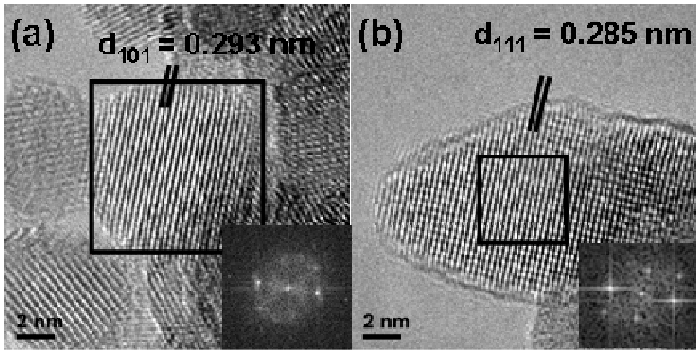

Figure 5-6. HRTEM images of a tetragonal (a) and monoclinic ZrO_2 nanoparticle in a 380AC sample. Reduced FFT images of the black square regions are given in the inset.

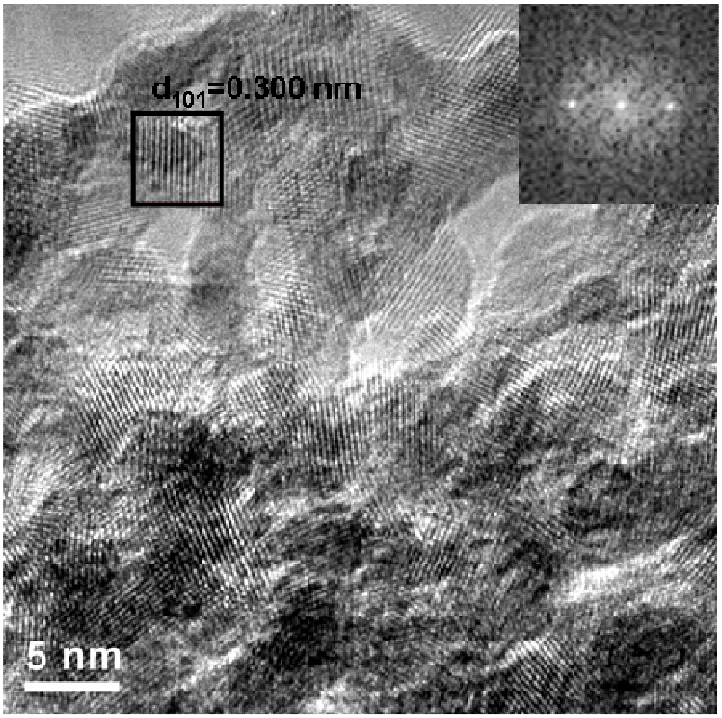

Figure 5-7. HRTEM image of t-ZrO_2 nanoparticles in 300AC sample. FFT of the square region is given in the inset.

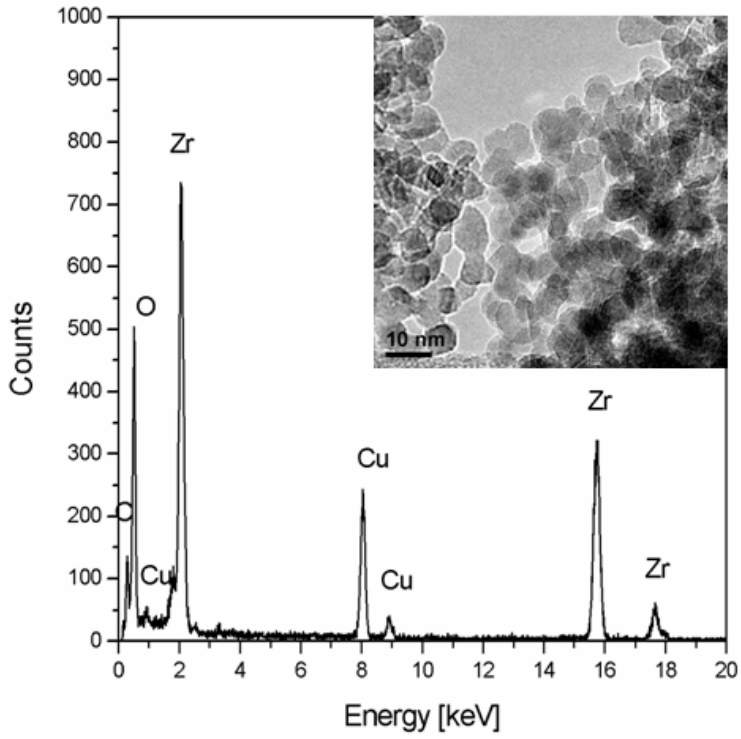

Figure 5-8. EDX spectrum of a 380AC ZrO_2 sample. Cu and C signals are due to the sample support.

The existence of the high temperature modifications, t-ZrO_2 and c-ZrO_2, at low temperatures for nano-sized zirconia is well established. A variety of interpretations of this phenomenon and the question whether these particles are kinetically (metastable)[52] or thermodynamically[59] stable phases are still subject of discussion. Garvie *et al.*[32, 60, 61] suggested, that a difference in surface energy for small particle sizes is responsible for the stabilization of t-ZrO_2 and determined a critical diameter size of 30 nm below which the t-ZrO_2 would be more stable than m-ZrO_2. Other studies found different critical diameter sizes (10-65 nm[22, 62, 63]), the lowest being that of 6 nm.[52, 64] For the c-t-transformation of undoped n-ZrO_2, theoretical and experimental results established a critical diameter of 2 nm.[65] To date, a variety of theories for the stabilization of nano-sized t-ZrO_2 at room temperature other than a critical diameter size have been proposed including the influence of OH^- and other ionic impurities,[66, 67] point defects,[68] oxygen vacancies,[69] topotactic nucleation from an amorphous precursor[70] and agglomeration[62] (see Shukla *et al.* for a detailed discussion[71]).

Extending the model of Shukla *et al.*,[22] who proposed a phase transformation for n-ZrO_2 according to Ostwald's step rule, the phase evolution could be as follows:

(5-2) Amorphous → Cubic → Tetragonal → Tetragonal + Monoclinic → Monoclinic

In our study, no m-ZrO_2 crystallites with diameters < 6 nm were observed. Co-existence of t-ZrO_2 and m-ZrO_2 was found for diameters > 6 nm even in single-domain particles. Thus, *factors other than the particle size only* must be responsible for the phase evolution.

Which factors lead to the formation of t-ZrO_2 at 300°C and the coexistence of m-ZrO_2 and t-ZrO_2 in the autoclave reactions, and why are the t-ZrO_2 particles formed at 300°C more agglomerated than those formed at higher temperature?

One possible explanation for the formation of t-ZrO_2 nanoparticles upon autogenous pressure is surface diffusion involving the reaction gases (H_2O, CO) which are formed by the thermolysis of the $Zr(C_2O_4)_2 \cdot 4H_2O$ precursor. Surface diffusion (with surface diffusion coefficients being in the range of the diffusion coefficient in liquids)[72-74] is known to substantially enhance surface species mobility. Since surface diffusion requires much smaller activation energy than volume diffusion, it is operant already at low temperature and t-ZrO_2, the kinetic product of the reaction, is obtained. The individual nanoparticles are still interconnected because the surface healing is incomplete (Figure 5-9(a)). At a higher temperature, the system is about to reach equilibrium, and well crystallized individual particles (m-ZrO_2/t-ZrO_2) are obtained (Figure 5-9(b)).

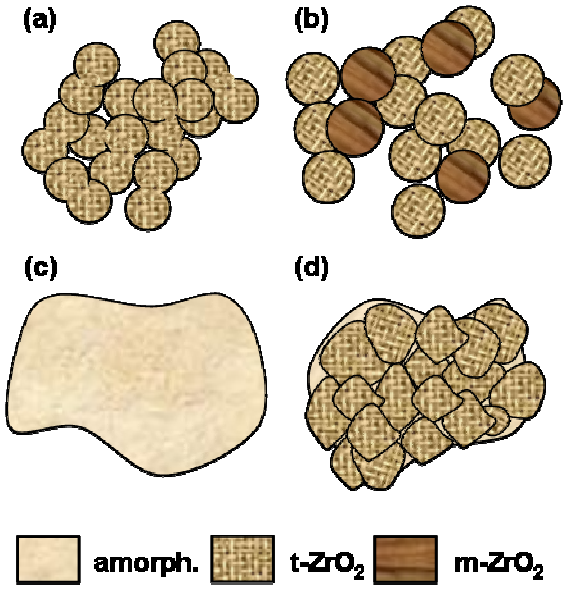

Figure 5-9. Scheme of morphologies of a 300AC (a), 380AC (b), 300TF (c) and 380TF (d) ZrO_2 samples: Interconnected t-ZrO_2 (a) and agglomerated individual t/m-ZrO_2 (b) nanoparticles, and amorphous (c) and multi-domain crystalline (d) micron-sized particles.

5.3.4.2 Tube furnace reactions

Whereas surface diffusion in the autoclave reaction allows the crystallization of the tetragonal phase at 300°C, the absence of a diffusion layer during the thermolysis in a tube furnace leads to the formation of non-crystalline ZrO_2 particles. Figure 5-10 displays the TEM

and HRTEM images of 300TF and 380TF ZrO_2 samples that were obtained from the decomposition of $Zr(C_2O_4)_2 \cdot 4H_2O$ at 300 and 380°C, respectively, in a conventional tube furnace. The samples consist of micron-sized particles, but in contrast to the samples synthesized in autoclaves no discrete nanoparticles were observed. Samples synthesized at 300°C were mainly amorphous (Figure 5-9(c)), whereas those obtained at 380°C showed a much better crystallinity with a d_{101}-spacing of 0.3071 nm corresponding to t-ZrO_2. The average crystallite size within the intergrown micron-size aggregates (Figure 5-9(d)) of a 380TF sample is about 10 nm which is only slightly larger than the value obtained from X-ray diffraction.

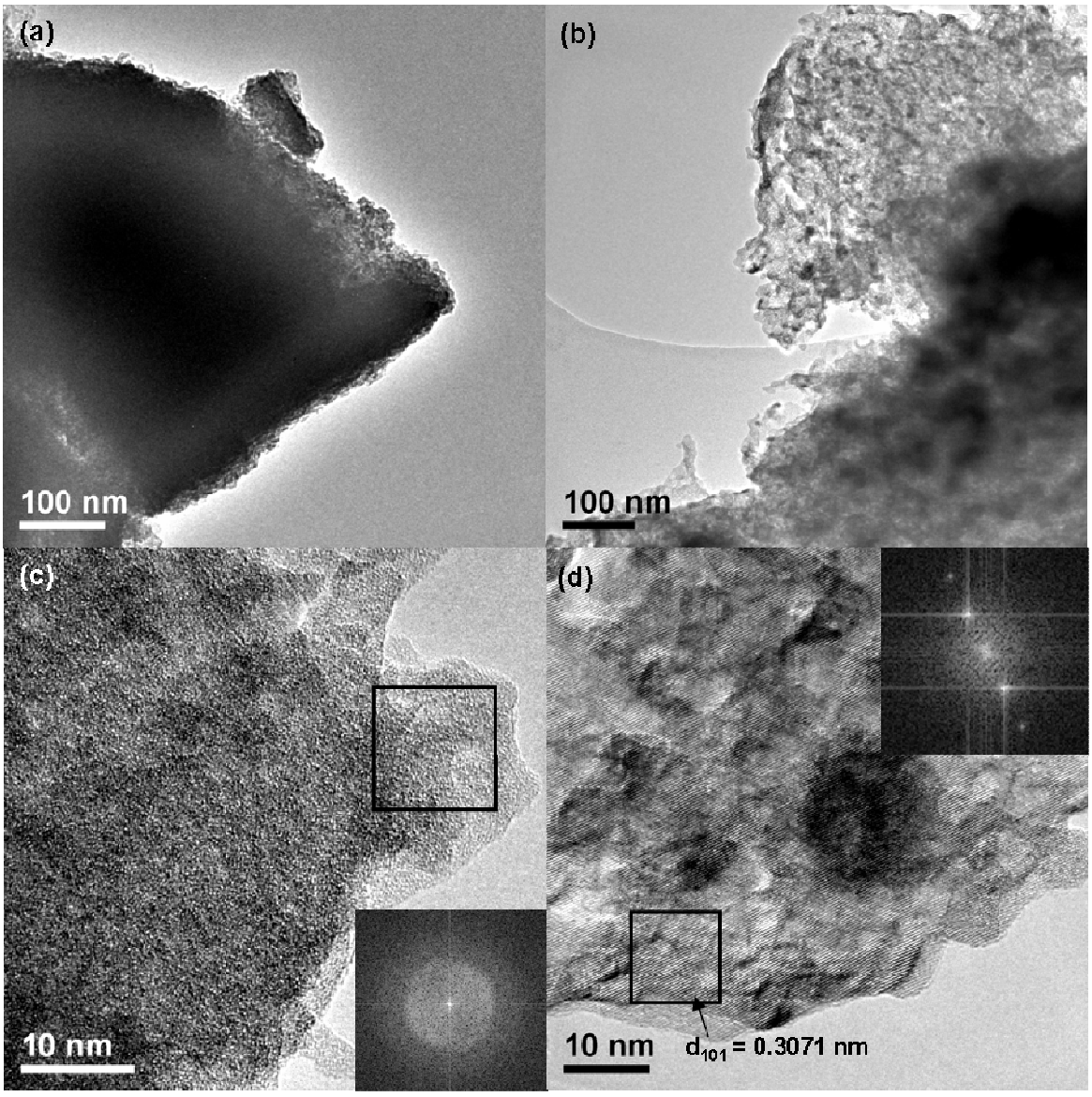

Figure 5-10. (HR)TEM images of a 300TF (a/c) and 380 TF (b/d) ZrO_2 sample. FFT images of the marked areas are given in the inset.

5.3.5 Small angle X-ray scattering

SAXS measurements were performed for the AC samples to obtain global information of the size distribution (Figure 5-11) in addition to the local size distribution (Figure 5-5) evaluated by TEM. The frequency is normalized to the maximum frequency value. Three maxima can be determined corresponding to particles with diameters of 8.9, 15.0 and 21.9 nm, the first being the global maximum. The second and third maximum can be regarded as the outer diameters of agglomerates of two and three particles, respectively. These values are consistent with the crystallite and particle diameters determined by XRD and TEM, respectively.

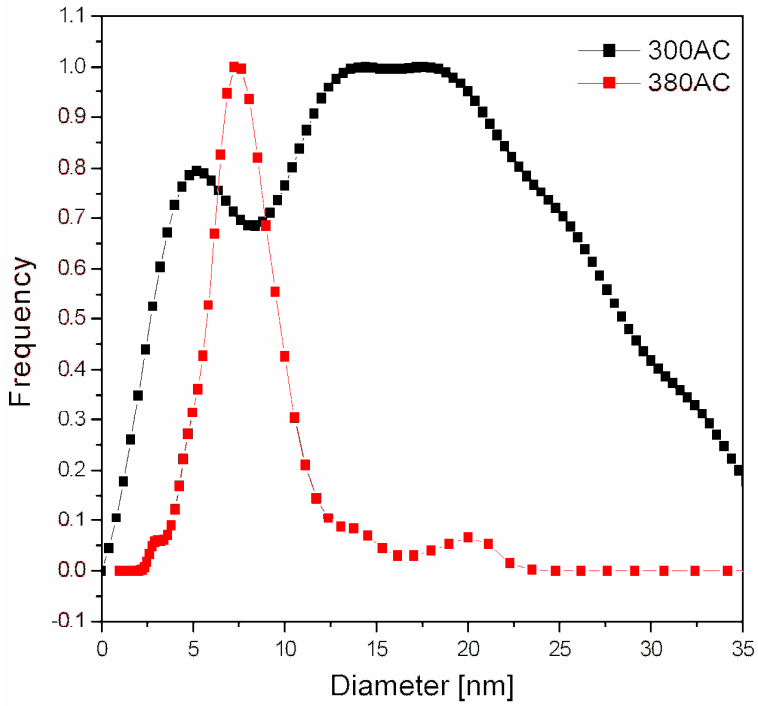

Figure 5-11. Particle size distribution obtained from SAXS measurements of a 300AC and a 380AC sample. Frequency is normalized to the maximum frequency.

In the case of the 300AC sample, the size distribution obtained from a fit to the experimental SAXS data is much broader, with a local maximum at 5.2 nm. This corresponds well to the primary particle size obtained from XRD and TEM measurements. Based on the SAXS model, automated model generation by the DAMMIN program without *a priori* information input reproducibly generated an interconnected particle model where four particles were joined in a tetrahedral kind of coordination as shown in Figure 5-12(a). This matches well with the TEM results (Figure 5-12(b)) where increased particle interconnection was observed for 300AC as compared to 380AC samples.

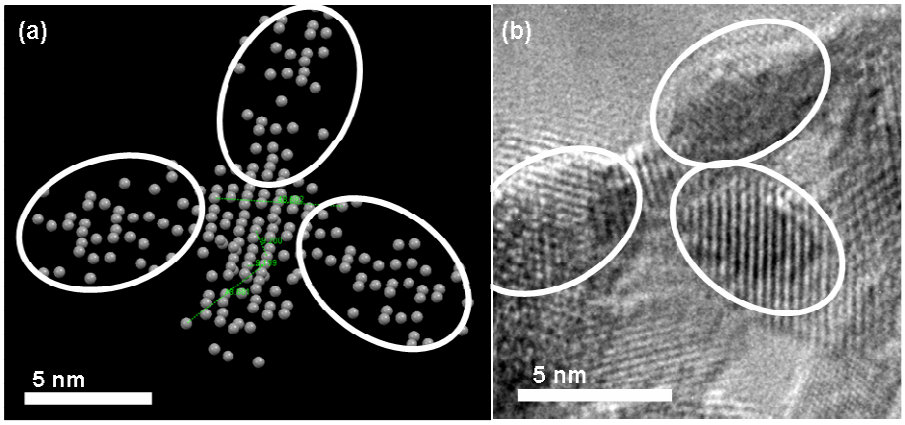

Figure 5-12. Model structure obtained with DAMMIN program (a) and TEM image exhibiting a similar arrangement (b) in a 300AC sample.

5.3.6 Brunauer-Emmett-Teller nitrogen sorption

BET measurements of the samples confirm high specific surface areas (SSA) (Table 5-4). The SSA values of 380AC samples exceed notably the values reported for t-/m-ZrO_2, *e.g.* prepared mechanochemically[49] or by reflux digestion.[75] 380AC samples exhibit higher surface areas than 300AC samples indicating a lower degree of agglomeration as already observed in TEM. Pore sizes vary from 1 and 2 nm for the 300AC and 380AC, respectively, to > 200 nm for both samples. Sharp peaks in the pore size distribution can be observed for pore size diameters as indicated in Table 3.

The pore size diameters of ~ 4-5 nm correspond to values slightly larger than calculated from the expected intergrain volume for spherical particles in densest packing with approximately diameters of 4 and 7 nm (as obtained from TEM measurements). This can be attributed to a coordination number well below 12, as in hexagonal or cubic closed packing.

Table 5-4. Specific surface areas and pore sizes as determined by N_2 sorption measurements.

	300AC	380AC
Pore size [nm]	3.6	5.7 ~ 70
SSA-BET [m^2/g]	276	385
SSA-Langmuir [m^2/g]	470	678

5.3.7 Raman spectroscopy

Because Raman spectroscopy is highly sensible to the polarizibility of the oxygen ions and therefore to an elongation of the *c/a* ratio accompanied by a displacement of the oxygen from the ideal anion site in the fluorite structure, this method is widely used for the distinction of t- and c-ZrO_2 which is difficult by XRD analyses due to peak broadening induced by small grain sizes.[54, 76-78] Figure 5-13 displays the Raman spectra of a 380TF, 300AC and 380AC

sample. Raman bands at ~ 470 and 640 cm^{-1} are indicative of both, t- and m-ZrO_2 but the intensity ratio is different: For the monoclinic modification the 470 cm^{-1} band is more prominent than the band at 640 cm^{-1} and vice versa for the tetragonal modification. Therefore, the m-ZrO_2 can be clearly identified in the 380AC sample and might also be present in minor amounts in the 300AC and 380TF sample, respectively. No indication of a broad band between 530 and 640 cm^{-1}, characteristic for c-ZrO_2 (F_{2g}), is observed in any of these spectra, confirming the results of the Rietveld refinement which indicated that tetragonal and not cubic ZrO_2 has formed.

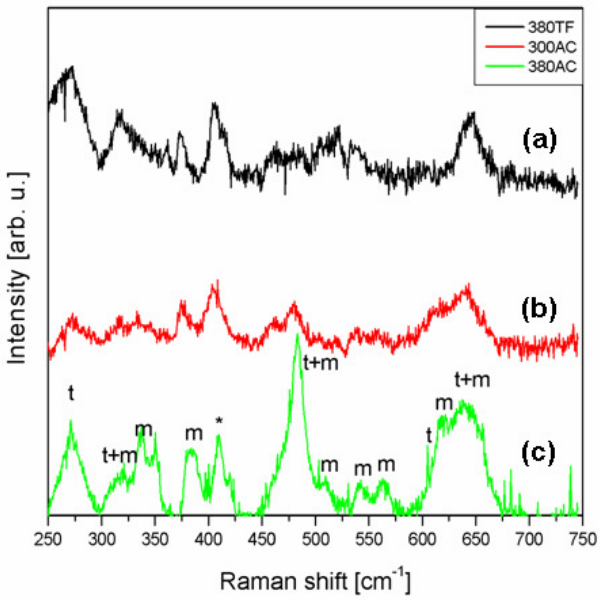

Figure 5-13. Raman spectra of a 380TF (a), 300AC (b) and 380AC (c) sample. Raman bands characterizing the monoclinic and tetragonal ZrO_2 modification are marked with m and t, respectively. An unidentified signal at ~ 400 cm^{-1} is indicated with an asterisk.

5.3.8 Photoluminescence spectroscopy

380AC, 300TF and 380TF samples exhibit a broad fluorescence band in the blue region (centered at 375 nm for the 380AC sample), the intensity being mainly independent of the excitation wavelength (Figure 5-14). The broadness of the fluorescence band and its significant red shift compared to bulk ZrO_2 (221.4 nm) strongly implies that mostly extrinsic states are involved. Surface or defect states might also contribute to a broadening of the band. A rather narrow band at 475 nm is comparable to the results of Liang *et al.*[79] who observed three fluorescence emissions at 402, 420 and 459 nm for ZrO_2 nanoclusters embedded in a polyvinyl alcohol matrix and attributed them to near band-gap transitions.

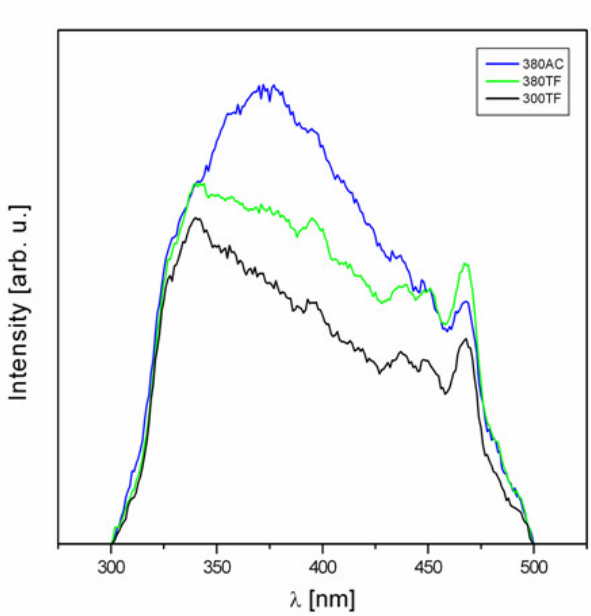

Figure 5-14. Normalized photoluminescence spectra of a 300TF (black), a 380TF (green) and a 380AC (blue) ZrO_2 sample.

5.4 Conclusion

Agglomerates of monodisperse anisotropic m- and t-ZrO_2 particles with average diameters of ~ 8 nm can be obtained by a simple thermal decomposition of $Zr(ox)_2$ in an autoclave at 380°C. By reducing the synthesis temperature to 300°C a single phase t-ZrO_2 product could be obtained with aggregated particles having diameters of approx. 5 nm. Reaction under autogenic pressure was crucial to obtain discrete nanoparticles. We attribute this finding to enhanced crystallization and defect healing due to surface diffusion. The agglomerated particles obtained in this way exhibit very high surface areas and seem to be ideally suited for catalytic applications. HRTEM studies showed that the critical size of 6 nm for the t-to-m-transformation at room temperature in samples prepared via thermal decomposition of Zr-oxalate can be regarded as a lower limit for the monoclinic phase. The co-existence of m- and t-ZrO_2 particles with diameters > 6 nm supports the idea, that factors other than particle size play an important role in the stabilization of the high temperature t-ZrO_2 modification at room temperature in nano-sized materials.

5.5 References

1. Si, P. Z.; Zhang, M., et al. *J. Mater. Sci.* **2005,** 40, 4287.
2. Yamaguchi, T. *Catal. Today* **1994,** 20, 199.
3. Minh, N. Q. *J. Am. Ceram. Soc.* **1993,** 76, 563.
4. Konstantinova, T. E.; Danilenko, I. A., et al. *Proc. - Electrochem. Soc.* **2003,** 2003-7, 153.

5. Fukui, T.; Ohara, S., et al. *J. Nanopart. Res.* **2001,** 3, 171.
6. Pavlik, R. S., Jr.; Klein, L. C., et al. *J. Am. Ceram. Soc.* **1995,** 78, 221.
7. Teixeira, V.; Monteiro, A., et al. *Vacuum* **2002,** 67, 477.
8. Chen, D.; Jiao, X., 1004-5013, 1757605, **2006**.
9. Van, L. A.; Almdal, K., et al., 2005-DK258, 2005099652, **2005**.
10. Li, W.; Zhao, H., et al., 1001-553, 1793024, **2006**.
11. Dunn, D. N.; Seitzman, L. E., et al. *J. Mater. Res.* **1997,** 12, 1191.
12. Tocha, E.; Schoenherr, H., et al. *J. Am. Ceram. Soc.* **2005,** 88, 2498.
13. Affatato, S.; Torrecillas, R., et al. *J. Biomed. Mater. Res. B* **2006,** 78B, 76.
14. Haefele, E.; Kaltenmaier, K., et al. *Sensors and Actuators, B: Chemical* **1991,** B4, 525.
15. Homyonfer, M., Mastai, Y., Hershfinkel, M., Volterra, V., Hutchison, J.L., Tenne, R. *J. Am. Chem. Soc.* **1996,** 118, 7804.
16. Skandan, G. *Nanostruct. Mater.* **1995,** 5, 111.
17. Srdic, V. V.; Winterer, M., et al. *J. Am. Ceram. Soc.* **2000,** 83, 729.
18. Chen, G.; Zhang, K. *Mater. Sci. Forum* **2005,** 475-479, 2973.
19. Wakai, F. *Ceram. Int.* **1991,** 17, 153.
20. Wakai, F.; Nagano, T. *J. Mater. Sci.* **1997,** 26, 241.
21. Panpranot, J.; Taochaiyaphum, N., et al. *Catal. Commun.* **2006,** 7, 192.
22. Shukla, S.; Seal, S., et al. *J. Sol-Gel Sci. Technol.* **2003,** 27, 119.
23. Mizuno, M.; Sasaki, Y., et al. *Abstr. Pap. Am. Chem. Soc.* **2006**, INOR.
24. Massalski, T. B.; Okamoto, H., et al., *Hf-Re to Zn-Zr*. 2nd ed.; ASM International,: Ohio, 1990; Vol. 3, p 2664.
25. Joo, J.; Yu, T., et al. *J. Am. Chem. Soc.* **2003,** 125, 6553.
26. Ramamurthi, S. D.; Xu, Z., et al. *J. Am. Ceram. Soc.* **1990,** 73, 2760.
27. Lee, M. H.; Tai, C. Y., et al. *J. European Ceram. Soc.* **1999,** 19, 2593.
28. Wang, J.; Ee, L. S., et al. *Mater. Lett.* **1997,** 30, 119.
29. Luo, T. Y.; Liang, T. X., et al. *Mater. Sci. Eng. A* **2004,** 366, 206.
30. Liu, Y.; Zheng, C., et al. *J. Am. Ceram. Soc.* **2002,** 85, 3120.
31. Hu, M. Z. C.; Harris, M. T., et al. *J. Colloid Interface Sci.* **1998,** 198, 87.
32. Garvie, R. C. *J. Phys. Chem.* **1965,** 69, 1238.
33. Li, L.; Wang, W. *Solid State Commun.* **2003,** 127, 639.
34. Murase, Y.; Kato, E. *J. Am. Ceram. Soc.* **1983,** 66, 196.
35. Kaya, C.; He, J. Y., et al. *Microporous Mesoporous Mat.* **2002,** 54, 37.
36. Chen, F.; Hong, Q., et al. *J. Am. Ceram. Soc.* **2005,** 88, 2649.

37. Bondioli, F.; Ferrari, A. M., et al. *J. Am. Ceram. Soc.* **2001,** 84, 2728.
38. Rao, K. J.; Mahesh, K., et al. *Bull. Mater. Sci.* **2005,** 28, 19.
39. Chraska, T.; King, A. H., et al. *Mater. Sci. Eng. A* **2000,** 286, 169.
40. Karthikeyan, J.; Berndt, C. C., et al. *Nanostruct. Mater.* **1997,** 8, 61.
41. Djurado, E.; Bouvier, P., et al. *J. Solid State Chem.* **2000,** 149, 399.
42. Mueller, R.; Jossen, R., et al. *Aiche J.* **2004,** 50, 3085.
43. Tsunekawa, S.; Asami, K., et al. *Appl. Surf. Sci.* **2005,** 252, 1651.
44. Nagashima, M.; Nakayama, T., et al. *Mater. Lett.* **2003,** 57, 4023.
45. Nitsche, R.; Winterer, M., et al. *Microbeam Anal. Proc.* **1995**, 239.
46. Rao, C. N. R., Satishkumar, B. C., Govindaraj, A. *Chem. Commun.* **1997,** 16, 15811582.
47. Chen, F.; Huang, L., et al. *Mater. Chem. Phys.* **2006,** 97, 162.
48. Ding, J.; Tsuzuki, T., et al. *Nanostruct. Mater.* **1997,** 8, 75.
49. Dodd, A. C.; Raviprasad, K., et al. *Scr. Mater.* **2001,** 44, 689.
50. Kuznetsov, P. N.; Kuznetsova, L. I., et al. *Appl. Catal. A* **2002,** 227, 299.
51. Yoshimura, M. *Am. Ceram. Soc. Bull.* **1988,** 67, 1950.
52. Winterer, M.; Nitsche, R., et al. *Nanostruct. Mater.* **1995,** 5, 679.
53. Mondal, A.; Ram, S. *Ceram. Int.* **2004,** 30, 239.
54. Xu, G.; Zhang, Y.-W., et al. *J. Am. Ceram. Soc.* **2004,** 87, 2275.
55. Gable, H. S. *J. Am. Chem. Soc.* **1931,** 53, 1276.
56. Berntsen, N.; Gutjahr, T., et al. *Chem. Mat.* **2003,** 15, 4498.
57. Konarev, P. V.; Volkov, V. V., et al. *J. Appl. Crystallogr.* **2003,** 36, 1277.
58. Svergun, D. I. *J. Appl. Crystallogr.* **1992,** 25, 495.
59. Wu, N.-L.; Wu, T.-F., et al. *J. Mater. Res.* **2001,** 16, 666.
60. Garvie, R. C.; Swain, M. V. *J. Mater. Sci.* **1985,** 20, 1193.
61. Garvie, R. C. *J. Phys. Chem.* **1978,** 82, 218.
62. Mitsuhashi, T.; Ichihara, M., et al. *J. Am. Ceram. Soc.* **1974,** 57, 91.
63. Srinivasan, R.; Rice, L., et al. *J. Am. Ceram. Soc.* **1990,** 73, 3528.
64. Nitsche, R.; Rodewald, M., et al. *Nanostruct. Mater.* **1996,** 7, 535.
65. Tsunekawa, S.; Ito, S., et al. *Nano Lett.* **2003,** 3, 871.
66. Cypres, R.; Wollast, R., et al. *Ber. Deut. Keram. Ges.* **1963,** 40, 527.
67. Clearfield, A. *Inorg. Chem.* **1964,** 3, 146.
68. Gomez, R.; Lopez, T., et al. *J. Sol-Gel Sci. Technol.* **1998,** 11, 309.
69. Yashima, M.; Tsunekawa, S. *Acta Crystallogr. B* **2006,** B62, 161.

70. Tani, E.; Yoshimura, M., et al. *J. Am. Ceram. Soc.* **1983,** 66, 11.
71. Shukla, S.; Seal, S. *Internat. Mater. Rev.* **2005,** 50, 45.
72. Volmer, M. *Trans. Faraday Soc.* **1932,** 28, 359.
73. Wicke, E.; Kallenbach, R. *Kolloid Z.* **1941,** 97, 135.
74. Schaefer, H. *Angew. Chem. Int. Ed.* **1971,** 10, 43.
75. Yin, S. F.; Xu, B. Q. *Chin. J. Catal.* **2002,** 23, 214.
76. Sobol, A. A.; Voronko, Y. K. *J. Phys. Chem. Solids* **2004,** 65, 1103.
77. Ozawa, M.; Suzuki, S., et al. *Appl. Surf. Sci.* **1997,** 121, 133.
78. Siu, G. G.; Stokes, M. J., et al. *Phys. Rev. B.* **1999,** 59, 3173.
79. Liang, J.; Deng, Z., et al. *Inorg. Chem.* **2002,** 41, 3602.

6 Conclusion

In this work, the adaptation and optimization of (i) the solvothermal and (ii) the metal-organic chemical vapor deposition (MOCVD) approach as simple methods for the high-yield synthesis of MQ_2 (M=Mo, W, Zr; Q = O, S) nanoparticles was carried out using X-ray diffracttion (XRD), scanning and transmission electron microscopy (SEM/TEM) combined with energy dispersive X-ray analysis (EDXA), Raman spectroscopy, thermal analyses (DTA/TG), small angle X-ray scattering (SAXS) and BET measurements for sample characterization. A heating stage transmission electron microscopy (TEM) study was employed to comparatively investigate the growth mechanism of MoS_2 and WS_2 nanoparticles obtained from MOCVD upon annealing.

A simple route to nanostructured MoS_2 based on the decomposition of the cluster-based precursor $(NH_4)_2Mo_3S_{13}{\cdot}xH_2O$ under solvothermal conditions (toluene, 653 K) has been established. Solvothermal decomposition results in nanostructured material that is distinct from the material obtained by decomposition of the same precursor in sealed quartz tubes at the same temperature. When carried out in the presence of the surfactant cetyltrimethyl-ammonium bromide (CTAB), the decomposition product exhibits unusual string-like morphologies of highly disordered MoS_2 lamellae with high surface areas. Representative crystallite sizes and stacking faults of the nano-MoS_2 produced by the different methods have been modeled by simulations of the corresponding powder X-ray diffraction patterns using the DIFFaX code.

The synthesis of WS_2 onion-like nanoparticles has been achieved by means of a single-step MOCVD process. Furthermore, the results of the successful transfer of the two-step MOCVD based synthesis of MoQ_2 nanoparticles (Q = S, Se), comprising the formation of amorphous precursor particles and followed by the formation of fullerene-like particles in a subsequent annealing step to the W-S system, are presented. X-ray diffraction (XRD) and high-resolution transmission electron microscopy (HRTEM) combined with energy dispersive X-ray spectroscopy (EDX) and high-resolution scanning electron microscopy (HRSEM) were employed to characterize the materials. Based on a study of the temperature dependence of the reactions a set of conditions for the formation of onion-like structures in a one-step reaction could be derived. However, the onion-like structures obtained in the single-step process turned out to be filled, whereas the particles obtained by the two-step procedure were systematically hollow. A model could be devised to rationalize the different outcome of the

reactions. Thus, the MOCVD approach allows a selective synthesis of open and filled fullerene-like chalcogenide nanoparticles.

An *in situ* heating transmission electron microscopy (TEM) study of WS_2 and MoS_2 nanoparticles obtained from metal organic chemical vapor deposition (MOCVD) has been carried out in order to study the growth mechanism of these particles. The general growth behavior of MoS_2 and WS_2 is similar: Round, mainly amorphous particles in the pristine sample transform to hollow onion-like particles upon annealing. A second type of particles with straight layers exhibits only minor changes. A significant difference between both compounds could be demonstrated in their crystallization conduct. Finally, the results of the *in situ* heating experiments are compared to those obtained from an *ex situ* annealing process under Ar.

Attempts of synthesizing MSe_2 (M=Mo, V, Nb, Zr) nanoparticles by means of a solvothermal approach to selenize metal oxalates and, in one case, acetylacetonate by *in situ* generated H_2Se led to the development of a simple low temperature synthesis of monodisperse ZrO_2 nanoparticles with diameters of ~8 nm. Whereas the solvent could be omitted, the synthesis in an autoclave is crucial for gaining nano-sized (n) ZrO_2, as thermal decomposition product of $Zr(C_2O_4)_2 \cdot 4H_2O$ in a conventional tube furnace at 300°C resulted in micron-sized materials. Reactions upon autogenic pressure yielded size-monodisperse mixtures of monoclinic (m) and tetragonal (t) ZrO_2 nanoparticles of about 8 nm diameter and interconnected t-ZrO_2 nanoparticles of ~ 4 nm in diameter, depending on the synthesis temper-ature. Samples were characterized with X-ray diffraction (XRD), small angle X-ray scattering (SAXS), scanning electron microscopy (SEM), transmission electron microscopy (TEM) associated with energy dispersive X-ray spectroscopy (EDS), and Raman microspectroscopy. The n-ZrO_2 exhibits high specific surface areas (up to 385 m^2/g) which make them promising candidates as catalysts and catalyst supports. Co-existence of m- and t-ZrO_2 nano-particles of 6-9 nm in diameter, *i.e.* above the critical particle size of 6 nm, demonstrates that the particle size is not the only factor for stabilization of the t-ZrO_2 modification at room temperature.

In conclusion, synthesis within an autoclave (with and without solvent) and the MOCVD process could be successfully adapted to the synthesis of MoS_2, WS_2 and ZrO_2 nanoparticles. A comparative *in situ* heating stage TEM study elucidated the growth mechanism of MoS_2 and WS_2 fullerene-like particles. As the general processes are similar, a transfer of this synthesis approach to other layered transition metal chalcogenide systems is to

be expected. Application of the obtained nanomaterials as lubricants (MoS_2, WS_2) or as dental filling materials (ZrO_2) is currently on investigation.

7 List of figures

Figure 1-1. Crystal structures of TiS_2 (CdI_2) (a) and MoS_2 (b). 3
Figure 1-2. Schematic illustration of „dangling“ bonds in a MoS_2 sheet (a), the size effect of volume to surface ratio (b), and the minimization of dangling bonds and surface by tube-formation (c). 3
Figure 1-3. Rhombohedral (a) and trigonal (b) point defect inducing curvature in MoS_2 layers.[21] 4
Figure 1-4. Atomic structure of fullerene-like MoS_2 with (a) cuboctahedral and (b) dodecahedral, and (c) octahedral morphology.[40] Transmission electron microscopy image of a nano-octahedron obtained by Parilla is given in (d).[37] 6
Figure 1-5. TEM of multi-walled IFs with a solid core.[92] 9
Figure 1-6. WS_2 nanobox obtained in a spray pyrolysis process.[104] 10
Figure 1-7. Hollow onion-like particle of MoS_2 synthesized in a two-step CVD-based process.[116] 12
Figure 1-8. WS_2 coated multiwall CNT.[140] 13
Figure 1-9. MoS_2 nanotubes synthesized using an alumina membrane as template.[144] 14
Figure 1-10. Scheme for the inverse micelle technique synthesis of IF-MoS_2.[148] 15
Figure 1-11. TEM images of WO_x nanorods (a) and the resulting WS_2-NT (b) obtained by Therese *et al.*[153] 16
Figure 2-1. Powder X-ray diffraction patterns of the product obtained from decomposition of $(NH_4)_2Mo_3S_{13} \cdot xH_2O$ at 653 K for 24 h in an evacuated, sealed quartz tube (Q), in toluene (S), and in toluene in the presence of CTAB (C). A simulated XRD pattern of crystalline 2H-MoS_2 is also displayed. 34
Figure 2-2. Thermogravimetric curves under flowing N_2 of the products Q, S and C. 35
Figure 2-3. TEM images of the product Q. The scale bars are (a) 50 nm and (b) 10 nm. 35
Figure 2-4. TEM image of the product S. The scale bar is 20 nm. 36
Figure 2-5. TEM images of the product C. The scale bars are (a) 100 nm and (b) 10 nm. 36
Figure 2-6. Powder X-ray diffraction patterns of (a) the product Q and (b) DIFFaX simulation of 20 layers of MoS_2, each 10 x 10 nm on side and using a probability of 60% random stacking. 37
Figure 2-7. Powder X-ray diffraction patterns of (a) the product C and (b) DIFFaX simulation of 5 layers of MoS_2, each 10 x 10 nm in size stacked in a completely random manner. 38
Figure 3-1. Schematic representation of the MOCVD experimental setup. 44
Figure 3-2. XRD patterns of a sample synthesized at 650°C before (a) and after (b) annealing at 800°C for 12 h. The arrows indicate the (110)-, (200)- and (211)-reflection of α-W, respectively. Simulated diffraction patterns of 2H- and 3R-WS_2 are given for comparison. 47
Figure 3-3. Development of d_{002}-values obtained from XRD as a function of annealing time for a WS_2 (650) sample. 48
Figure 3-4. HRTEM images of a sample synthesized at 650°C before (a) and after (b) annealing for 12 h at 800°C. A corresponding overview TEM image is given in the inset. 49
Figure 3-5. XRD traces of samples synthesized at 450°C (a), 550°C (b), 650°C (c) and 750°C (d) and the calculated diffraction patterns of 2H- and 3R-WS_2, respectively. A magnification of the (002)-reflection is displayed in the inset. The arrows mark the (200)- and (211)-reflection, respectively, of α-W (JCPDS card no. 4-806). One unidentified reflection is indicated with an asterisk (*). 51
Figure 3-6. Lattice expansion monitored by means of the d_{002}-values of samples synthesized at 450, 550, 650 and 750°C. A linear fit is displayed as black line. 52

Figure 3-7. TEM images of samples synthesized at 450 (a), 550 (b), 650 (c) and 750°C (d). The arrows in (a) and (d) highlight irregular-shaped, small (S-type) particles and bigger, round (R-type) particles..... 53
Figure 3-8. HRTEM images of S-type (a-d) and R-type (e-h) particles, respectively, in samples synthesized at 450 (a/e), 550 (b/f), 650 (c/g) and 750°C (d/h)..... 55
Figure 3-9. Filled (a) and hollow (b) onion-like structures, obtained from a WS_2 (750) and a WS_2 (650/800-12) sample, respectively. Background filtered IFFT of the central part (white square in (a)) of the filled IF- structure is given in (c). The corresponding FFT is given in the appendix (ad chapter 3). 57
Figure 3-10. EDX spectrum of a 450°C sample. The analyzed area is marked in the corresponding TEM image in the inset. W(L) : S(K) ratio is determined as 1 : 2. 58
Figure 3-11. HRSEM image of a sample synthesized at 550°C. S- and R-type particles are marked with arrows.59
Figure 3-12. Schematic representation of the hot zone around the graphite coil. A dotted line represents the minimum temperature needed for particle growth. 60
Figure 3-13. Formation of S (a) and R-type (b) particles: scheme and TEM images. 61
Figure 3-14. Formation of a binuclear particle (left: schematic representation, right: corresponding HRTEM image). 62
Figure 4-1. HRTEM images of (a) small particles (S) with straight layers and (b) round particles (R) in a pristine WS_2 (750) sample and of (c) needle-like (N) and (d) onion-like (O) particles in an annealed WS_2 (450/800-1) sample. Note, R-type particles (b) in low temperature (450°C) syntheses are similar in morphology but do not exhibit layer fringes. 69
Figure 4-2. TEM image of a WS_2 (450) sample (a). High resolution TEM micrographs of S- (b) and R-type (c) particles..... 70
Figure 4-3. HRTEM picture of an R-type particle at 250°C. The structural transformation within three marked areas (white rectangles) is monitored in the sequel..... 71
Figure 4-4. Evolution in the central part (area 1 in Figure 4-3) of R-type particles monitored by means of IFFT of HRTEM images upon annealing at 250 (a), 400 (b), 600 (c) and 800°C (d). Colored lines mark areas with WS_2 layers. The center remains filled throughout the heating. Scale bar = 10 nm. 72
Figure 4-5. IFFT of HRTEM images of an area at the particle boundary (area 2 in Figure 4-3) at 250 (a), 400 (b), 600 (c), 700 (d) and 800°C (e). Some defects are marked with white arrows. Scale bar = 10 nm... 73
Figure 4-6. IFFT of HRTEM images of an R-type particle heated at 250 (a), 400 (b), and 800°C (c). Successive healing of defects and transformation of radial to tangential layers are indicated with black and white arrows, respectively. Scale bar = 10 nm..... 74
Figure 4-7. Schematic growth mechanism for R-type particles in a WS_2 sample: Amorphous material (1), incipient layer formation (2), preferred formation of closed shells at the boundary with basal layers parallel to the surface (3), movement of defects to the outside (4), formation of closed shells (5). Layers are only shown for part of the particle..... 74
Figure 4-8. HRTEM images of S-type WS_2 particles at 250 (a) and 800°C (b). Bending of layers is indicated with a black arrow. 75
Figure 4-9. TEM overview (a) and HRTEM of S-type particles in a MoS_2 sample before annealing. Refer to text for definition of S- and R-type particles marked with arrows in (a)..... 76
Figure 4-10. TEM image of an R-type particle in a MoS_2 sample at 24 (a), 100 (b), 300 (c) and 500°C (d). 77
Figure 4-11. TEM images at 700°C of hollow onions in a MoS_2 sample. Note the significantly larger hollow core for bigger particles (b) as compared to particles of half the size (a). 78

Figure 4-12. Schematic representation of monitored particle development during *in situ* heating TEM study. Refer to text for particles type (S, N, R, O) definition. 80
Figure 5-1. Thermogravimetric curve of $Zr(C_2O_4)_2 \cdot 4H_2O$ under air. 85
Figure 5-2. XRD pattern of ZrO_2 300TF (a), 380TF (b), 300AC (c), and 380AC (d) samples. Calculated patterns of monoclinic (m) and tetragonal (t) ZrO_2 are given for comparison. 87
Figure 5-3. SEM image of a 380AC (a) and HRSEM image of a 380TF ZrO_2 sample (b). 87
Figure 5-4. TEM images of a 300AC (a) and a 380AC (b) ZrO_2 sample. 88
Figure 5-5. Normalized size distribution for a 300AC (black) and 380AC (red) ZrO_2 sample as determined from TEM. 88
Figure 5-6. HRTEM images of a tetragonal (a) and monoclinic ZrO_2 nanoparticle in a 380AC sample. Reduced FFT images of the black square regions are given in the inset. 89
Figure 5-7. HRTEM image of t-ZrO_2 nanoparticles in 300AC sample. FFT of the square region is given in the inset. 89
Figure 5-8. EDX spectrum of a 380AC ZrO_2 sample. Cu and C signals are due to the sample support. 90
Figure 5-9. Scheme of morphologies of a 300AC (a), 380AC (b), 300TF (c) and 380TF (d) ZrO_2 samples: Interconnected t-ZrO_2 (a) and agglomerated individual t/m-ZrO_2 (b) nanoparticles, and amorphous (c) and multi-domain crystalline (d) micron-sized particles. 91
Figure 5-10. (HR)TEM images of a 300TF (a/c) and 380 TF (b/d) ZrO_2 sample. FFT images of the marked areas are given in the inset. 92
Figure 5-11. Particle size distribution obtained from SAXS measurements of a 300AC and a 380AC sample. Frequency is normalized to the maximum frequency. 93
Figure 5-12. Model structure obtained with DAMMIN program (a) and TEM image exhibiting a similar arrangement (b) in a 300AC sample. 94
Figure 5-13. Raman spectra of a 380TF (a), 300AC (b) and 380AC (c) sample. Raman bands characterizing the monoclinic and tetragonal ZrO_2 modification are marked with m and t, respectively. An unidentified signal at ~ 400 cm^{-1} is indicated with an asterisk. 95
Figure 5-14. Normalized photoluminescence spectra of a 300TF (black), a 380TF (green) and a 380AC (blue) ZrO_2 sample. 96
Figure 10-1. High resolution SEM image of a WS_2 (650/800-12)_sample. III
Figure 10-2. Rietveld refinement of a WS_2 (650) sample, consisting of 2H- and 3R-WS_2 and α-W. Note, the percentage values can only be regarded as qualitative due to extreme peak broadening. III
Figure 10-3. FFT of the central part of a WS2(750) sample as indicated in Figure 3-9. Frequencies outside the white circle were filtered for the IFFT in Figure 3-9 (c). III
Figure 10-4. HRTEM (a), corresponding FFT (b) and resulting IFFT (c). Frequencies outside the white circle in (b) have been suppressed by a suitable ring mask. IV
Figure 10-5. Rietveld refinement of ZrO_2 synthesized at 300°C in an autoclave. V
Figure 10-6. N_2 adsorption (red) and desorption (black) isotherms for a 300AC (a) and a 380AC (b) ZrO_2 sample. V

8 List of tables

Table 1-1. Theoretical studies on MS_2 (M=transition metal) nanotubes and fullerene-like particles. 5
Table 1-2. Synthesis methods for MoS_2 nano-materials. 20

Table 1-3. Synthesis methods for WS_2 nano-materials. 21
Table 1-4. Synthesis methods for various transition metal chalcogenide and halide nano-materials. 22
Table 2-1. Surface areas and median pore diameters obtained from N_2 adsorption measurements. 39
Table 3-1. Summary of reaction parameters (T_{ind}, T_{anneal} and t_{anneal}) of the two-step synthesis. 43
Table 3-2. Summary of d_{002}-values obtained from XRD and TEM studies of the WS_2 (650) and WS_2 (650/800-12) sample. The corresponding lattice expansion (in percent) and the ratio of the left to right half of the FWHM are given in parentheses below the d- and FWHM-values, respectively. 47
Table 3-3. Summary of (002)-peak shape parameters: Given are the values for samples synthesized at 450, 550, 650 and 750°C, respectively. 52
Table 5-1. Parameters for the attempted synthesis of MSe_2 nanostructures. 82
Table 5-2. Experimental conditions and labeling. 84
Table 5-3. Results of the Rietveld refinements of the XRD patterns. 86
Table 5-4. Specific surface areas and pore sizes as determined by N_2 sorption measurements 94
Table 10-1. Structure types of MQ_2 compounds (M=transition metal, Q=S, Se, Te). Data based on the inorganic crystal structure database. I
Table 10-2. Characterization methods II

9 Abbreviations (Abbr.)

Abbreviation	Full text/Explanation
(hkl), where h, k, l=integer	Miller indices of a crystal plane
μ	Magnetic momentum
μT	Microtube
2H	Denomination of a modification of a layered transition metal chalcogenide MQ_2. 2 indicates the number of layers per unit cell, H stands for hexagonal symmetry.
3R	Denomination of a modification of a layered transition metal chalcogenide MQ_2. 3 indicates the number of layers per unit cell, R stands for rhombohedral symmetry.
a	Thickness of a sheet
BET	Brunauer-Emmett-Teller, a method to determine the SSA
BuLi	Butyl lithium
C	Elastic modulus
C	In Chapter 2, symbol for samples synthesized under solvothermal conditions with addition of the surfactant CTAB
C_{60}	Carbon allotrope – fullerene
CNT	Carbon nanotube
CTA(B/Cl)	Cetyltrimethylammonium (bromide/chloride)
CVD	Chemical vapor deposition
d_{calc}	Interlayer spacing of the corresponding bulk compound
d_{hkl} (h, k, l = integers)	Interlayer distance between planes with Miller indices h, k, l
DSC	Differential scanning calometry
DTA	Differential thermal analysis
DVM	Discrete variation method
e.g.	For example – abbr. of Latin '*exempli gratia*'
E_{bend}	Bending energy
EDS	Energy dispersive x-ray spectroscopy
EDX(A)	Energy dispersive x-ray analysis
et al.	And others – abbr. of Latin '*et alii*'
FFT	Fast Fourier transformation
FPLMTO	Full potential linearized *muffin-tin* orbital method
HDS	Hydrodesulfurization
HR	High resolution
HRTEM	High resolution transmission electron microscope/microscopy
i.e.	That is – abbr. of Latin '*id est*'
IF	Inorganice fullerene-like (particle)
IFFT	Inverse Fast Fourier transformation
JCPDS	Joint Committee on Powder Diffraction Standards
LDA	Local density approximation
LSDFT	Local spin density functional theory
LTMC	Layered transition metal chalcogenide
M	Wild-card for a metal such as Mo, W
MM	Molecular mechanics
MOCVD	Metal-organic chemical vapor deposition
MOCVD	Metal organic chemical vapour deposition
NC	Nanocluster

Abbreviation	Full text/Explanation
nm	Nanometer
NP	Nanoparticle
NS	Nanostructure
NT	Nanotube
N-type	Needle-like particle (refer to Chapter 3)
NW	Nanowire
O-type	Hollow onion-like particle (refer to Chapter 3)
PDF	Powder diffraction file
PL	Photoluminescence
Q	(i) Wild-card for a chalcogenide such as S, Se, Te. (ii) In Chapter 2, symbol for samples synthesized in a quartz ampoule.
R	Radius
R-type	Round nanoparticles (refer to Chapter 3)
S	In Chapter 2, symbol for samples synthesized under solvothermal conditions
SAXS	Small angle X-ray scattering
SC	Self-consistent
SEM	Scanning electron microscope
SEM	Scanning electron microscopy
SSA	Specific surface area
STM	Scanning tunneling microscope
S-type	Small particle with straight layers (refer to Chapter 3)
T_{anneal}	Temperature [°C] of the annealing under Ar (Chapter 3)
t_{anneal}	Time [h] of the annealing under Ar (Chapter 3)
TB-DFT	Tight-binding density functional theory
T_C	Curie-Temperature
TEM	Transmission electron microscope
TEM	Transmission electron microscope/microscopy
TG	Thermogravimetry
THF	Tetrahydrofuran
T_{ind}	Synthesis temperature [°C] of the MOCVD experiment
U. S.	United States
wt.%	Weight percent
XRD	X-ray diffraction
ρ	Density

10 Appendix

10.1 Layered transition metal chalcogenides (LTMC) of the form MQ_2

Table 10-1. Structure types of MQ_2 compounds (M=transition metal, Q=S, Se, Te). Data based on the inorganic crystal structure database.

	Sc	Ti	V	Cr	Mn	Fe	Co	Ni	Cu	Zn
S	o	CdI_2	CdI_2	layered	FeS_2	FeS_2	FeS_2	FeS_2	FeS_2	o
Se	o	CdI_2	CdI_2	o	FeS_2	3D	FeS_2	FeS_2	FeS_2	o
Te	o	CdI_2	layered	o	FeS_2	3D	CdI_2	CdI_2	o	o

	Y	Zr	Nb	Mo	Tc	Ru	Rh	Pd	Ag	Cd
S	3D	CdI_2	NbS_2	MoS_2	layered	FeS_2	FeS_2	layered	o	o
Se	layered	CdI_2	MoS_2	MoS_2	layered	FeS_2	FeS_2	layered	o	o
Te	o	CdI_2	layered	MoS_2	layered	FeS_2	FeS_2 / CdI_2	CdI_2	o	o

	La	Hf	Ta	W	Re	Os	Ir	Pt	Au	Hg
S	3D	CdI_2	MoS_2	MoS_2	layered	FeS_2	3D	CdI_2	o	o
Se	layered	o	MoS_2	MoS_2	layered	3D	3D	CdI_2	o	o
Te	3D	CdI_2	layered	layered	o	FeS_2	CdI_2	CdI_2	CdI_2	o

FeS_2 = Pyrit

o = no MQ_2 compound known

layered

3D

both types

10.2 Characterization methods

Table 10-2. Characterization methods.

Method	Abbreviation	Information	Comment
Differential thermal analysis/thermal gravimetry	DTA/TG	Thermal behavior (mass loss, enthalpy effects)	Different atmospheres possible
Energy dispersive X-ray spectroscopy	EDS (EDX/EDXA)	Elemental analysis with high spatial resolution	!Mo(L)~S(K); Cu, C (and O) signal by grid/coating; without standard only semiquantitativ
Nitrogen sorption	BET	Specific surface area, pore size distribution	Micro- and mesopores
Photoluminescence	PL	Electronic transitions	Intrinsic and extrinsic effects
Raman spectroscopy		Crystallinity, composition	Allows distinction of tetragonal and cubic ZrO_2
Scanning electron microscopy	REM	Morphology, size distribution	Resolution: Local information
Small angle X-ray scattering	SAXS	Size and shape of particles/agglomerates of mesoscopic size (~ 1 nm < L < ~ 1µm)	Global information
Transmission electron microscopy	TEM	Particle sizes, crystallinity, interlayer distances	Resolution: ~ 1 Å Projection through the particles, very local information
X-ray diffraction	XRD	Composition, crystallinity, crystallite size, Crystal structure	Global information, only crystalline materials are detected, impurities > 5wt.% not detectable

10.3 Supplementary Material

10.3.1 Ad Chapter 3: Selective Synthesis of Hollow and Filled Fullerene-Like (IF) WS_2 Nanoparticles via Metal-Organic Chemical Vapor Deposition (MOCVD)

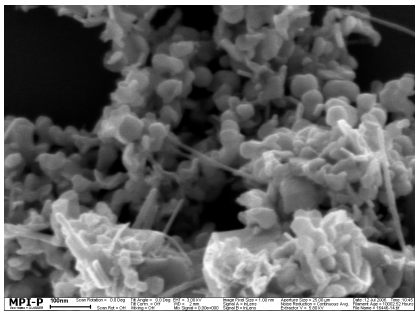

Figure 10-1. High resolution SEM image of a WS_2 (650/800-12)_sample.

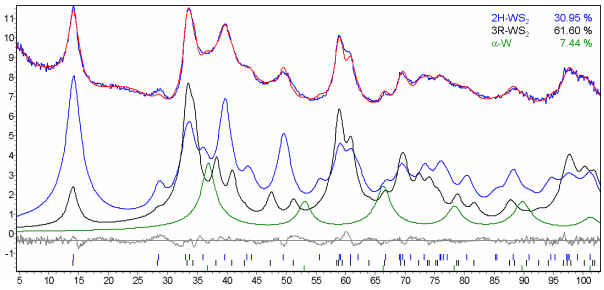

Figure 10-2. Rietveld refinement of a WS_2 (650) sample, consisting of 2H- and 3R-WS_2 and α-W. Note, the percentage values can only be regarded as qualitative due to extreme peak broadening.

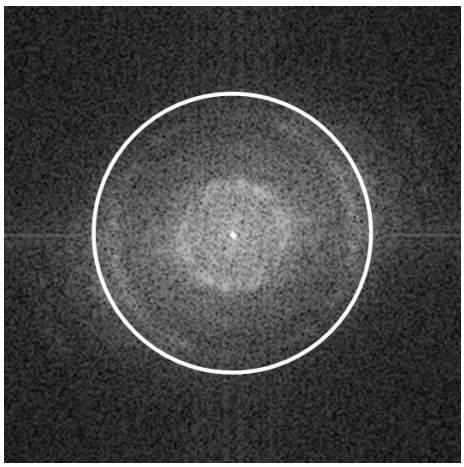

Figure 10-3. FFT of the central part of a WS2(750) sample as indicated in Figure 3-9. Frequencies outside the white circle were filtered for the IFFT in Figure 3-9 (c).

10.3.2 Ad Chapter 4: *In situ* Heating TEM Study of Onion-Like WS_2 and MoS_2 Nanostructures Obtained via MOCVD

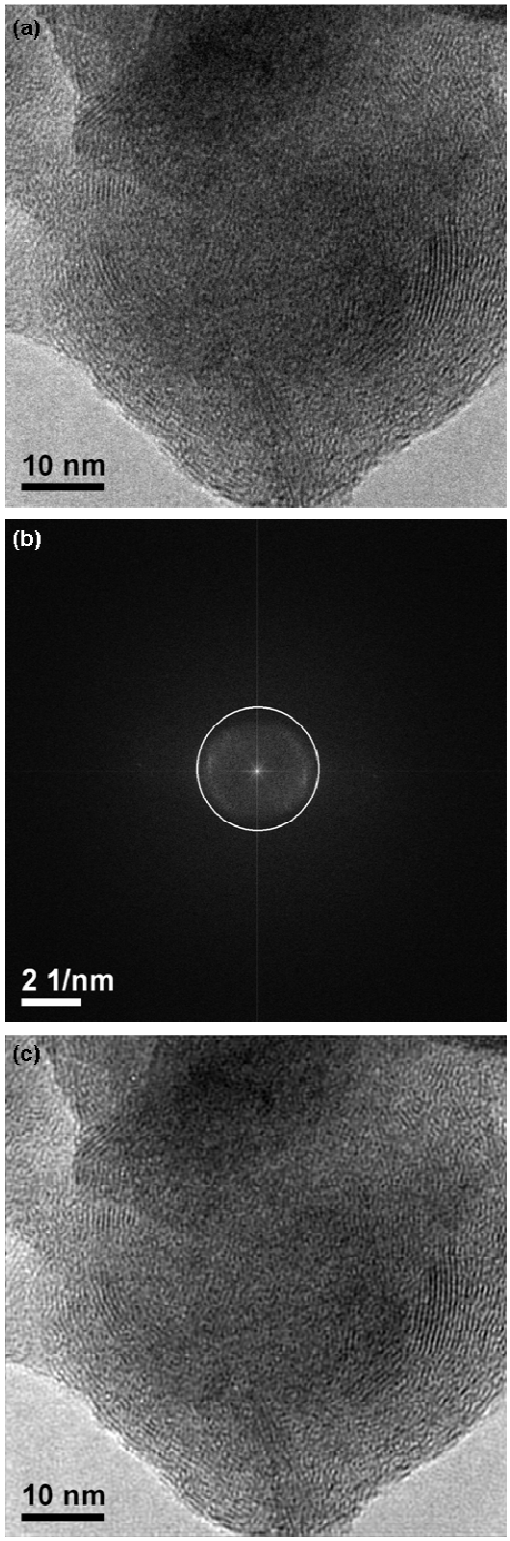

Figure 10-4. HRTEM (a), corresponding FFT (b) and resulting IFFT (c). Frequencies outside the white circle in (b) have been suppressed by a suitable ring mask.

10.3.3 Ad Chapter 5: Low temperature synthesis of monodisperse ZrO_2 nanoparticles with high specific surface area

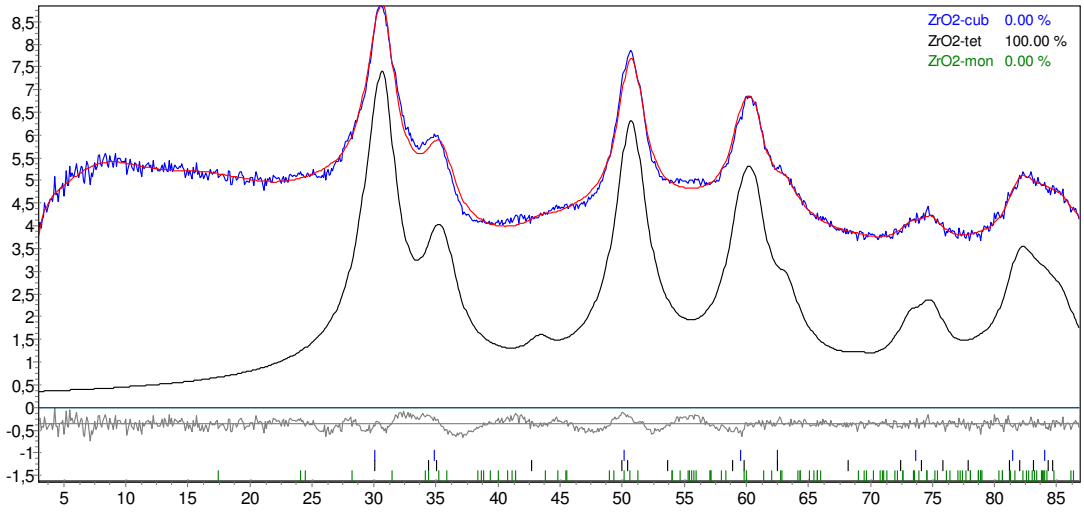

Figure 10-5. Rietveld refinement of ZrO_2 synthesized at 300°C in an autoclave.

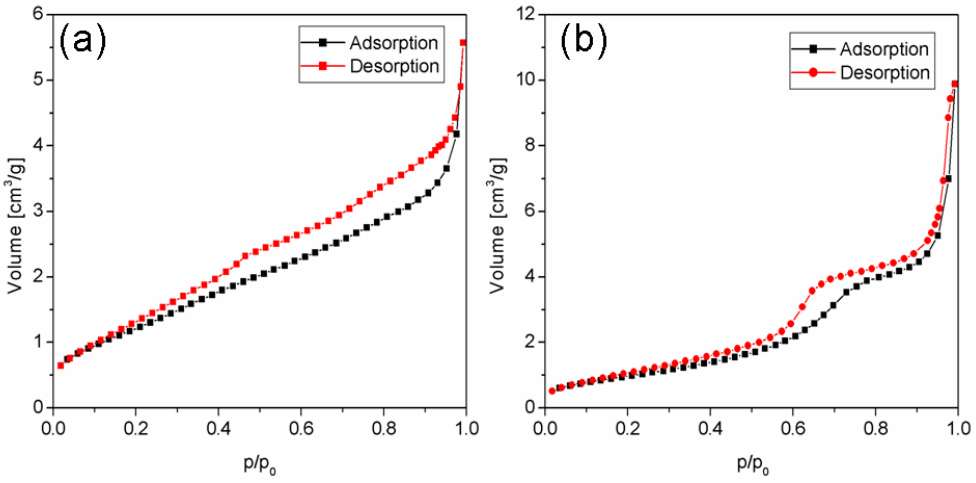

Figure 10-6. N_2 adsorption (red) and desorption (black) isotherms for a 300AC (a) and a 380AC (b) ZrO_2 sample.

10.4 List of Publications

10.4.1 Articles

- In situ *heating TEM study of onion-like WS_2 and MoS_2 nanostructures obtained via MOCVD*[1]
- *Selective synthesis of hollow and filled fullerene-like (IF) WS_2 nanoparticles via metal-organic chemical vapor deposition (MOCVD)*[2]
- *Low temperature synthesis of monodisperse ZrO_2 nanoparticles with high specific surface area*[3]
- *Overcoming the insolubility of molybdenum disulfide nanoparticles through a high degree of sidewall functionalization using polymeric chelating ligands*[4]
- *Metal-organic chemical vapor deposition synthesis of hollow inorganic-fullerene-type MoS_2 and $MoSe_2$ nanoparticles*[5]
- *A solvothermal route to high-surface-area nanostructured MoS_2*[6]
- *Assisted self-sustaining combustion reaction in the Fe-Si system: mechanical and chemical activation*[7]
- *The mechanically activated combustion reaction in the Fe–Si system:* in situ *time-resolved synchrotron investigations*[8]
- *Solvothermal synthesis of $[Mo_4S_4(SH)_4(en)_4]\cdot en$ and $W_4S_4(SH)_4(en)_4]\cdot(S)$ (en = ethylenediamine) containing cubane-type metal-sulfur clusters with terminal SH groups*[9]
- *Time-of-flight photoelectron spectromicroscopy of single MoS_2 nanotubes*[10]
- *Refinement of hydrogen positions in $(NH_4)_2SeO_4$*[11]
- *Different dissolution media lead to different crystal structures of talinolol with impact on its dissolution and solubility*[12]

10.4.2 Conferences

10.4.2.1 Presentation

- *Synthesis of nanostructured transition metal chalcogenides (MQ_2, M = Mo, V, Ti, W)*[13]

10.4.2.2 Posters

- *Nanostructured MoS_2 and WS_2. Application as lubricant and catalyst*[14]

- *Inorganic fullerene-like (IF) particles of MS_2 (M=Mo, W, Re) by metal organic chemical vapor deposition (MOCVD)*[15]
- *A solvothermal route to high surface area nanostructured MoS_2*[16]
- *The refinement of hydrogen positions in $(NH_4)_2SeO_4$*[17]

10.4.3 Patent

- *Synthese von fullerenartigem MoS_2 und MoS_2-Nanoröhren in hoher Ausbeute durch thermische Zersetzung von Molybdaten und anschließende Sulfidierung*[18]

10.4.4 References

1. Zink, N.; Therese, H. A.; Pansiot, J.; Yella, A.; Banhart, F.; Tremel, W. *Chem. Mater.* **2006**, submitted.
2. Zink, N.; Pansiot, J.; Kieffer, J.; Therese, H. A.; Panthöfer, M.; Rocker, F.; Messerschmidt, M.; Kolb, U.; Tremel, W. *J. Am. Chem. Soc.* **2006**, submitted.
3. Zink, N.; Pansiot, J.; Emmerling, F.; Therese, H. A.; Panthöfer, M.; Häger, T.; Hahn, A.; Messerschmidt, M.; Tahir, M. N.; Kolb, U.; Tremel, W. *J. Mater. Chem.* **2006**, submitted.
4. Nawaz, T. M.; Zink, N.; Eberhardt, M.; Therese, H. A.; Kolb, U.; Theato, P.; Tremel, W. *Angew. Chem.* **2006,** 118, 4927.
5. Etzkorn, J.; Therese, H. A.; Rocker, F.; Zink, N.; Kolb, U.; Tremel, W. *Adv. Mater.* **2005,** 17, 2372.
6. Berntsen, N.; Gutjahr, T.; Loeffler, L.; Gomm, J. R.; Seshadri, R.; Tremel, W. *Chem. Mater.* **2003,** 15, 4498.
7. Gras, C.; Zink, N.; Bernard, F.; Gaffet, E. *Mater. Sci. Eng. A* **2006**, submitted.
8. Gras, C.; Berntsen, N.; Bernard, F.; Gaffet, E. *Intermet.* **2002,** 10, 271.
9. Leist, A.; Zink, N.; Hennig, S.; Ksenofontov, V.; Tremel, W. *Z. Anorg. Allg. Chem.* **2006**, in preparation.
10. Gloskovskii, A.; Nepijko, S. A.; Cinchetti, M.; Fecher, G. H.; Kandpal, H. C.; Felser, C.; Klimiankou, M.; Therese, H. A.; Zink, N.; Tremel, W.; Oelsner, A.; Schönhense, G. *Appl. Phys. Lett.* **2005**, submitted.
11. Loose, A.; Melnyk, G.; Zink, N.; Wozniak, K.; Dominiak, P.; Smirnov, L. S.; Pawlukojc, A.; Shuvalov, L. A. *Surf. X-ray Synchr. Neutr. Invest.* **2006**, submitted.

12. Wagner, D.; Glube, N.; Berntsen, N.; Tremel, W.; Langguth, P. *Drug Dev. Ind. Pharm.* **2003,** 29, 891.
13. Zink, N.; Therese, H. A.; Rocker, F.; Schwermann, W.; Etzkorn, J.; Fleischhammer, M.; Gutjahr, T.; Gomm, J. R.; Löffler, L.; Seshadri, R.; Kolb, U.; Li, J.; Tremel, W., *69. Jahrestagung der DPG*, Berlin, 2005; p 110.
14. Zink, N.; Rocker, F.; Kieffer, J.; Pansiot, J.; Yella, A.; Joly-Pottuz, L.; Kolb, U.; Banhart, F.; Tremel, W., *Achema*, 2006.
15. Zink, N.; Rocker, F.; Kieffer, J.; Yella, A.; Therese, H. A.; Kolb, U.; Banhart, F.; Tremel, W., *Annual meeting of the MWFZ*, Mainz, 2006.
16. Berntsen, N.; Gutjahr, T.; Loeffler, L.; Gomm, J. R.; Seshadri, R.; Tremel, W., *Gordon Research Conference: Solid State Chemistry II*, Oxford, 2003.
17. Loose, A.; Smirnov, L. S.; Melnyk, G.; Berntsen, N.; Shuvalov, L. A., *Gordon Research Conference: Solid State Chemistry II*, Oxford, 2003.
18. Therese, H. A.; Berntsen, N.; Tremel, W., **2005**.

11 Zusammenfassung

Die Arbeit befasst sich mit der Anpassung und Optimierung des (i) solvothermalen und (ii) des metall-organischen chemischen Gasphasenabscheidungs-Ansatzes (MOCVD) als einfache Methoden für die Synthese von MQ_2-Nanopartikeln (M=Mo, W, Zr; Q = O, S) mit hohen Ausbeuten. Eine umfassende Charakterisierung wurde mit Röntgenbeugung (XRD) Raster- und Transmissionelektronenmikroskopie (SEM/TEM) kombiniert mit energiedispersiver Röntgenspektroskopie (EDXA), Raman Spektroskopie, thermischen Analysen (DTA/TG), Kleinwinkelröntgenbeugung (SAXS) und Stickstoffsorptionsmessungen (BET) durchgeführt. Nach einer allgemeinen Einleitung zum gegenwärtigen Stand der Forschung, wird ein einfacher Weg zu nanostrukturiertem MoS_2, der auf der Zersetzung der cluster-basierten Vorstufe $(NH_4)_2Mo_3S_{13}{\cdot}xH_2O$ unter solvothermal Bedingungen (Toluol, 653 K) beruht, dargestellt und mit der Zersetzung in Quarzglasampullen verglichen. In Anwesenheit des Tensids Cetyltrimethylammoniumbromid (CTAB) bilden sich unter solvothermalen Bedingungen ungeordnete MoS_2-Schichten mit hohen spezifischen Oberflächen.

In einem weiteren Abschnitt wird die erfolgreiche Übertragung eines Zweistufen-Prozesses (MOCVD + Tempern) zur Synthese von zwiebelartigen WS_2-Nanopartikeln auf einen einstufigen MOCVD-Prozesses vorgestellt, die Ergebnisse mit denen des zweistufigen Prozesses verglichen und ein möglicher Wachstumsmechanimus diskutiert. Durch die Wahl der Synthesebedingungen ist die selektive Synthese von gefüllten oder hohlen zwiebelartigen MQ_2-Partikeln möglich.

Eine transmissionselektronenmikroskopische *in situ* Heizstudie wurde eingesetzt, um vergleichend den Wachstumsprozess von aus dem MOCVD-Prozess gewonnenen MoS_2- und WS_2-Nanopartikeln zu untersuchen und den Ergebnissen des *ex situ* Heizens gegenüber zu stellen. Runde, hauptsächlich amorphe Partikel in der ursprünglichen Probe transformieren unter Erhitzen zu fullerenartigen Nanopartikeln. Ein bedeutender Unterschied zwischen beiden Verbindungen konnte im Kristallisationsverhalten demonstriert werden.

Zuletzt wird eine bereits bei niedrigen Temperaturen mögliche Synthese von monodispersen ZrO_2-Nanopartikel mit Durchmessern von ~ 8 nm vorgestellt. Die Synthese in einem Autoklav für den Erhalt von ZrO_2-Nanopartikeln durch Zersetzung von Zirkonoxalat entscheidend. Das resultierende Material weist hohe spezifische Oberflächen (bis 385 m^2/g) auf und kann demnach als viel versprechender Kandidat für den Einsatz im Katalysebereich (Katalysator, Trägermaterial) angesehen werden. Koexistenz von ZrO_2-Nanopartikeln der monoklinen und tetragonalen Modifikation mit Durchmessern von 6-9 nm, d.h. über der kritischen Teilchengröße von 6 nm, zeigt, dass die Teilchengröße nicht der einzige Faktor für Stabilisierung der tetragonalen Hochtemperaturmodifikation bei Raumtemperatur ist.

Zusammenfassend konnte die Synthese innerhalb eines Autoklaven (mit und ohne Lösungsmittel) und der MOCVD-Prozess erfolgreich auf die Synthese von MoS_2, WS_2 und ZrO_2-Nanopartikeln übertragen bzw. optimiert werden. Eine vergleichende *in situ* TEM Heizstudie klärte den

Wachstumsmechanismus von MoS_2- und von WS_2 fulleren-artigen Partikeln auf. In Zukunft ist eine Übertragung dieser Synthesemethoden auf andere schichtartige Übergangsmetalldichalcogenid-Systeme angedacht. Die mögliche Anwendung der hier gewonnenen Nanomaterialien als Schmiermittel (MoS_2, WS_2) oder als zahnmedizinische Füllmaterialien (ZrO_2) wird zurzeit untersucht.

12 Abstract

Here, we present the adaptation and optimization of (i) the solvothermal and (ii) the metal-organic chemical vapor deposition (MOCVD) approach as simple methods for the high-yield synthesis of MQ_2 (M=Mo, W, Zr; Q = O, S) nanoparticles. Extensive characterization was carried out using X-ray diffraction (XRD), scanning and transmission electron microscopy (SEM/TEM) combined with energy dispersive X-ray analysis (EDXA), Raman spectroscopy, thermal analyses (DTA/TG), small angle X-ray scattering (SAXS) and BET measurements. After a general introduction to the state of the art, a simple route to nanostructured MoS_2 based on the decomposition of the cluster-based precursor $(NH_4)_2Mo_3S_{13}\cdot xH_2O$ under solvothermal conditions (toluene, 653 K) is presented. Solvothermal decomposition results in nanostructured material that is distinct from the material obtained by decomposition of the same precursor in sealed quartz tubes at the same temperature. When carried out in the presence of the surfactant cetyltrimethylammonium bromide (CTAB), the decomposition product exhibits highly disordered MoS_2 lamellae with high surface areas.

The synthesis of WS_2 onion-like nanoparticles by means of a single-step MOCVD process is discussed. Furthermore, the results of the successful transfer of the two-step MOCVD based synthesis of MoQ_2 nanoparticles (Q = S, Se), comprising the formation of amorphous precursor particles and followed by the formation of fullerene-like particles in a subsequent annealing step to the W-S system, are presented. Based on a study of the temperature dependence of the reactions a set of conditions for the formation of onion-like structures in a one-step reaction could be derived. The MOCVD approach allows a selective synthesis of open and filled fullerene-like chalcogenide nanoparticles. An *in situ* heating stage transmission electron microscopy (TEM) study was employed to comparatively investigate the growth mechanism of MoS_2 and WS_2 nanoparticles obtained from MOCVD upon annealing. Round, mainly amorphous particles in the pristine sample transform to hollow onion-like particles upon annealing. A significant difference between both compounds could be demonstrated in their crystallization conduct. Finally, the results of the *in situ* heating experiments are compared to those obtained from an *ex situ* annealing process under Ar.

Eventually, a low temperature synthesis of monodisperse ZrO_2 nanoparticles with diameters of ~ 8 nm is introduced. Whereas the solvent could be omitted, the synthesis in an autoclave is crucial for gaining nano-sized (n) ZrO_2 by thermal decomposition of $Zr(C_2O_4)_2$. The n-ZrO_2 particles exhibits high specific surface areas (up to 385 m^2/g) which make them promising candidates as catalysts and catalyst supports. Co-existence of m- and t-ZrO_2 nano-particles of 6-9 nm in diameter, *i.e.* above the critical particle size of 6 nm, demonstrates that the particle size is not the only factor for stabilization of the t-ZrO_2 modification at room temperature.

In conclusion, synthesis within an autoclave (with and without solvent) and the MOCVD process could be successfully adapted to the synthesis of MoS_2, WS_2 and ZrO_2 nanoparticles. A comparative *in situ* heating stage TEM study elucidated the growth mechanism of MoS_2 and WS_2 fullerene-like particles. As the general processes are similar, a transfer of this synthesis approach to other layered transition metal

chalcogenide systems is to be expected. Application of the obtained nanomaterials as lubricants (MoS_2, WS_2) or as dental filling materials (ZrO_2) is currently under investigation.